KAUNAS UNIVERSITY OF TECHNOLOGY

SAULIUS RAČKAUSKAS

INVESTIGATION OF INTERNAL BALLISTICS OF SOLID PROPELLANT ROCKET MOTOR BY NUMERICAL AND EXPERIMENTAL METHODS

Doctoral dissertation
Technological sciences, Mechanical engineering (T 009)

2020, Kaunas

This doctoral dissertation was prepared at Kaunas University of Technology, Faculty of Mechanical Engineering and Design, Department of Transport Engineering during the period of 2014–2019.

Scientific Supervisor:

Prof. Dr. Habil. Algimantas FEDARAVIČIUS (Kaunas University of Technology, Technological Sciences, Mechanical Engineering (T 009)).

Doctoral dissertation has been published in:
http://www.ktu.edu

Editor:

Armandas Rumšas (Publishing Office "Technologija")

KAUNO TECHNOLOGIJOS UNIVERSITETAS

SAULIUS RAČKAUSKAS

KIETOJO KURO RAKETINIO VARIKLIO VIDINĖS BALISTIKOS TYRIMAS SKAITINIAIS IR EKSPERIMENTINIAIS METODAIS

Daktaro disertacija
Technologijos mokslai, mechanikos inžinerija (T 009)

2020, Kaunas

Disertacija rengta 2014-2019 metais Kauno technologijos universiteto Mechanikos inžinerijos ir dizaino fakultete, Transporto inžinerijos katedroje.

Mokslinis vadovas:

Prof. habil. dr. Algimantas FEDARAVIČIUS (Kauno technologijos universitetas, Mechanikos inžinerija – T 009).

Interneto svetainės, kurioje skelbiama disertacija, adresas:
http://ktu.edu

Redagavo:

Armandas Rumšas (leidykla “Technologija”)

ACKNOWLEDGMENTS

The first thought which comes to my head is a ‘Thank You’ note for my supervisor, professor Algimantas Fedaravičius, DSc who gave me the once-in-a-lifetime opportunity to be able to contribute to one of the hardest engineering disciplines – the rocket science. Other huge thanks go to a colleague of mine, Arvydas Survila, who is my engineering idol, my best critic and supporter throughout the hard times of research and development of this project. I would like to thank all of my other colleagues from the *Institute of Defence Technologies* who have been very kind and helpful during all of these years. I am glad to call them friends. Of course, I must thank all of my family and friends for their kindness and understanding when I had ‘no life at all’ during this long time. I must render my gratitude to all the great guys at *Warsaw Military University of Technology* and supervisor Zbigniew Leciejewski for his help, support and guidance.

Tėvynės labui !

TABLE OF CONTENTS

INTRODUCTION

Relevance of the work

When it comes to the solid-propellant rocket motor (SRM) development and design, it is paramount to precisely determine the internal characteristics of ballistics in order to fully understand the motor's performance with the prescribed design requirements. Normally, performance is measured during static testing which allows considering more profoundly the various physical and chemical attributes taking place within the motor. Such testing requires a significant amount of time, infrastructure and resources, which, in turn, makes it labor-intensive and relatively expensive.

On the other hand, simulations can reduce the required resources and even provide deeper insights into the motor's internal ballistics, such as the pressure and temperature in the combustion chamber, the mass flow rate, the nozzle influence and other parameters which are almost impossible to measure during static testing due to extreme physical conditions within the motor that renders the measuring probes incapable of reading the data. However, in order to use the simulation approach, one must first validate it so that the data could be trusted.

Furthermore, the major difference between static testing and simulations (provided that the model is valid) is the ability to use the model not only to peer into the inner workings of an already existing model retrospectively but also to simulate different potential configurations of the motor and observe their performance without having to build the motor. This enables precision engineering and cost-effective means for optimizing an already existing motor or designing a new one with different prescribed parameters. All in all, a valid simulation based numerical model may enable researchers to extend the range of the rocket or simulate what it would take to lift it to space while minimizing the labor and monetary resources.

This research is based on the internal ballistics of the RM-12K solid rocket motor which is part of the RT-400 aerial target system designed and developed at the *Institute of Defence Technologies* (IDT) at Kaunas University of Technology (KTU). The purpose of the research was to construct a valid numeric model, which would allow researchers to track the change of the propellant grain evolution and various internal ballistic parameters during the combustion process over time, such as the pressure, temperature, thrust, propellant grain regression (the grain open surface area), the grain burn rate, the mass flow rate through the nozzle and the density of the combustion products.

The main objectives of this research are to construct a robust and valid simulation based on the numerical model for the solid rocket motor internal ballistics characteristics research which could substitute the experimental approach. This achievement would let researchers design a new type of rocket motors for various applications or optimize the already produced designs in order to achieve even better performance characteristics.

The aim of the work

To develop a united methodology for the construction of solid propellant rocket motors by construction of the simulation for obtaining internal ballistics characteristics, to perform research and its validation by comparative analysis of the results of numerical modeling and static experimental tests.

Work objectives

1. To develop a computer-aided 3D geometric model of a solid propellant rocket motor to evaluate the energy properties of the propellant and its combustion in the grain and nozzle discharge area.
2. To determine the initial and boundary conditions of simulation, which takes into account the pressure and temperature in the combustion chamber of the motor, the physical properties of the fluid and solid state, and the CAD geometry and mesh, thus allowing accurate modeling of solid propellant combustion and the internal ballistics of the motor.
3. To perform modeling of the combustion process of solid propellant grain, to determine the characteristics of the internal ballistics of the rocket motor and to present the obtained results of the modeling of the solid propellant rocket motor.
4. To perform comparative analysis of numerical modeling and experimental – static studies and verification of the simulation results when the motor is in its steady-state.
5. To develop a research-based methodology for the development of solid-propellant rocket motors that would reduce or completely replace the need for experimental testing of the motor under development, thereby reducing the time and economic costs in designing multi-purpose solid-propellant rocket motors.

Methodology

The dissertation was based on theoretical, analytical, numerical and experimental research. By using theoretical and analytical research methods, a simulation based on the numerical model of the internal ballistics of solid-propellant rocket motors was constructed and investigated. The results for the simulation were validated by the experimental approach while using the RM-12K solid-propellant rocket motor internal ballistics characteristics.

Scientific novelty

The dissertation extends the methodology of the construction of solid propellant rocket motors by using the simulation approach of motor internal ballistics, which evaluates the energy properties of the solid propellant and allows to obtain the internal ballistics characteristics and the geometrical parameters of the motor.

The practical value of the work

Reliable and valid methods for internal ballistic performance studies of solid propellant rocket motors have been developed, which reduces or alters the need for the experimental testing of the motor under development. This allows the design of solid-state rocket propulsion motors for various applications or optimization of previously manufactured ones to achieve better performance at a reduced time and cost.

Defended statements

1. Simulation based on the numerical model which evaluates the energetic properties of the solid propellant and the moving interface of the propellant grain significantly improves the design and research process of solid-propellant rocket motors to simulate internal ballistic processes.
2. Simulations allow the identification of motor internal ballistics characteristics and physical processes values (the burning surface, area, volume, burn rate) that would otherwise be undetectable in experimental testing.
3. Valid models can reduce or even eliminate the need for static-experimental testing for solid-propellant rocket motors.

Approval of work results

The research results have been presented in 3 publications in scientific journals in the ISI database with the citation index as well as in 3 international scientific conferences. The aerial target system containing the developed motor has been issued a patent in the *Patent Database of the Republic of Lithuania*. Also, the *RT-400* aerial rocket target system using the RM-12K solid-propellant rocket motor was awarded the *Lithuanian Product of the Year Gold Medal*.

Structure of the work

The dissertation consists of 4 main parts: in the first part, the author presents a review of the solid rocket motor design, various types of propellants, nozzle types, grain types, and combustion phenomena. The second part presents the model and methods for the simulation of the solid propellant rocket motor. The third part discusses the methodology and the results of the experimental approach for the static testing of the rocket motor. In addition, the test stand design and operation are discussed. In the fourth part, the results of the simulation are presented. Comparison and validation of the model with experimental results are presented and discussed. The conclusions drawn from the research with regard to the initial purpose of the work as summaries are given at the end of each chapter. At the end of the work, the conclusions of the whole research are formulated. The volume of the doctoral dissertation is 102 pages. It contains 58 figures, 41 formulas, 18 tables, and 92 references.

Abbreviations used in the work:

SRM – Solid rocket motor
TWR – Thrust to weight ratio
APCP – Ammonium perchlorate composite propellant
ANCP – Ammonium nitrate composite propellant
C-D nozzle – Converging-diverging nozzle
RM-12K – Rocket motor used in the research
RT-400 – Aerial target system used in the research

1. LITERATURE REVIEW, MOTIVATION, AND FORMULATION OF KEY RESEARCH OBJECTIVES AND DEFINITIONS

1.1. Literature review

According to the *Encyclopaedia Britannica*, the field that is now known as *rocket science* originated back in the 17th century with the publication of *Ars Magna Artilleriae* (a.k.a. *Artilleriae ars magna*), originally written by Kazimieras Simonavičius and later translated into the French, German, English, and Polish languages (Siemienowicz 1650) [1]. The field mostly focused on the use of projectiles for military applications as based on Newtonian Physics. 253 years later, Tsiolkovsky introduced his rocket equation (Tsiolkovsky 1903) [2] which was the first mathematical derivation describing the motion of rocket vehicles. This mathematical model enabled the launch of the first liquid-propellant rocket merely within 23 years after Tsiolkovsky's publication (Goddard 1926) [3]. Finally, after 16 more years, the first successful suborbital flight was achieved by the German-made V2 rocket (von Braun 1946) [4] thus providing the foundations that later sparked the modern era of the rocket science.

The modern era of the rocket science began with the *Space race* which started on August 2, 1955 [5]. The first breakthrough in the solid rocket propellant development was made in 1968 (Schmidt *et al.*) [6] when aluminum was introduced as a fuel for propellant combustion. APCP (Ammonium Perchlorate Composite Propellant) propellant and its surrogates, such as ANCP (Ammonium Nitrate Composite Propellant) were and are still being widely used as one of the most robust solid propellants in the market today. APCP rocket motors were used in the Space Shuttle system as SRBs (Solid Rocket Boosters) since the start of the Space Shuttle operation in 1981 (NASA) [7]. As a widely used practice, SRBs have been used in all space agencies during major space launches since 1981 up till the present day. Despite the strides that have been achieved within the field of rocket science, the research and development in many cases was mostly based on experimental data and calculations by hand or computers of that time that had significant computational limitations compared to today's machines.

Since 1981, the computational power has become more effective and accessible by tens if not hundreds of orders of magnitude. In the 1990s, this development sparked interest in creating complex computational models and solving those by using algorithms, i.e., by creating numerical simulations for rocket ballistics applications (Meha 1996) [8]. Due to the aforementioned reasons, the number of research papers has increased significantly in the field of investigation of the credibility and validity of the developed computational models. Most attention was focused on AP (Ammonium Perchlorate) propellants because they were more energetic than AN (Ammonium Nitrate) propellants due to AN's high hygroscopic properties and several crystalline transitions; however, the new modeling techniques and interest in this type of propellants enabled research teams to eliminate the drawbacks and take advantage of the additional benefits that Ammonium Nitrate provides in relation to Perchlorate (Kondrikow *et al.* 1999) [9].

In the paper *Modeling of Flowfield Features During Ignition of Solid Rocket Motors* published in 2002, the research team investigated a solid propellant rocket motor by using numerical methods (Serraglia *et al*. 2002) [10] where the authors performed transient simulations on their motor. Such transient simulations compared with static simulations are computationally expensive yet crucial because of the dynamic nature of the propellant combustion phenomena. Similar methods are now being used in the modern Computational fluid dynamics (CFD) algorithms. The CFD models' development progress and evolution are best described in M. W. Beckstead's research paper named *Recent Progress in Modelling Solid Propellant Combustion* (Beckstead 2006) [11]. The paper is a collection of works from various research teams which allowed to see the bigger picture in the past development of the solid propellant combustion models. Additionally, the Australian Government has greatly contributed to the CFD field by researching solid propellant modeling for defence applications (Harrland *et al*. 2012) [12]. The same type of investigations of solid propellants combustion was published at the academic level (Ajinkya *et al*. 2012) [13].

Nowadays, all major space and defence industry companies use tools developed by major CAD and CAE companies. The tools combine the aforementioned CFD research and enable engineers to develop simulations more efficiently and researchers to study the processes more accurately thus allowing them to push the field even further. This synergy is crucial for the future growth of the market. New computational models are being introduced continuously at an increasing pace. It is safe to claim that the feedback loop between engineers and researchers has never been shorter in the history of this field, which should allow this industry to develop and expand like never before. This is one of the reasons the author chose this field of research, that is, the ability to contribute to the body of work that, although began as a tool for the military, now has potential to take people to Mars and beyond.

1.2. Motivation

The motivation for this paper stems mainly from the idea of 'digital twins' [14]. The key aspect of the idea is the development of a computer model that features the exact same characteristics as the actual real-life object, rocket motor, etc. It enables one to simulate the motor's performance without static tests and to fine-tune the motor's properties and optimize it due to the amount of data that is possible to collect from the model. Up until recently, the research of rocket motors capable of supersonic flight was reserved only for governmental agencies with the appropriate funding and motivation due to the prohibitively expensive experiments and tests that are inherently needed for this kind of research. What is more, due to the mostly military nature of such governmental projects, there is lack of available public knowledge which is needed to design a motor without performing one's own tests and experiments. Fortunately, due to the advent of modern computing, it is now possible to create a computer model that is accurate enough so that its performance could be simulated in a realistic way in order to obtain data that was recently only available after experiments or analytical calculations which – by hand – is immensely complicated and provides just a small glimpse of the actual inner workings of the motor, whereas, with a computer model, every data point in its entirety is collected and can be analyzed step by step thus providing researchers with a sophisticated tool that may change the rocket motors as we know them. Therefore, due to the reasons listed above, the idea for this research was born which revolves around the actual real-life motor which is being used in practice on an ongoing basis.

The aforementioned situation within the aerospace industry is a product of history and key recent developments that will be briefly covered for a broader context. Nowadays, the aerospace industry as a whole can be divided into two categories – subsonic and supersonic. History has shown that subsonic aerospace technologies are mostly used by the private (civilian) sector, whereas the supersonic flight is mostly used by governments, and, to be more accurate, by the military. This division was mostly based on cost efficiency. Supersonic vehicles were and still are expensive to design, develop and maintain, whereas subsonic vehicles, such as passenger jet planes or domestic drones, are significantly more affordable and readily available. Furthermore, supersonic technologies were experimented with for the civilian use – such as in the case of Concorde [15] – but after several major issues with the planes [16], the project was canceled, and, to this day, it is incredibly hard to find a supersonic aircraft that is used for civilian benefit. On the other hand, supersonic flight is highly attractive to the military sector. It bears little explaining as of why speed is beneficial in combat situations. Therefore, militaristic motivations kept the supersonic technology alive and well through the 1970s up until the 1990s and early 2000s [17, 18]. Due to the above listed motivations, the advent of supersonic jet planes, ramjets and scramjets was possible [19, 20]. In Table 1.1 one can see a comparison of the different propulsion technologies with their advantages and disadvantages.

Table 1.1. Comparison of the various propulsion types for aerospace applications

No.	Type	Description
1.	Jet engine	Efficient with bypass for subsonic applications M>0.7. Fuel inefficient with afterburner for supersonic applications M<3. Can work from M=0. Limitations regarding altitude.
2.	Ramjet	Can only work when M>2
3.	Scramjet	Can only work when M>5
4.	Turboprop	Limitations on altitude and speed. Can work from M=0
5.	Rocket engine	Need to carry all required products for combustion. Complex design. Can work from M=0
6.	Rocket motor	Need to carry all required products for combustion. Relatively simple design. Can work from M=0

As one can conclude from Table 1.1, the most efficient and reliable technology is jet propulsion. However, these engines can operate only within a limited range of velocity. In general, the entire selection of the available propulsion methods can be divided into three segments: subsonic, supersonic and hypersonic. Turboprop and Jet engines are the most efficient in subsonic flight. In fact, turbo-prop engines cannot reach supersonic speeds at cruising speeds. Meanwhile, jet engines with an afterburner can easily reach supersonic velocity but are very inefficient with respect to fuel consumption while at supersonic flight. Therefore, ramjet engines fit perfectly for supersonic applications. And, finally, scramjet engines are ideal for hypersonic applications. Normally, for top performance, Ramjet and Scramjet engines need each other for nominal operation, and also a regular jet engine or rocket propulsion is needed to provide the initial thrust from zero as both of the aforementioned engines can only operate after they have reached supersonic speeds. Ramjet can only start performing from M>3, whereas Scramjet can operate only from M>6 [21, 22].

The most efficient solution to counter the disadvantages of these supersonic jet engines is rocket propulsion which can minimize the take-off and landing distances and reach greater velocities. Such a setup is used for military applications, such as the modified *C-130 Hercules*, or, in research applications, such as *X-15* [23, 24]. However, these hybrid solutions are rarely actually used because of the complexity of the outlined propulsion systems. In parallel with the jet technologies, a standalone rocket propulsion technology has been steadily improved up until it reached a critical point a decade ago [25]. After that point, multiple private companies started to adopt rapid prototyping and simulation technologies in order to serve the emerging supersonic markets that became possible due to an increase in computational capabilities. Such companies as *SpaceX*, *Blue Origin*, *Rocket Lab* or even the volunteer initiative *Copenhagen Suborbital* are capable to develop technologies that previously had only been possible by the superpower states. Because of this, the aforementioned branch of industry became more and more attractive to investors and entrepreneurs. As an example, a private company founded by a student in New Zealand called *Rocket Lab* in 2017, after a series D investment round, raised 75 million USD for their *Electron* rocket development. It is currently estimated that the company is worth around 1 billion USD [26]. These facts clearly illustrate that computer models can not only make the research easier but also bring significant added value on which businesses can capitalize and take a sizable piece of the industry into private hands.

Having said that, it is worth reiterating that the main motivation for this study was to develop a robust rocket system model which is based on a solid-propellant rocket motor. We shall investigate it and compare its validity with the experimental results which were obtained from the RT-400 aerial target system which was designed developed and produced at *Kaunas University of Technology Institute of Defence Technologies*. This model is crucial for the future progress of solid propellant rocket motor research due to the limited resources in terms of construction materials, propellant manufacturing process difficulties, logistical challenges and cost inefficiency because real-world experiments are prohibitively expensive and complicated in comparison with computational methods. The ability to use virtual models and perform various operational scenarios and design changes is one of the key factors that will bring major improvements in solid propellant rocket motor research in the near future.

As can be seen in Table 1.2 below, simulations objectively outweigh the experimental approach in terms of costs, labor and resource; therefore, the motivation for this research is to construct a model that is a nearly perfect digital twin that will allow the author to develop the design and optimize the rocket system more efficiently than it has been possible ever before.

Table 1.2. Comparison of the simulations and experimental approaches

	Simulation	Experiment
Time	Short / semi-short	Long
Cost	Cheap	Expensive
Scalability	Any	Limited
Repeatability	Yes	Limited
Safety	Yes	Limited
Data acquisition	All	Sensor points

1.3. Analysis and internal ballistics of solid propellant rocket motors and its propellants

1.3.1. Key design features of solid rocket motors

Rockets are self-contained propulsion devices in which no intake of air or another oxidizer from the external environment is needed [27]. Chemical rockets contain all the required components for combustion, however, that requires a lot of mechanical components with potential multiple points of failure, whereas solid propellant rocket motors are significantly simpler due to the elimination of fuel and oxidizer plumbing systems, injectors and preheating or cooling solutions for fuel/oxidizer [28]. Solid rocket motors (SRM's) consist of 7 main parts which are shown in **Fig. 1.3.1**. The propellant is contained in the motor casing or liner (if the motor is manufactured by using filament winding techniques). The second main part is the nozzle with a pressure cap. This is mandatory if one has to build pressure in the combustion chamber in order to initiate combustion nominal performance. In most cases, the igniter is attached at the top of the motor (motor head), but in other cases ignition can be initiated by using igniters which are attached from the bottom. This method minimizes the weight of the rocket after lift-off because the igniter stays on the launchpad. For solid-propellant rocket motor nominal operation, sealing of the gaps is crucial. The motor casing, the head and the nozzle joints are fixed with elastic O-rings and other fixing elements.

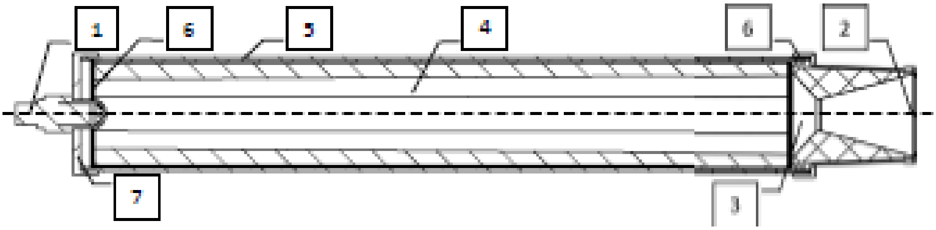

Fig. 1.3.1. Rocket motor assembly: 1 – igniter; 2 – end cap; 3 – nozzle; 4 – propellant grain; 5 – hermetic rings; 6 – fixing ring; 7 – top cap

One of the key design features in comparison with liquid rocket engines is that in the SRM's all the propellant required for the combustion is stored in the combustion chamber. This means that, when combustion starts, the propellant grain burns gradually, layer by layer, and changes the shape and volume of the propellant grain/combustion chamber. With regard to the changing surface area of the propellant grain/combustion chamber, the pressure changes as well, which leads to the change of the thrust of the rocket motor. Such characteristics dictate the design of the grain geometry, and the challenge is to design the grain so that the area of the open surface of the grain would be changing according to the required thrust profile at the transient process of the combustion. Having said that, the casing for the propellant grain has to be made as a pressure vessel type in order to withstand the ever-changing pressure levels in the combustion chamber and keep the SRM intact [29].

As far as numerical models and CFD simulations are concerned, Serraglia (2003) contributed significantly with his work *Modeling and Numerical Simulation of Ignition Transient of Large Solid Rocket Motors*, which investigates ignition problems and ignition related phenomena in great detail. Furthermore, combustion and heat transfer problems were thoroughly researched and simulated by using CFD by Adami *et al*. (2017) and Cai *et al*. (2008). Design issues related to the propellant are mostly concerned with the selection of the propellant type and the mounting and protection of the propellant grain in the casing. It is tricky to design the optimal SRB without numerical models and CFD simulations because, differently from liquid rocket engines, SRBs have no propellant tanks; however, the casing has to contain the propellant and also behave as a combustion chamber. For this reason, a standard booster would have an objectively large casing. Moreover, cooling SRBs are completely different from cooling liquid rockets because there are no liquids involved, and heat dissipation has to be entirely passive. In **Fig 1.3.1**, one can see the rocket motor *RM-12K* which is a propulsion device for the *RT-400* aerial target system (Fedaravičius *et al*. 2016) [30].

Every motor can be classified to a specific class which is related to the motor total impulse. The total impulse it is defined by Eq. 1.1 as the integration of thrust F over the operating duration t_b [31]. In **Fig. 1.3.2**, one can see the definition of the burning time and the action time.

$$I_t = \int_0^{t_b} F dt = \overline{F} t_b \ [N \cdot s] \tag{1.1}$$

where $\overline{F}$ is the average value of thrust over the burning duration t_b. F is the thrust of the SRM.

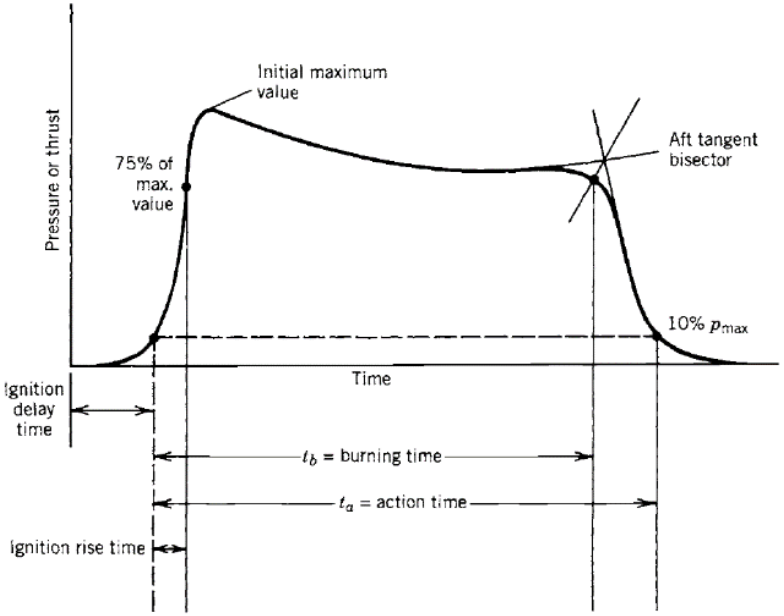

Fig. 1.3.2. Definitions of burning time and action time [31]

As it can be seen from the chart above, the total impulse is defined by eliminating the sliver effect which is described by the aft tangent bisector and excluding the ignition delay time. Action time t_a is defined from the ignition delay time until the sliver burnout time. 10% pressure leftovers in the combustion chamber are considered as gas escaping the combustion chamber, but the propellant grain (sliver) gets fully burned [32]. In Table 1.3, one can see a classification table for various rocket motors [33]. Such a classification is established for regulatory and technical reasons. One must note that the *RM-12K* solid-propellant rocket motor is a class P motor and is considered as a high-power motor.

Table 1.3. Class comparison of rocket motors

Classification	Class	Total impulse, $N{\cdot}s$	Category
Model rocket	$\frac{1}{8A}$	0.01 – 0.3125	Micro
	$\frac{1}{4A}$	0.3126 – 0.625	Low power
	$\frac{1}{2A}$	0.626 – 1.25	
	A	1.26 – 2.5	
	B	2.51 – 5	
	C	5.01 – 10	
	D	10.01 – 20	
	E	20.01 – 40	Medium power
	F	40.01 – 80	

	G	80.01 – 160	
High power	H	160.01 – 320	Level 1
	I	320.01 – 640	
	J	640.01 – 1280	Level 2
	K	1280.01 – 2560	
	L	2560.01 – 5120	
	M	5120.01 – 10240	Level 3
	N	10240.01 – 20480	
	O	20480.01 – 40960	
	P	40960.01 – 81920	
	Q	81920.01 – 163840	

Moreover, as described above, the total impulse describes the potential power output of the motor, however, in order to better understand the performance characteristics, one must know the specific impulse of the motor as well since it effectively describes the motor’s efficiency. The specific impulse in the design of rocket propulsion devices is one of the key factors. This dimension is measured in seconds and is denoted by linear dependence on the square root of the given energy which is obtained from the combustion of the propellant. A simplified version of the equation is presented in Eq. 1.2 [34].

$$Isp = \frac{I}{\dot{m} \cdot g_0} = \frac{F}{\dot{m} \cdot g_0} = \frac{v_e}{g_0} = \frac{\int_0^t F dt}{g_0 \int \dot{m} dt} \quad [s] \tag{1.2}$$

where F – the thrust force of the rocket, I – the total impulse of the motor, ṁ – the Mass flow rate of the exhaust gas from the nozzle, g_0 – gravitational acceleration (9.81 m/s^2).

Another parameter that describes the motor’s efficiency is its thrust-to-weight ratio (TWR). TWR encompasses the relationship between the thrust produced by the motor and the weight of the vehicle in a single dimensionless coefficient. Only when TWR ≥ 1, the vehicle is able to lift-off (at the launchpad). TWR with $x < 0$ values can effectively be used only in non-atmospheric environments where orbital maneuvers need to be implemented. For the RM-12K rocket motor at the average thrust of the motor when it was operating in the steady-state phase, the TWR was about 286, but, taking into consideration that the motor is a part of the RT-400 system, the effective TWR for the rocket with the motor was about 95. One must note that these preliminary values are disclosed only for explanatory reasons where performance characteristics of the motor can be described. In the normal operation, the TWR tends to change during combustion of the motor, and the TWR would be displayed as a trend curve, but not as a constant. By concluding this statement, one can clearly see that the produced TWR of the motor is more than enough for the ability to lift-off the aforementioned rocket and perform its objectives.

$$TWR = \frac{F}{m} = \frac{\frac{dm}{dt} v_e}{m} \quad [dimensionless] \tag{1.3}$$

where F – the thrust force of the rocket, v_e – the escaping gas velocity from the nozzle, m – the mass of the vehicle, dm – the mass flow rate.

Optimizing the rocket is not as simple as maximizing the aforementioned ratios and values. Engineers need to keep in mind the pressure and temperatures that will build stresses within the system which can rupture the motor casing or other parts of the motor. The case must be capable of withstanding the internal pressure stemming from the motor operation, at approximately 3–80 MPa (with regard to the RM-12K rocket motor) with a sufficient margin for safety. The safety factor must be evaluated by performing simulations or static firing testing in order to evaluate pressure fluctuations. Fluctuations may indicate an inadequate mixture composition of the fuel-oxidizer in the propellant grain. Besides the stresses due to the pressure in the chamber, thermal stresses may sometimes be critical, and, when the case also serves as a flight vehicle, the bending loads and inertial forces, such as spinning (passive-active stabilization solutions), play an important role in determining the thickness and the material of the motor case as well [35]. For these reasons, motor cases are usually made either from metal (high resistance steel or high strength aerospace-grade aluminum alloys), or composite materials (fiberglass, polymer fibers, carbon).

1.3.2. Common types of solid rocket propellants

Solid propellant motors, differently from liquid-propellant engines, are denoted by a wide range of composition, separate fuel, and oxidized chemicals are used, which are thoroughly mixed in the grain. It can be made as monopropellant from nitrocellulose or double-base propellants or oxidizer-binder combinations as APCP or ANCP propellants. The oxidizer is usually ammonium nitrate, potassium perchlorate, or ammonium perchlorate, and it often comprises as much as four-fifths or more of the whole propellant mix. The fuels in use are metals, hydrocarbons, such as asphaltic-type compounds, or plastics. As the oxidizer has no significant structural strength, the propellant must not only perform well but must also supply the necessary form and rigidity to the grain. Having said that, much of the research in solid propellants is devoted to improving the physical as well as the chemical properties of the fuel. It is worth highlighting that one fact which unites all these different composition motors is that there is no possibility to shut down the motor when the propellant grain is in the combustion phase. For this problem, thrust vectoring is achieved by casting propellant grains with special geometrical properties.

Solid propellant rocket motors Isp are in the range of 150 s – 320 s. For example, Space Shuttle Solid Rocket Booster Isp is 242 s (sea level), Zefiro 23 booster used in Vega launch vehicle is 289 s and Zefiro 9A is 294 s, Orion 38 (Pegasus launch vehicle) is 287 s and Orion 50XL is 289 s, SR-118 (Minotaur launch vehicle) is 282 s, and SR-120 is 300 s [36, 37]. Despite their relatively low specific impulse in comparison with liquid rocket engines, solid motors are much cheaper to produce, reliable, less complex, and, in most cases, they are the propulsion device of choice in military applications, especially for single stage motors or solid rocket boosters, such as the solid rocket motor missile AIM-120 which is used in the NASAMS (*Norwegian Advanced Surface to Air Missile System*) air defence system [38] or *Atlantic Research*

MK 106 in the Tomahawk (RGM/UGM-109C/D) missile which is used as a solid rocket booster [39, 40]. The cost efficiency is clearly noticeable for solid propellant rocket motors. The data is provided as specific impulses for all the 4 stages of *Scout G1*– stage 1: Algol 3 – 238 s, stage 2: Castor 2 – 232 s, stage 3: Antares 3A – 295 s, stage 4: Altair 3 – 255 s, [41] Pegasus 3 out of 4 stages solid (4th stage is optional) – stage 1: Orion 50SXL – 295 s, stage 2: Orion 50 – 289 s, stage 3: Orion 38 – 287 s, [42] Long March 3 stage 3 – 298 s, Delta boosters – 245 s – 273 s [43]. The specific impulse of these solid rocket motors is in the range from 238 s to 295 s, which correlates perfectly to solid rocket motors Isp versus the thrust-to-weight ratio pool.

When considering the propellant which would be most suitable for the research, three different propellant types were reviewed. This was done to conclude which propellant type would be optimally cost-efficient to produce, and could assure grain stability and manufacturability. The first candidate was black powder propellants, the second candidate was double-base propellants, and the third option was composite propellants.

The Dark Powder solid rocket propellant is composed of charcoal (fuel), potassium nitrate (oxidizer), and sulphur (additive), black powder is one of the oldest pyrotechnic compositions with application to rocketry. The primary difference is the existence of the binder, normally dextrin. In modern times, black powder finds use in low-power model rockets as it is cheap and fairly easy to produce. The propellant grain is typically a mixture of pressed fine powder with a burn rate that is highly dependent upon the exact composition and operating conditions. Motors designed with black powder are most frequently end-burners because of the rapid burning charge of the propellant. Due to its sensitivity to fracture and poor performance (a specific impulse around 80 s), BP does not typically find use in motors above 40 Ns. The simple dextrin-free variant (the most commonly applied compound) comprises 75% potassium nitrate, 10% sulphur, and 15% carbon. Dextrin may be brought as desired (normally between 0 and 5 percent). Extra (coarse) carbon or metal powders (5–10 percent) may be added to find a beneficial light course. However, that may vary somewhat the burn rate of the mix [44].

Double-Base propellants are composed of two monopropellant fuel elements where one typically acts as the unsteady, high-energy monopropellant, whereas the second element acts as the lower-energy stabilizing (and gelling) element. The monopropellant normally consists of nitrocellulose and nitro-glycerine, to which, the plasticizer is added. DB propellants are applied in applications where minimum smoke is needed yet medium-high Isp is needed, which is around 210 s – 235 s. Their primary goal is that they do not create any traceable gas and are, thus, usually utilized in tactical weapons. They are also frequently used to perform functional purposes, such as jettisoning the spent components when dividing one stage from another.

The aging of DB propellants, which is the result of material reactions and physiological operations that happen over time, has a considerable consequence on their relevant properties (e.g., material composition, mechanical and ballistic properties). These changes of related attributes determine the good and reliable delivery life of DB rocket propellants. That is the reason why many research efforts are dedicated to finding reliable methods so that to evaluate the changes caused by aging, to determine this level at a given point of time, and to predict the remaining lifetime of DB rocket propellants [45].

The composite propellants that are frequently used are either ammonium nitrate-based (ANCP), or ammonium perchlorate-based (APCP). The ammonium nitrate composite propellant frequently utilizes magnesium and/or aluminum as fuel and delivers ISP of around 180 s – 250 s [46], whereas the ammonium perchlorate composite propellant frequently utilizes aluminum fuel and delivers high performance (vacuum Isp up to 296 s with a single piece nozzle or 304 s with a high area ratio nozzle) [47]. Composite propellants are cast, and they retain their shape after the rubber binder, such as Hydroxyl-terminated polybutadiene (HTPB), cross-links (solidifies) from the addition of a curing agent. Because of its high performance, moderate ease of manufacturing, and moderate cost, APCP finds widespread use in space rockets, military rockets, and hobby as well as amateur rockets, whereas the cheaper and less efficient ANCP finds use in amateur rocketry and gas generators. Ammonium dinitramide, $NH_4N(NO_2)_2$, is being considered as a 1-to-1 chlorine-free substitute for ammonium perchlorate in composite propellants. Unlike ammonium nitrate, ADN can be substituted for AP without a loss in motor performance. The ammonium perchlorate composite propellant is typically employed in aerospace applications, where ease and dependability are desired, and specific impulses (dependent on the arrangement and operating thrust) of 180–260 seconds are adequate. Because of these process properties, APCP is regularly applied at booster applications, e.g., in this area, Shuttle Solid Rocket Boosters, spacecraft ejectors, and specialty area exploration applications such as NASA’s Mars exploration Rover descent stage retro-rockets are involved. Additionally, the high-power rocketry group regularly employs APCP in this manner of a commercially accessible propellant, also as single-use motors. Experienced researchers and amateur rocketeers also frequently work with APCP thus making APCP by themselves [48].

Ammonium Nitrate (AN) is the cheapest and most readily available oxidizer for Solid rocket propellants compositions. Its composition of the high oxygen quantity (60% Oxygen, 5% Hydrogen, and absence of halides), high thermal stability, low smoke profile, and sufficient capability with a number of other constituents makes it the oxidizer of choice for low-cost missions [49]. The oxidizers which are used in solid propellants are those which have weak bonds with small atomic number elements. Ammonium Nitrate, NH_4NO_3, has a combustible element – hydrogen – which oxidizes to water upon thermal disintegration according to the following reaction [50]:

$$NH_4NO_3 \rightarrow 2H_2O + N_2 + \frac{O_2}{2} \tag{1.4}$$

By this relation, the author of this thesis considers that free oxygen in ammonium nitrate in percentages is 20% which is almost the same as the air in the atmosphere where the oxygen percentage is almost 21% [51]. One concludes that in order to burn 1 kg of bitumen, it is necessary to have 15 kg of ammonium nitrate. Such a propellant would have 97% ammonium nitrate and only 3% of bitumen and would not be suitable for medium-high power rocketry applications. This issue was solved by introducing Aluminum as fuel. Aluminum is a stable element (metal), which, upon reacting with oxygen, produces high energy combustion. Such a propellant only needs 40–80% of oxidizer and 5–25% of fuel [52]. This type of propellant must have a binder material which shapes and binds the fuel/oxidizer mixture in the propellant grain. This type of propellant where the binder is used is called composite propellants, or, in this particular case, the Ammonium Nitrate Composite Propellant (ANCP). Ammonium nitrate propellants have a specific impulse range in between 180 s – 250 s, but, in most cases, where no hazardous and complex additives are used, the specific impulse is in the range between 180 s – 220 s. In Table 1.4, one can compare the AN based propellant with the AP based propellant.

Table 1.4. Theoretical performance of Typical Solid Rocket Propellant combinations [53]

Oxidizer	Ammonium nitrate	Ammonium perchlorate 78% – 66%	Ammonium perchlorate 84% - 68%
Fuel	11% binder; 7% additives	18% organic polymer binder 4% – 20% aluminum	12% polymer binder 4% – 20% aluminum
Density ρ, (kg/m^3)	1510	1690	1740
Absolute temperature T, (K)	1282	2816	3371
Characteristic velocity c*, (m/s)	1209	1590	1577
Molecular mass m, (kg/kg-mol)	20.1	25	29.3
Specific impulse Isp (s)	192	262	266
Specific heat ratio γ (-)	1.26	1.21	1.17

By having extensively reviewed the candidate propellants, a conclusion was made to produce the grain by using a composite AN type propellant due to its relatively high energetic properties, grain stability, and a low decomposition rate during the storage and cost-efficiency with regard to manufacturability. One must note that, when testing the specimens for the AN based composite propellant, it was found that the propellant during the storage period (which lasted from one to five years) maintained similar energetic properties. From such optional tests, the conclusion was drawn that the propellant is able to maintain its initial properties during extensive storage periods. An additional note is required to present which concludes the previous one. The tests of the ANCP specimens were done as additional research and were not related to the main objectives of this research.

The graph below depicts multiple formulations of the solid rocket propellant using varying amounts of AN, aluminium, and binder. Even though the relatively well-known *Wickman* formula within the solid propellant community is comprised of PSAN (phase-stabilized AN), magnesium powder, and R-45 polymer, here the researchers opted for aluminum because of the high energy it produces during the combustion and – of course – additional safety and cost benefits. However, due to the difficulty with combusting particles of aluminum because of the tough shell of aluminum oxide (alumina) that encases the readily oxidized metal, it is paramount to optimize the composition of the binder. The binder is meant to increase the combustion and stabilize its rate. The commonly used additives for this purpose are Sulphur and Red iron oxide, as used by NASA's *Space Shuttle Booster Propellant*. This graph depicts twenty-one different formulations marked by hollow circles together with the actual formulation used for the RM-12K solid propellant marked by the opaque circle [52].

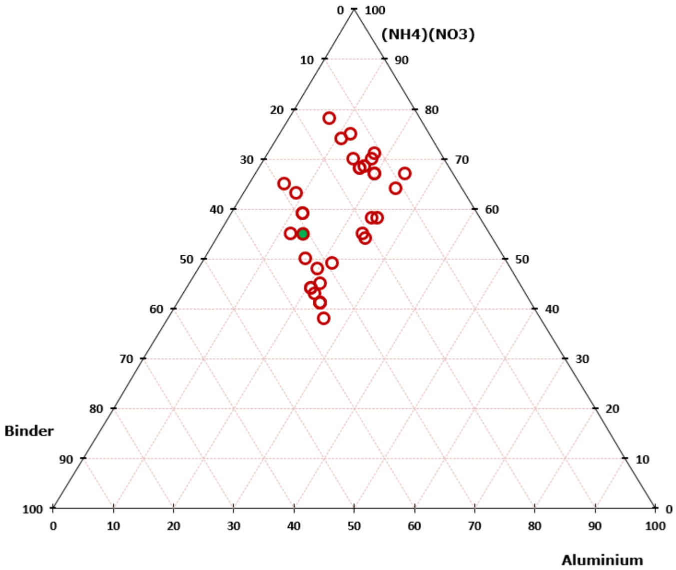

Fig. 1.3.3. Ternary plot of ANCP various compositions

From the graph, one can see an interesting pattern formation which, for the purpose of this discussion, may be called the 'safety isle'. Every dot on the graph represents a 'successful' formulation – in the sense that the resulting propellant was able to start the combustion and get combusted or to be able to combust without exploding. Therefore, when looking at the resulting pattern, one can conclude that any variation of AN, aluminum and binder within the 'safety isle' could, potentially be a valid propellant with a different specific impulse. Furthermore, one can see that, for a solid propellant to be a viable option for the rocket motor, it has to contain anywhere between 7% and 25% aluminum, 38% and 80% of AN, and 8% to 38% of Binder. It is important to note, however, that even within the ranges provided by the research, it is possible to obtain a formulation that would not combust or potentially explode, as the actual 'safety isle' is more like a 'U' shape pattern rather than an uninterrupted area as seen in the graph. As the addition, one must conclude that such variations in the fuel, oxidizer and binder can lead to different performance of the propellant where the limits of the motor mechanical integrity could be surpassed. In case of RM-12K, the propellant was used to be less energetic, but more stable regarding the burn rate, where pressure fluctuations were small, and combustion was more stable. Such a formulation allows to have a margin of safety for the mechanical components of the rocket motor only by sacrificing a small amount of power in order to achieve better stability.

1.3.3. Thrust characteristics of solid propellant grains

Solid propellants in the solid rocket motors are used in forms called grains. The structure and size of the propellant's shape determine the burning time, the quantity of fuel, and the combustion rate originating from the combusting propellant and, as a result, thrust profile.

The combustion duration of the propellant is defined by the burning rate of the propellant and the thickness of the propellant grain. The surface area of the grain changes during the combustion process with respect to the shape of the grain; therefore, the thrust may be either high (but with the low combustion duration), or low (but combustion extends over a longer period of time). In reality, combustion characteristics are not that binary as it is possible to moderate the combustion duration and thrust in non-linear patterns by creating specific grain shapes depending on the mission requirements.

The burn rate is influenced by the Combustion chamber pressure, the initial temperature of the propellant grain, the velocity of the burning gas falling parallel to the burning surface, the local static pressure, the motor acceleration, and the spin. These elements are discussed below.

The burning layer of the rocket propellant grain recedes in the way perpendicular to the wall of the propellant grain. The pace of regression, typically measured in millimeters per second, is termed the *burn rate*. The burn rate may differ significantly for different propellants and within a variety of operating conditions. Recognizing quantitatively the burning rate of the propellant, and how it changes under different circumstances is of the most important aspects in the successful design of the optimal rocket motor performance.

The optimal propellant grain must not only develop the desired particular performance, but it must also demonstrate adequate mechanical properties to withstand high pressure from the combustion chamber and the temperature caused by chemical reactions by the combusting propellant. Otherwise, the propellant grain is at risk of producing a crack with an explosion as a likely consequence [54]. The paragraphs below discuss different propellant grain designs and their influence on SRM performance. The five different propellant grain types were reviewed, which were, specifically, Rod and tube, Tubular, Multi fin, Dual composition, and Star. The main interest was directed towards these grains which could enable us to achieve a neutral-like thrust profile or a semi-constant thrust profile. It is worth noting that an additional grain type which is progressive or regressive was reviewed for the reasons of comparison.

The traditional rod-in-tube (R-I-T) propellant grain (**Fig. 1.3.4**) pattern involves two casting processes, one for the rod part of the propellant grain, and the other for the tube part. The mechanical assistance device is also needed for the rod part of the grain. This device increases the motor's weight; However, irrespective of this additional weight, the R-I-T propellant grain offers the so-called burning neutrality, which is suitable for some operations.

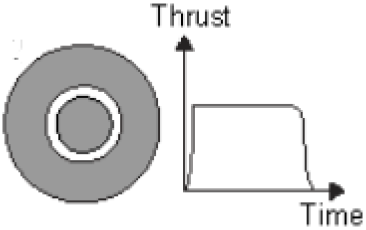

Fig. 1.3.4. Rod and Tube propellant grain cross-sectional view [55]

A slight improvement on the aforementioned design is the single cast Rod-in-tube solid-propellant rocket motor grain. It creates burning neutrality, which produces a minimum propellant sliver during the combustion. The main advantage of this improved design is that, while being single cast, it does not deliver the additional weight of the mechanical assistance device as the rod is cast into the tube.

Tubular grain (**Fig. 1.3.5**) is one of the simplest solid propellant grains. The simplicity of the design makes the fabrication process relatively simple as it does not require sophisticated machinery and casting molds.

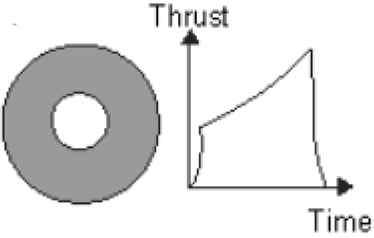

Fig. 1.3.5. Tubular propellant grain cross-sectional view [55]

The grain thrust curve is progressive and leaves virtually no sliver. However, the practical implementation of this strategy is limited because the progressive thrust curve behavior has aerodynamic inefficiencies for low altitude applications, where the drag forces limit the performance of the rocket and create high aerodynamic pressures on the rocket shell.

The key features of the Multi-fin solid propellant grain (**Fig. 1.3.6**) type are the high thrust and the short burn duration, and the curve of such a combustion profile is called ‘dual thrust’. Such a type of the propellant grain is used where the motor needs a short, rapid burst to propel the object.

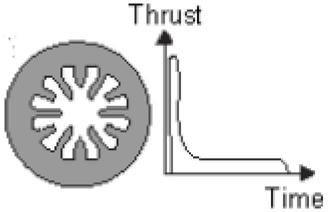

Fig. 1.3.6. Multi-fin propellant grain cross-sectional view [55]

The most common application for this grain type is to launch escape systems, where a short, powerful burst is desired to detach the crew cabin from the launch vehicle in case of an emergency.

The Dual composition solid propellant grain type is based on the ‘cross’ shape cut-out. Such a design is based on the regressive thrust cure behavior (**Fig. 1.3.7**).

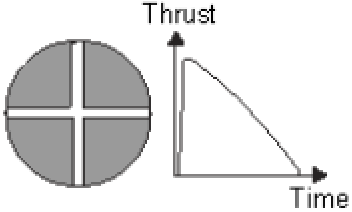

Fig. 1.3.7. Dual composition propellant grain cross-sectional view [55]

The Dual composition propellant grain type initially has a large surface area which progressively gets smaller during the combustion, which means that the thrust is getting progressively lower as well.

The Star type propellant grain is the neutral thrust curve type grain (**Fig. 1.3.8**). The thrust curve behavior is similar to the rod and tube propellant grain type, but the item is easier to fabricate and features superior mechanical properties because of the monolithic nature of the cast, unlike in the Rod in tube design.

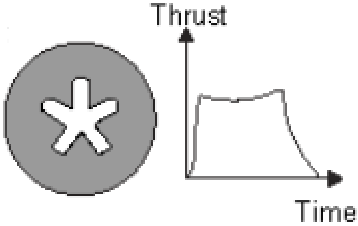

Fig. 1.3.8. Star propellant grain cross-sectional view [55]

Some variations are possible for the star-shaped propellant grains, such as making fillets on the star spikes in order to control the sliver influence at the end of the steady-state combustion process, but such enhancements make the fabrication harder, which can lead to crack development near the fillet regions. In the Star-shaped propellant grain, the spikes of the star are placed in such a configuration that the burning surface is semi-constant during steady-state combustion; therefore, it produces a steady (neutral) thrust [56].

1.3.4. The impact of the converging-diverging rocket nozzle on the solid rocket motor performance

A nozzle is a tube of varying cross-sectional area which is positioned at the end of the rocket motor with the aim to increase the velocity of the outflow of the gases. The nozzle is as important to the rocket motor as the propeller is to the shaft-engine propulsion systems because it converts and amplifies the thermal energy produced by the burning grain of the motor into the kinetic energy required to generate relative motion. This relative motion is created in the simplest case by ejecting the mass back through the nozzle from the chamber with the reaction forces acting mainly on the opposite chamber wall with a small contribution from the nozzle walls.

It is said that the nozzle begins where the chamber diameter begins to decrease. Since the flow within the nozzle is very fast, it can be considered as adiabatic to the first approximation, therefore the isentropic model is a good enough assumption for preliminary design calculations and simulations of the rocket motor nozzle.

When it comes to nozzle design configurations, several different well-researched options with varying geometries and performance are available today. Since the inlet shape, the contour of the throat or the inlet angle are not very critical for performance, the main factors to be considered while choosing the nozzle design are the actual shape of the nozzle extending from the throat (the narrowest point in the nozzle) to the divergent section, as depicted in **Fig. 1.3.9**. The first three sketches depict the more commonly used conical and bell-shaped nozzles, whereas the final three types – although well researched and abundant in literature – have never been used in a commercial rocket design yet.

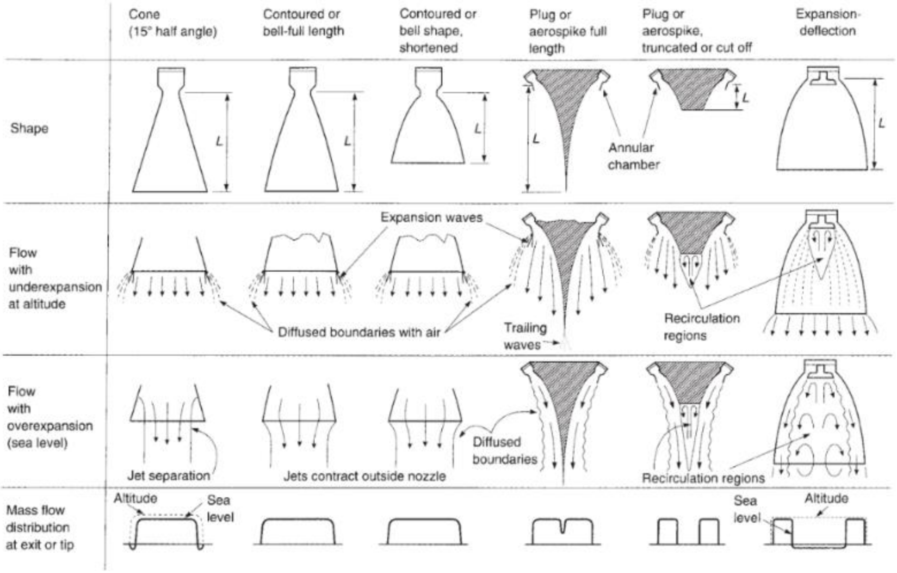

Fig. 1.3.9. Simplified diagrams of different generic nozzle configurations and their flow effects [57]

The bell nozzle (**Fig. 1.3.10**) is the most common nozzle in the rocket propulsion research and development. Such a type of the nozzle allows enhancing the velocity of the combustion products in the most efficient way. Even though this nozzle is highly efficient in converting the thermal energy into the thrust momentum, it can be optimized only for a specific range of altitudes, beyond which, the performance may suffer significantly. As a result, staging is required to eliminate this disadvantage where another bell nozzle is introduced which would be designed for a different altitude range or even vacuum. One must note that it is possible to extend the altitude range of the bell nozzle by creating the so-called dual-bell profile where two shock zones can appear in different altitude ranges [58].

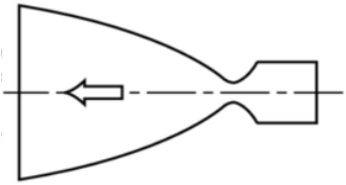

Fig. 1.3.10. Bell nozzle [58]

The conical nozzle is one of the simplest nozzles to fabricate. Due to its simplicity, it is less efficient than the bell nozzle. However, such inefficiency is marginal (around 1%) stemming mainly from shock misalignment.

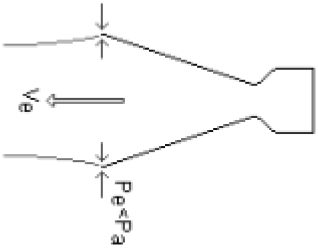

Fig. 1.3.11. Conical nozzle [58]

The aerospike nozzle is most unique in comparison with the others described above. Even though technically it is an inverted bell nozzle, however, it does not have to be radial as the cross-section of the said nozzle can also be linear without any specific length limitations. As a result, such a design allows to eliminate altitude inefficiencies but involves a potential risk of getting clogged by the combustion residue. Additionally, it suffers from one of the most complicated fabrication processes.

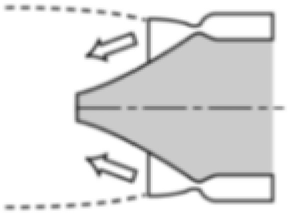

Fig. 1.3.12. Aerospike nozzle [58]

1.3.5. Discussion on nozzle selection

The three final nozzles as depicted in **Fig. 1.3.9** were discounted early in the process as viable options for the RM-12K rocket motor due to their intrinsic properties geared towards performance benefits in the high-altitude, lower atmospheric pressure conditions. The aforementioned nozzles achieve better results in the high altitude due to the central body inside the nozzle that provides altitude compensation, which means that the hot-gas boundaries outside the nozzle can grow even when the outside pressure decreases thus allowing for a better optimized expansion with an increase in altitude. Since the RM-12K motor is designed for low-altitude (up to 2.2 km) conditions, the benefits of these nozzles would not be pronounced enough to justify the complex fabrication techniques required in order to manufacture the nozzles.

The first three nozzles as depicted in **Fig. 1.3.9** were thoroughly researched and simulated mathematically. Although the bell-shaped/contour nozzles are the closest shape to the ideal nozzle shape which can be calculated by using the prescribed motor design parameters, we have chosen the conical nozzle. This nozzle is the oldest and perhaps is of the simplest configuration. The main reason for choosing it was the simplicity in fabrication and the fact that its shape would not need to change if the propellant grain properties changed. However, when simulating the flow with the conical nozzle – assuming ideal conditions where the isentropic flow is achieved – the theoretical correction factor λ must be applied to the nozzle exit momentum. This factor is the ratio between the momentum of the gases exhausting with a finite nozzle angle 2α and the momentum of the ideal nozzle with all the gases flowing in the axial direction:

$$\lambda = \frac{1}{2}\left(1+\cos\alpha\right) \tag{1.5}$$

For ideal rockets, λ is 1.0. However, in this case – due to the divergence cone angle of 30° (half angle α = 15°) – the exit momentum and, therefore, the axial exhaust velocity will be 98.3% of the calculated velocity assuming the ideal conditions. Small nozzle divergence angles may allow most of the momentum to remain axial and thus produce high specific impulses, but they result in long nozzles thus introducing performance penalties in the rocket propulsion system and the vehicle mass amounting to minor losses. Larger divergence angles give shorter, lightweight designs, but their performance may become unacceptably low. Depending on the specific application and the flight path, there is the optimum conical nozzle divergence value (typically between 12° and 18° half-angle) [60].

Therefore, taking the aforementioned factors into consideration, we designed the current nozzle with the aim to minimize the frictional effects, flow disturbances, and circumstances that may lead to shock failures. A CAD representation of the nozzle design is shown in **Fig. 1.3.13**.

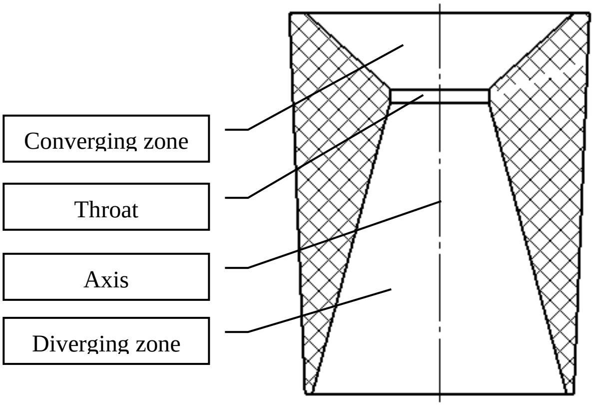

Fig. 1.3.13. Cross-sectional view of the nozzle

All in all, the selected conical shape of the nozzle with a standard divergence factor of 15° has proven to be a prudent decision that minimizes fabrication costs and still provides the optimal performance with the given rocket motor design and mission parameters.

1.3.6. 1D isentropic model study of the nozzle

The 1D isentropic model assumes that the nozzle flow is one-directional and axisymmetric. It allows simplifying the calculations in order to obtain parameter values in ideal conditions. When using this model, the nozzle shape is irrelevant, and the flow depends only on the cross-section area ratios. For this concept, the method of characteristics of the ideal propulsion system is useful because the required thermodynamic principles can be expressed with simplified mathematical models thus doing away with two- or three-dimensional equations of the real aerothermal chemical behavior. Taking into account a few assumptions required to achieve the isentropic model, the resulting values are satisfactory for studying rocket propulsion systems as well as testing and evaluating various prescribed design parameters.

The main assumptions used in performing the calculations are as follows:

1. There is no heat transfer across any and all gas-enclosure walls; therefore, the flow is adiabatic.
2. There is no appreciable wall friction, and all boundary layer effects may thus be neglected.
3. There are no shock waves or other discontinuities within the nozzle flow.
4. The solid propellant is homogeneous and uniform, the burning rate is steady.
5. All the exhaust gases leaving the rocket nozzle travel with a velocity parallel to the nozzle axis.
6. The gas velocity, pressure, temperature, and density are all uniform across any section normal to the nozzle axis (the combustion chamber).

We note that ideal isentropic conditions imply that no losses occur within the flow, whereas the optimum conditions are a separate concept reflecting the best-calculated performance at a particular set of prescribed parameters.

1.3.7. Nozzle flow equations

When constructing a model, it is paramount to calculate the model characteristics mathematically beforehand so that the obtained results could be used to validate the model. Even though the experimental approach theoretically provides the most accurate results for validation, however, sometimes, the experimental approach can be difficult to rely on because of the different test conditions and difficult to accurately measure various parameters due to physical constraints. The best practice is to compare both – experimental results and calculated results – in order to validate whether the rocket motor is predictable enough according to the mathematical assumptions.

Having said that, it is crucial to estimate the motor’s thrust. To calculate the thrust of the rocket, first of all one needs to calculate the pressure, velocity, mass flow, temperature, and the optimal efficiency of the nozzle. Since the nozzle transfers thermal energy into kinetic energy, it is the best practice to feed the static combustion chamber pressure and temperature as the initial input into the equations and calculate the remaining values with regard to other predefined design characteristics. One must note that the main parameters which rely on such calculations are the specific heat ratio, nozzle throat, and exit areas.

We take into account that the calculations were done for the conical nozzle (they can also be applied for the bell nozzle). The minimum nozzle cross-sectional area is referred to as the *throat* and is denoted as t or * (an explanation will be presented below).

Knowing the aforementioned values enables us to calculate the thrust and mass flow rate and to determine where the shock occurs, which tells us how well optimized the flow produced by the nozzle really is.

A converging-diverging nozzle flow starts with the converging section where $M < 1$ (M refers to a dimensionless Mach number), then narrows down to the throat where $M = 1$, and finally diverges to the exit where $M > 1$.

When assuming that the flow is isentropic along with the nozzle, we can calculate the effectiveness of the nozzle by obtaining values for the temperature ratio, the exit speed, and the mass flow rate. In the converging-diverging nozzle used for the supersonic flow, both the throat area and the exit area should be optimized for the maximum thrust as a function of altitude and the flight speed.

In the RM-12K rocket motor, the chamber pressure was p_c: 6.08E+06 Pa, the Chamber temperature equaled T_c: 2322K, the Coefficient of heats (γ) was 1.19, and R is given as 347.9 J/kg/K. The following calculations will assume a rocket operating near the sea level with an ambient pressure of 101.3E+03 Pa. The radius of the throat is 44 mm, and the radius of the nozzle exit is 114 mm.

In the following equations, the notations are as follows: T_t (or T^*) – gas temperature at the throat of the nozzle, T_e – gas temperature at the exit of the nozzle, p_t (or p^*) – gas pressure at the throat of the nozzle, p_e – gas pressure at the exit of the nozzle, γ – specific heat ratio of the gas, A_e – area at the exit of the nozzle, v_e – gas velocity at the exit of the nozzle, R – gas constant, $\dot{m}$ – mass flow rate of the combustion gas through the nozzle, M_e – Mach number at the exit of the nozzle. One must note that the abbreviation for t and * is dedicated to describing the variable at the throat level (t) and the critical variable at the throat level (*), respectively. In addition, one must note that t and * in the ideal system should be the same, but in a real system * can shift from t due to instabilities and the chaotic nature of the combustion processes where combustion products are not perfectly homogenous with regard to the pressure, density and temperature of the occurring process.

In order to estimate the effectiveness of the nozzle, the objective is to find the flow conditions at the throat and at the exit for a given set of the observed and calculated parameters [61]:

$$\dot{m} = \rho^* v^* A^* = \frac{p^*}{RT^*}\sqrt{\gamma RT^*}A^* = \frac{\gamma p^* A^*}{\sqrt{\gamma RT^*}} = \frac{\gamma p_t A^*}{\sqrt{\gamma RT_t}}\left(\frac{2}{\gamma+1}\right)^{\frac{\gamma+1}{2(\gamma-1)}}, \tag{1.6}$$

$$\dot{m} = \rho_e v_e A_e = \frac{\gamma p_t A_e}{\sqrt{\lambda RT_t}} M_e \left(1+\frac{\gamma-1}{2}M_e^2\right)^{\frac{2-\gamma}{2}}, \tag{1.7}$$

$$M_e = \frac{v_e}{\sqrt{\gamma R T_e}}, \tag{1.8}$$

$$F = \dot{m} v_e . \tag{1.9}$$

In the converging-diverging nozzle used in the supersonic flow, both the throat area and the exit area should be optimized for the maximum thrust as a function of the altitude and flight speed. As seen in the equation below:

$$\frac{A^*}{A_e} = M_e \left(\frac{\frac{\lambda + 1}{2}}{1 + \frac{\gamma - 1}{2} M_e^2} \right)^{\frac{\gamma+1}{2(\gamma-1)}} . \tag{1.10}$$

When the flow is isentropic all along with the nozzle, i.e., for values of p_0/p_t, the exit Mach number M_e is given by [61]:

$$M_e = \sqrt{\frac{2}{\gamma - 1}\left(\left(\frac{p_t}{p_e} \right)^{\frac{\gamma-1}{\gamma}} - 1 \right)} . \tag{1.11}$$

With the given motor characteristics, pressure p* at the throat is 5.73E+06 Pa.

$$P_t = \left(\left(\frac{2}{\gamma + 1} \right)^{\frac{\gamma}{\gamma-1}} \right) E_i . \tag{1.12}$$

One must note that E_i in Eq. (1.11) stands for the specific internal energy of gas, and its value is 10.11E+06 J/kg.

$$E_i = \frac{2 T_c R \gamma}{\gamma} \tag{1.13}$$

For p_e calculation, one must note that it has to be equal or close to the ambient pressure. In this case, p_e was 1.01E+03 Pa since the test was conducted on the ground (at the sea level).

Given the aforementioned values, the resulting exit Mach number (M_e) was calculated as 2.97 Mach, which is consistent with the cross-referenced value from the A^*/A_e graph depicted and explained at the end of this section.

Having obtained the chamber temperature which was taken from chemical kinetics calculation, the velocity at the throat v^* was 937 m/s.

$$v^* = \sqrt{\frac{(2 \gamma R T_c)}{\gamma + 1}} \tag{1.14}$$

Having determined the throat temperature and the exit Mach number, one can calculate the exit velocity. This value is one of the key values in order to calculate the motor's thrust. The exit velocity was 2204 m/s.

$$v_e = \sqrt{\frac{2 \gamma R T_t}{\gamma - 1}\left(1 - \left(\frac{p_e}{p_t} \right)^{\frac{\gamma-1}{\gamma}} \right)} = \sqrt{\frac{2 \gamma R T_t}{\gamma - 1}\left(1 - \frac{1}{1 + \frac{\gamma - 1}{2} M_e^2} \right)} \tag{1.15}$$

The throat temperature rate of change is described as the specific internal energy which is the internal energy divided by the mass. This value describes the rate of change from the thermal energy which is produced in the combustion chamber to the kinetic energy which produces the thrust for the rocket motor. The value of the rate of change was denoted as $E_i = T^*$ and was equal to 10.11E+06 J/kg.

$$T^* = \frac{(2\gamma R T_c)}{\gamma - 1} \tag{1.16}$$

Upon having obtained the chamber temperature, the ambient pressure and the chamber pressure, one can calculate the exit temperature. This shows how much the temperature decreases when it leaves the rocket nozzle. One can note that this can clearly show how the thermal energy is dissipated in the nozzle when the thermal energy is transferred to the kinetic energy. The exit temperature was calculated as 1207.8 K.

$$T_e = T_c \left(\frac{p_0}{p_c} \right)^{\frac{\gamma - 1}{\gamma}} \tag{1.17}$$

Mass flow rate and thrust calculations are presented in Eq. (1.7) and Eq. (1.9). Given the resulting values above, the mass flow rate was $\dot{m} = 5.424$ kg/s, and thrust F = 11952.65 N. The calculated thrust value is consistent with the empirical and simulation data. One can confirm other values by the drawings area, pressure and temperature ratio graphs as a function of the Mach number in order to test whether the values obtained by the calculations can be found on those graphs, which would suggest that the values are accurate enough for preliminary design calculations [61].

Table 1.5. Calculated values of the rocket motor nozzle

Altitude, m	1
Coefficient of Heats, γ, -	1.19
Gas constant, R, j/kg/K	347.9
Exit pressure, p_e, Pa	1.01E+03
Pressure ratio, p_t/p_e	0.0167
Temp Ratio, A_t/A_e	0.52
Density Ratio, ρ_e/ρ^*	0.04
Rate of change, T*, J/kg	1.01E+07
Throat pressure, p_t, Pa	5.73E+06
Throat velocity, v_t, m/s	937
Exit velocity, v_e, m/s	2204
Mass Flow rate, $\dot{m}$, kg/s	5.42
Thrust, F, N	11952.65
Exit temperature, T_e, K	1207.8
Exit speed of sound, v_M, m/s	707
Exit Mach, M_e, -	2.97

The nozzle area ratio A_*/A_e is defined by dividing the nozzle local area by the nozzle throat area, and this ratio is in the range from 0 to 1 across different Mach values (Eq. (1.10)).

For this design, A^* was 0.00152 m², and A_e was 0.0102 m² with the 0.1489 area ratio. The area ratio of the developed RM-12K rocket motor is presented in the figure below (**Fig. 1.3.14**).

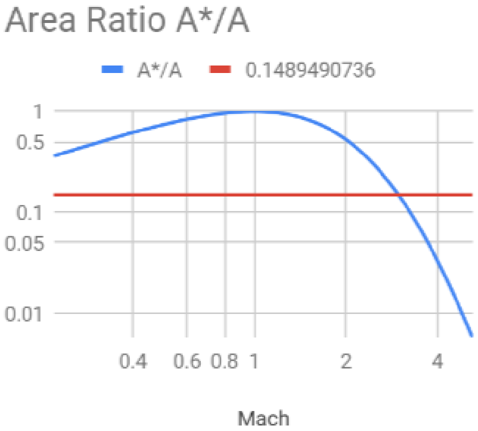

Fig. 1.3.14. Area ratio of the nozzle of the designed rocket motor

The nozzle pressure ratio p_e/p^* is defined by dividing the nozzle local pressure by the nozzle throat pressure across various Mach values.

$$\frac{\rho}{\rho^*}=\frac{\frac{\gamma+1}{2}}{\gamma-1\sqrt{1+\frac{\gamma+1}{2}M_e}} \tag{1.18}$$

For this design, p^* was 5.73E+06 Pa, and p_e was 1.01E+03 Pa with the 0.0167 pressure ratio. The pressure ratio of the developed RM-12K rocket motor is presented in the figure below.

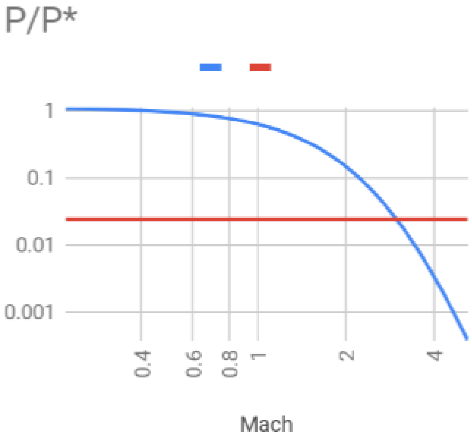

Fig. 1.3.15. Pressure ratio of the nozzle of the designed rocket motor

The nozzle temperature ratio T_e/T^* is defined by dividing the nozzle local pressure by the nozzle throat pressure across various Mach values. For this design, T_c was 2322 K, and T_e was 1207 K with the 0.52 temperature ratio. The area ratio of the developed RM-12K rocket motor is presented in the figure below.

$$\frac{T^*}{T} = \frac{1+\frac{\gamma-1}{2}M^2}{\frac{\gamma+1}{2}} \tag{1.19}$$

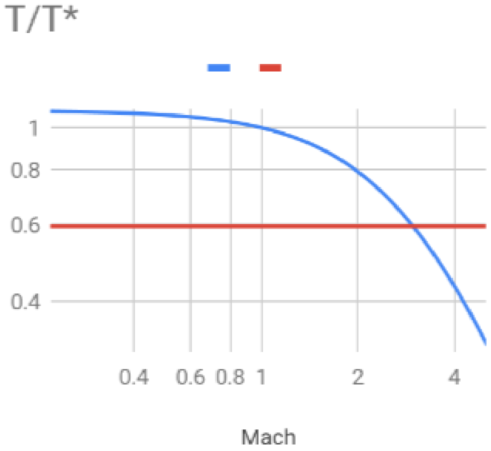

Fig. 1.3.16. Temperature ratio of the nozzle of the designed rocket motor

For this design, ρ^*/ρ_e ratio was 0.04. The area ratio of the developed RM-12K rocket motor is presented in the figure below (**Fig. 1.3.17**).

$$\frac{\rho}{\rho^*} = \frac{\frac{\gamma+1}{2}}{\gamma-1\sqrt{1+\frac{\gamma+1}{2}M_e}} \tag{1.20}$$

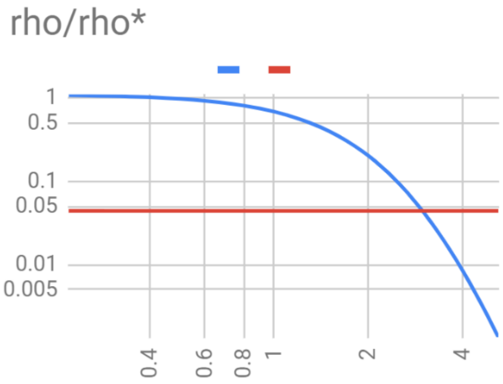

Fig. 1.3.17. Density ratio of the nozzle of the designed rocket motor

1.3.8. Validation of the results

After a close inspection of **Figures 1.3.14** through **1.3.17**, it is possible to conclude that the results in Table 1.5 are physically verifiable and valid because one can find corresponding points in the graphs at a given Mach value of 2.97 – the one obtained by calculating the exit velocity. The figure below depicts the area, pressure, density, and temperature ratios. The markers indicate the calculated nozzle ratios from the throat and the exit.

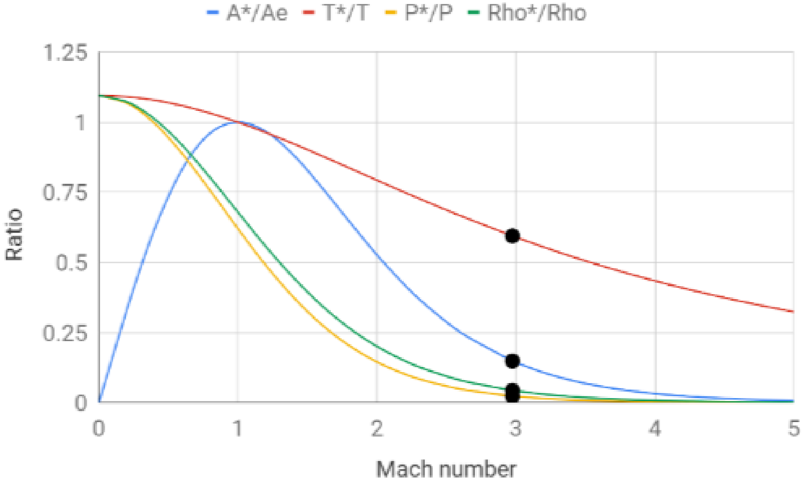

Fig. 1.3.18. Nozzle ratios with marked values for the proposed design

All in all, the results obtained by the one-dimensional isentropic flow model are beneficial in order to determine the resulting rocket characteristics from the prescribed design parameters. In this particular case, we are able to calculate values that were instrumental in confirming the simulation results. One can conclude that the nozzle produces supersonic flow after the throat, which produces sufficient thrust with shock forming almost at the nozzle exit for slightly suboptimal performance, but the given benefits provided by the conical nozzle shape – the ease of manufacturing the nozzle and the ability to use different types of propellant grains – outweigh the slight loss of performance.

1.3.9. 3D study

The simulation study by itself is based on mathematical calculations in the computational domain where computational cells are discrete entities which represent the fluid motion. For this particular research, the VoF (Volume of Fluid) method was used because Typical CFD methods which are based on Lagrange methods where mesh discretization is based on hexahedral cells had limitations whenever dynamic boundaries were introduced. This was caused by the relatively complex propellant grain whenever there was great possibility to generate high skewness cells, which led to singularities and negative values. Having said that, Eulerian based mesh methods were chosen as the best candidate to solve such a problem because it was possible to track the moving boundary continuously throughout the grid in the fraction-like manner.

Since the C-D nozzle is of the commonly applied geometry, it requires extremely precise modeling in order to optimize the smooth flow. Use of software which solves computational fluid dynamics to study supersonic and subsonic flows in the convergent-divergent nozzle will deliver a higher precision. The most important thing is that the nozzle should be able to perform as designed. Having said that, additional features where a numerical study is more advantageous than the analytical one offers a possibility to capture the sliver phase as precisely as possible. This is crucial for the motor optimization problems.

1.3.10. Internal ballistics of the solid rocket motors and their combustion stages

In the process of combustion of the propellant grain, thermal energy is transferred into kinetic energy which produces thrust. Internal ballistics in the start-up, steady-state and tail-off is the same. Internal ballistics relies on the combustion chamber temperature, the ratio of specific heats, the combustion chamber pressure, the mass flow rate, and other factors. All these parameters define thrust which the motor is producing during the combustion. In the paragraphs below, all the three phases of the combustion process will be presented in greater detail to showcase the influence towards the performance of the rocket motor and the possible offset from its design requirements [62].

The solid rocket motor is ignited by using initiation charge which is made from the propellant mixture with a fast burn rate and a high temperature. The igniter can be mounted on the bulkhead of the rocket motor or just simply placed into the combustion chamber at the bottom of the rocket through the throat of the nozzle. Such an approach eliminates the mass of the igniter after the ignition by simply leaving it on the launch pad, but, in most cases, the effect of this additional mass from the igniter is negligible with regard to the rocket’s performance [63].

During the start-up phase (when the motor starts to ignite), the pressure in the combustion chamber rapidly increases to the point where it creates a shock-like effect within the combustion chamber. In this phase, it is crucial that the mechanical properties of the propellant grain and motor casing could sustain the initial blast without creating cracks which can lead to the explosion of the rocket motor.

The steady-state phase is the main and the longest phase of the combustion process. In this mode, the rocket motor performs according to its grain characteristics. One must note that the calculated results can be slightly different from the experimental ones because combustion phenomena are a complex process with multiple constantly changing variables that can differ from the theoretical values.

Almost every solid propellant grain design produces sliver at the end of the steady-state phase. The thrust generated during the sliver phase is not sufficient enough to produce the required thrust-to-weight ratio for the vehicle to perform nominally. The sliver is all the remaining leftovers of the propellant after the steady-state phase has been completed. High amounts of sliver indicate inefficiencies of the propellant grain design or faults in fabrication. Commonly, the sliver phase is coupled with the tail-off phase when the propellant is about to be depleted, and the pressure in the combustion chamber starts to decrease towards the ambient pressure [64].

1.4. Introduction about the specific system used in the research

This particular research is focused on internal ballistics modeling of a specific system that we not only built and conducted experiments on but also deployed it in an actual rocket system. The aforementioned specific system is a rocket motor with a nominally designed thrust of 12000 – 10000 N that uses solid propellants; this is where the name RM-12K that is referred to throughout the dissertation stems from – “Rocket Motor” (RM) with the 12000N average thrust (12K). All the experimental data collected during static firing tests was obtained by using this rocket motor. We were able to use the collected data to validate the internal ballistics model created as a result of this research. Furthermore, as mentioned above, RM-12K is also used in the RT-400 aerial target system. The motor has been successfully deployed with RT-400 systems since 2014 and is still being used to this day (2019 as of writing). The military exercises were as follows:

1. “Amber Arrow 2014”, Klaipėda, Lithuania, Baltic Sea (from Vidar class staff and support ship *N42 Jotvingis*)
2. “Amber Arrow 2015”, Klaipėda, Lithuania, Baltic Sea (from Vidar class staff and support ship *N42 Jotvingis*)
3. “Amber Arrow 17”, Juodkrantė, Lithuania (From Juodkrantė training ground)
4. “Baltic Zenith 2018”, Šķēde, Latvia (from Šķēde military site)
5. “Baltic Zenith 2019”, Pape, Latvia (from Pape airfield).

The motor is highly practical, sometimes even at the expense of performance (as we shall discuss below), but, on the upside, its practicality, ease of fabrication and satisfactory characteristics made it a success worth investigating. That is another motivation for us to construct an internal ballistics model of this particular motor as we hope to optimize and improve the said motor to the extent that we want to fully understand it.

1.4.1. Rocket-propelled aerial target system – RT-400

RT-400 is a rocket with a solid propellant motor that is designed to mimic certain characteristics of live aerial targets for air defence applications. *RT-400* stands for Rocket Target which is 400 mm in diameter and is an abbreviation for the short-range aerial defence training system designed and developed by Kaunas University of Technology (KTU) *Institute of Defence Technologies, Department of Rocketry Applications* [65]. The RT-400 aerial target system is depicted in the picture below.

Fig. 1.4.1. RT-400 Aerial target system with RM-12K solid-propellant rocket motor

The system has been successfully deployed in short-range air defence training exercises as a cost-effective way to train operators in defending against aerial threats when using short-range guided anti-air defence systems such as STINGER [66], GROM [67] or RBS-70 [68].

1.4.2. Purpose of RT-400

The purpose of the RT-400 system is to substitute a fighter jet or an attack helicopter for short-range anti-aircraft defence training military exercises. The solid propellant rocket was chosen as a vehicle capable of achieving the aforementioned goal because of its relatively high velocity, cost-effectiveness, ease of use, and durability. These attributes are desired for the training purposes because they provide learning opportunities even for experienced anti-air systems operators. Conventional targets used for training are either stationary ground, sea objects or moving UAVs or drones. They are used for training operators to improve their lock-on and aiming abilities, but these types of exercises do not prepare for more realistic high-speed aerial target acquisition and termination scenarios. Both UAVs and drones lack realism as far as simulating the fighter jet behavior is concerned as they lack speed, can be costly, difficult to operate and are not always suited for harsh weather conditions/poor visibility situations. Meanwhile, a rocket-propelled target can be deployed in almost any weather conditions, with minimal operational overhead, and can be launched in different ballistic trajectories that can make the training more dynamic thus allowing for more realistic exercises.

1.4.3. Sub-systems and prescribed design parameters of RT-400

The RT-400 system consists of 4 key subsystems that allow it to be safely deployed and operated during military exercises as a standalone device or as embedded into or combined with other vessels.

The 4 key subsystems are as follows:

1. The mobile launch system which is a portable, reusable fire-resistant lightweight trailer with a built-in rocket launcher and safety mechanisms.
2. The launch sequence check and initiation hardware – this is an additional part of the rocket launcher responsible for the launch control.
3. The remote controller connected by wire to the launch control system allows for the safe and timely launch of RT-400 rockets.
4. The RT-400 rocket motor is a solid propellant powered rocket consisting of 7 core parts (**Fig. 1.3.1**).

Furthermore, the RT-400 system was designed by using several prescribed parameters. One of the key design requirements was the size of the rocket which had to feature a sufficient cross-section in order to be detected by various radar systems during training sessions. RT-400 had to be designed in such a way that it would be able to simulate various types of aircraft; therefore, multiple design parameters had to be met, such as velocity, flight height, range, rocket size, and flight time. The full list of various design and performance properties is presented below in Table 1.6.

Table 1.6. Properties of the RT-400 system

No.	Property	Value	No.	Property	Value
1.	Length of the target, l, m	5.2	9.	Rocket motor mass (with propellant), m_{mot}, kg	35
2.	Length of the rocket motor, l_1, m	1.06	10.	Rocket mass, m, kg	105
3.	The diameter of the target, d m	0.4	11.	Burn time of the rocket motor, t_{burn}, s	3.25
4.	The diameter of the target, d, m	0.16	12.	Maximum flight time of the rocket, t_{max}, s	44.92
5.	The nominal thrust of the rocket motor, T_{nom}, kN	10	13.	Maximum flight range, X_{max}, km	4.5
6.	The impulse of the rocket motor, I, kNs	32	14.	Maximum flight height, Y_{max}, km	2.2
7.	The specific impulse of the rocket motor, Isp, s	182	15.	The velocity range of the rocket, v, m/s	30 - 282
8.	Propellant mass, m_{prop}, kg	18	16.	Drag coefficient, cd, -	0.48

As the table shows, RT-400 is 5.2 meters in length, 0.4m in diameter with a nose shape that generates a drag coefficient of 0.48 that allows the rocket to stay in flight for the maximum of approximately 45 seconds and fly for 4.5km at a maximum height of 2.2 kilometers while reaching a top speed of 0.8 Mach.

The aforementioned performance metrics are sufficient to mimic a fighter jet or an attack helicopter passing by at a realistic speed and altitude in order for anti-air systems operators to gain valuable training experience by practicing with the RT-400 system.

1.4.4. RT-400 use in practice

The RT-400 short-range air defence training system has already been deployed in military exercises, during which, the system was embedded in a naval vessel and also used on land. The system has been successfully deployed during day and night-time exercises. Due to its relatively lightweight design, it can be operated by as few as 2 people, however, manning by 4 individuals is recommended due to the manual effort required in reloading the system with new RT-400 rockets after each launch. The reload of the system takes about 10–20 minutes, which involves only placing a new target onto the launcher as the launch angle is set automatically for the desired ballistic trajectory after the reload procedure has been completed.

During a standard exercise routine, once the RT-400 has been loaded, the launcher sets the angle to reach the desired mission parameters and is launched remotely. Once RT-400 is airborne, an anti-air system (STINGER, GROM, RBS-70) operator acquires the moving target and takes a shot. RT-400 is then destroyed on impact, and the system is reloaded to launch another target if required. The system has already proven its feasibility in military exercises because of the simplicity of design, safety, ease of use, and cost-effectiveness. The following discussion will elaborate on the research and data behind the RT-400 design parameters that mimic fighter jet or attack helicopter characteristics and enables it to be used reliably and safely for military training purposes.

1.5. Summary

In this section, the following concepts were introduced:

1. The design features of the solid propellant rocket motors, why this type of propulsion device is unique with regard to design and performance.
2. The solid propellant composition, performance, and comparison with other Ammonium Nitrate formulations.
3. Discussion about various propellant grain types and key features with regard to motor performance.
4. Discussion about various nozzle types and explanation of the criteria used when selecting a satisfactory nozzle for RM-12K. Its influence in the flow acceleration.
5. Solid rocket motor characteristics. Start-up, steady-state, sliver and tail-off phases.
6. Real-world implementation of the motor in the aerial target system.

2. MODELING OF THE SOLID PROPELLANT ROCKET MOTOR

2.1. Key factors and advantages of simulations in solid rocket motor internal ballistics research

Simulations for rocket propulsion applications are becoming increasingly more affordable for small-scale research and the private space industry. Increasingly more research is being performed by employing numerical methods for rocketry and space applications [69]. These developments have become available because of the relatively cheap and abundant computational resources which can be harnessed from computer clusters/clouds [70], local machines, or even low power computing clusters of various architectures [71]. For example, most of the research and development (R&D) prototypes at the private space exploration company *SpaceX* were developed by using simulations in the 'cloud' rather than by static testing. This approach saves labor and money, and, in turn, enables companies and researchers to expedite the iteration of propulsion system designs [72].

Despite the advantages of numerical method-based simulations, there are still persisting significant challenges that must be considered before employing this technique. The main issue of the classical analytical methods is the need for homogeneous (linear) models, which is not a realistic assumption in fluid dynamics and therefore does not represent the physics accurately. For this reason, numerical method-based computer simulations are an attractive option as they are capable of dealing with the chaotic nature of multiple, high energy reactions occurring simultaneously. However, simulations have inherent challenges that do not need to be considered in experimental approaches. One of the key challenges is the initialization of the solution, which requires the setting of all the environmental parameters semi-subjectively. This is important because the parameters must represent the domain in which the model has to operate, and, therefore, a slight divergence from reality may render the simulation results useless and impossible to reproduce in the field activity. Another key challenge is the determination of the numerical schemes. Unfortunately, there is no 'right' answer when it comes to choosing one, and thus the simulation results can vary on the case-by-case basis.

2.2. Model and methods of the solid rocket motor internal ballistics

The modeling approach was selected in order to reduce the need for experimental testing. Internal ballistics was modeled as a CFD (Computational Fluid Dynamics) problem.

Computational fluid dynamics (CFD) is the simulation of physical sciences that represents how fluids affect objects. Fluid dynamics uses Navier-Stokes equations [73]. These equations describe how the velocity, pressure, temperature, viscosity, concentration and other properties of the fluid are interlinked. CFD has become a valuable tool for analyzing energy properties and modeling the airflow. In this research, CFD is based on the *volume of fluid* method where the object is transformed from the geometrical type, Computer-Aided Design program (CAD) to the mesh type, which means that every element of the mesh is converted to a single cell which connects and shares information with the neighboring cells through the nodes. Computations are executed for each cell (by computing their centroids) separately by solving partial differential equations (PDE's) for every iteration with regard to the prescribed boundary and initial conditions. CFD has been around since the early twentieth century and has been mainly used for researching gas flow in aerospace, automotive, oil and gas as well as energy industries [74].

The aforementioned Navier-Stokes equations in fluid mechanics are partial differential equations that describe the flow of fluids. To be more specific, the equations describe how the velocity, pressure, temperature, and density of a moving fluid are related. The equation is a generalization of the equation devised by Swiss mathematician Leonhard Euler in the 18th century to describe the flow of incompressible and frictionless fluids [75]. The element of viscosity (friction) was introduced by French engineer Claude-Louis Navier in 1821 for the more realistic and far more difficult problem of viscous fluids. British physicist and mathematician Sir George Gabriel Stokes improved on this work throughout the mid-19th century, although, at that time, complete solutions were obtained for simple two-dimensional flows only.

The equations are a set of coupling differential equations and can be solved in theory by using calculus methods for a given flow problem. But, in practice, these equations are too difficult to solve analytically. Recently, modern computers have been used to solve approximations to the equations by using a variety of techniques, such as the finite difference, finite volume, finite element, volume of fluid and spectral methods. This area of study is called Computational Fluid Dynamics or CFD.

Navier-Stokes equations consist of a time-dependent continuity equation for the conservation of mass, three time-dependent conservation of momentum equations, and the time-dependent conservation of energy equation. There are four independent variables in the problem, the x, y, and z spatial coordinates of some domain, and time t. There are six dependent variables; pressure p, density ρ, and temperature T (which is contained in the energy equation through the total energy E_t), and three components of the velocity vector; the u component is in the x-direction, the v component is in the y-direction, and the w component is in the z-direction. All of the dependent variables are functions of all the four independent variables. The differential equations are therefore partial differential equations and not the ordinary differential equations. To indicate partial derivatives, the symbol 'partial' is used. The symbol indicates that all the independent variables must be fixed when computing a derivative, except for the variable next to the symbol.

To solve a flow problem, one has to solve all the five equations simultaneously; that is why it is called a coupled system of equations. There is actually a sixth – state – equation that is required to solve this system which relates the pressure, temperature, and density of the gas with the specified stress tensors. One of the main issues of solving the problem by the direct numeric solution (DNS) method is the enormous computational power requirements because of the Kolmogorov microscales theory [76] which states that the mesh size has to be as small as possible so that it would be able to capture the smallest eddies in the computational domain, which means that hundreds of millions or billions of cells are needed for accurate results to be implemented into the computational domain. This is why, approximations are used.

In CFD, the stress tensor terms are often approximated by a turbulence model which is a simplified version of the complex Navier-Stokes mathematical description because solving Navier-Stokes equations directly is inefficient (computationally) and time-consuming. In CFD terms, the solutions acquired by using turbulence modeling are called RANS (Reynolds-Averaged Navier-Stokes) or LES (Large Eddy Simulation).

RANS simulation is one of the most popular methods to deal with numerical problems [77]. This approach states that no computational domain is treated for direct numerical solution, and everything is solved by using approximations with accordance to the model in use. Such a method is used for practical applications on a daily basis for calculating turbulent flows. One must note that there is a wide variety of turbulence models since there is no one universal model to solve all the required problems by using CFD. For instance, one can use a specific turbulence model designed to solve flow separation, and another model to solve swirling flows (as an example). Furthermore, when combustion problems have to be solved as precisely as possible, the same turbulence phenomena can lead to unacceptable results. This is why it is strongly suggested to validate models by comparing the obtained results with experiments. All in all, the RANS method is based only on the modeling approach and involves more diffusive terms than any other described method which yields a more approximated result than LES or DNS, but it allows saving computational time and still achieves acceptable results.

LES simulation is a hybrid between RANS and DNS [78]. This means that the area of interest is solved by direct numerical solution, whereas other zones are solved by the RANS method. This method is more computationally expensive and more sensitive to the boundary and initial conditions, which, if set incorrectly, can exert pronounced adverse effects on simulations. On top of that, we must note that, in comparison with RANS, the mesh density has to be much more refined, which increases the computational time.

2.2.1. Conservation of mass

To solve the partial differential equations by using numerical methods for the specific problem, several assumptions must be taken into account, and also certain boundaries have to be introduced. The conservation of mass according to Navier-Stokes equations states that fluid dynamics and thermodynamic laws are based on physical continuities. The principle of continuity, or the equation of continuity, states that it is necessary for the fluid to move in such a way that the mass is preserved when the fluid is in motion. This principle is a consequence of the law of mass preservation. Hence, the conservation of mass (the mass continuity equation), Eq. (2.1), describes how mass is conserved in a closed system [79]. It is worth noting that the partial differential equation representing mass conservation in the fluid flow can be derived in a sense working backward to recover an integral form often referred to as the control-volume form.

$$V_f\,\frac{d\rho}{dt}+\frac{d}{dx}\left(\rho vA_y\right)+R\,\frac{d}{dy}\left(\rho\omega A_z\right)+\xi\,\frac{\rho uA_x}{x}= \\ =R_{DIF}+R_{SOR}, \tag{2.1}$$

where V_f is the fractional volume open to flow, ρ is the fluid density, R_{DIF} is the turbulent diffusion term, R_{SOR} is the mass source term, R is the reference frame indicator, and ξ is the geometry reference frame type indicator ($R \neq \xi$). The velocity components (u, v, w) are in the coordinate directions (r, R_{SOR}, z). A_x, A_y, and A_z are the area fractions for flow in the directions corresponding to the grid axis. In the cylindrical coordinate system, the y derivatives must be transformed into azimuthal derivatives. The conversion equation is given as follows:

$$\frac{d}{dy}\rightarrow\frac{1}{r}\frac{d}{d\theta}. \tag{2.2}$$

2.2.2. Fluid modeling

Momentum conservation is a fundamental law of physics that states that the momentum of a system is constant when there are no external forces acting on the system. It is embodied in the first law of Newton (the law of inertia). The momentum itself is defined as an object’s mass multiplied by the object’s velocity; the momentum is neither created nor destroyed, but only changed by the action of forces as described by the laws of motion. Momentum conservation is the trickiest to calculate compared to mass and energy because momentum is a number of vectors involving both magnitude and direction. Momentum is maintained simultaneously in all the three physical directions. Calculations are even trickier for gaseous domains because forces in one direction can affect the momentum in another direction due to collisions among molecules.

The equations of motion for the fluid velocity components (u, v, w) in the three coordinate directions are given by the Navier-Stokes equations with additional terms capable of handling the specific problem represented in Eq. (2.3). Hence, the velocity magnitude can be derived by the relation $\mathrm{U}=\sqrt{u^2+v^2+w^2}$. In this study, the velocity is measured in SI units [80].

$$\begin{aligned}
&\frac{du}{dt}+\frac{1}{V_F}\left\{uA_x\frac{du}{dx}+vA_yR\frac{du}{dy}+wA\ \frac{du}{dz}\right\}-\xi\frac{A_yv^2}{xV_F}=\\
&-\frac{1}{\rho}\frac{dp}{dx}+G_x+f_x-b_x-\frac{R_{SOR}}{\rho V_F}\left(u-u_w-\delta u_s\right)\frac{dv}{dt}+\\
&\frac{1}{V_F}\left\{uA_x\frac{dv}{dx}+vA_yR\frac{dv}{dy}+wA_z\frac{dv}{dz}\right\}+\xi\frac{A_yuv}{xV_F}=\\
&-\frac{1}{\rho}\left(R\frac{dp}{dy}\right)+G_y+f_y-b_y-\frac{R_{SOR}}{\rho V_F}\left(v-v_w-\delta v_s\right)\\
&\frac{dw}{dt}+\frac{1}{V_F}\left\{uA_x\frac{dw}{dx}+vA_yR\frac{dw}{dy}+wA_z\frac{dw}{dz}\right\}=\\
&-\frac{1}{\rho}\frac{dp}{dz}+G_z+f_z-b_z-\frac{R_{SOR}}{\rho V_F}\left(w-w_w-\delta w_s\right)
\end{aligned}\tag{2.3}$$

Here, (G_x, G_y, G_z) are the body accelerations, (f_x, f_y, f_z) are the vicious accelerations, (b_x, b_y, b_z) are the introduced masses at the source represented by geometric components, (u_w, v_w, w_w) represents the velocity of the source component, and (u_s, v_s, w_s) is the velocity component of the fluid at the surface of the source relative to the source itself. The derivation of this source term is given by:

$$U_s=\frac{dQ}{\rho QdA}n,\tag{2.4}$$

where dQ is the mass flow rate, ρ_Q is the fluid source density, dA is the area of the source surface in the cell, and n is the outward normal to the surface. In this case, n = 0.0 because the flow is a stagnant pressure type. This means that the source term which introduces fluid into the domain has a zero-velocity magnitude at the interface of the propellant surface. As a result, pressure must build up at the source so that to move the fluid away from the source. This helps to model the emerging fluid from the propellant grain and to mimic the grain burning process when the emerging fluid creates momentum inside the source component.

2.2.3. Energy transfer

Energy conservation is a fundamental concept of physics along with mass conservation and momentum conservation. In physics, the energy conservation law states that an isolated system’s total energy remains fixed within the domain, it is also believed that it will be preserved over time. This law means that energy cannot be created or destroyed but can only be transformed or transferred from one form to another (potential energy can be converted into kinetic energy). For example, when a propellant grain starts to combust, chemical (thermal) energy is converted to kinetic energy. If one adds all the energy forms released in the combustion, specifically, kinetic energy, as well as the heat and other energy-related factors, one gets the exact decrease in the propellant’s combustion of chemical energy.

Fluid energy equations Eq. (2.5) are required to calculate the heat transfer of the fluid. The fluid temperature affects the fluid flow properties during the transition from the combustion chamber through the throat of the nozzle before escaping the choked flow into the diverging part of the nozzle when leaving the domain.

$$\begin{gathered} V_F \frac{d}{dt}(\rho I) + \frac{d}{dx}(\rho I u A_x) + R\frac{d}{dy}(\rho I v A_y) + \xi\frac{\rho I u A_x}{x} = \\ -p\left\{\frac{duA_x}{dx} + R\frac{dvA_y}{dy} + \frac{dwA_z}{dz} + \xi\frac{uA_x}{dx}\right\} + RI_{DIF} + \\ T_{DIF} + RI_{SOR}, \end{gathered} \tag{2.5}$$

Here, I is the macroscopic mixture of internal energy where the subscripts DIF and SOR refer to the diffusion and source terms, respectively. As the model employs a two-fluid problem, ρI is given by Eq. (2.6)

$$\rho I = F\rho_1 I_1 + (1-F)\rho_2 I_2 . \tag{2.6}$$

The heat conduction diffusion process is introduced in Eq. (2.7).

$$\begin{gathered} T_{DIF} = \frac{d}{dx}\left(kA_x \frac{dT}{dx}\right) + R\frac{d}{dy}\left(kA_y R\frac{dT}{dy}\right) + \\ \frac{d}{dz}\left(kA\ \frac{dT}{dz}\right) + \xi\frac{kA_x T}{x} \end{gathered} \tag{2.7}$$

Here, k is thermal conductivity. For this model, each fluid is locally weighted by the fluid volume fraction, F.

2.2.4. Interface modeling

According to the equations described above, one key feature has to be introduced for us to be able to simulate the evolution of the burning surface of the propellant grain. The main problem of the CFD models is that the majority of fluid flow problems are simulated by using static mesh methods. Such models offer the opportunity to solve steady-state or transient fluid flow problems around obstacles or cavities, which allows for the researcher to understand the problem in a greater detail only for specific cases when the solid domain is immobilized. Such simulations are widely used in the aerospace industry for the external flow simulations around aerofoils or vehicle shells. In another case, most of the real-world problems are based on dynamic behavior when the same aerofoils change, for example, the angle of attack. For such problems, dynamic mesh or moving reference frame methods can be introduced into simulation. Having said that, there are still limitations if one needs to solve more complex simulations which require complex solid domain movements or even a change of shape. For this type of research, the simulation must involve the ability to track the mesh changes at the cell level and apply fluid-structure interaction to the computational domain. By default, such a type of simulations is computationally expensive and hard to set up. One of the key factors to allow this kind of simulation is the introduction of the interface region between the solid and fluid domains where the numerical code could enable us to recalculate the changes of the solid domain. To model the burning surface of the solid propellant, the fluid interface in the computational cell between the fluid and solid domains must be introduced. Such phenomena can be defined in terms of the volume of the fluid function, F (x, y, z, t) [81]. This function represents the volume of fluid per unit volume and is given by Eq. (2.8). This interface moves during the simulation, and its parameters are derived by Eq. (2.7).

$$\frac{dF}{dt}+\frac{1}{V_F}\left[\begin{array}{l}\frac{d}{dx}\left(FA_x u\right)+R\frac{d}{dy}\left(FA_y v\right)+\\ \frac{d}{dz}\left(FA_z w\right)+\xi\frac{FA_x u}{x}\end{array}\right]=F_{DIF}+F_{SOR}, \tag{2.8}$$

where

$$F_{DIF}=\frac{1}{V_F}\left\{\begin{array}{l}\frac{d}{dx}\left(v_F A_x\frac{dF}{dx}\right)+R\frac{d}{dy}\left(v_F A_y R\frac{dF}{dy}\right)+\\ \frac{d}{dz}\left(v_F A_z\frac{dF}{dz}\right)+\xi\frac{v_F A_x F}{x}\end{array}\right\}. \tag{2.9}$$

Here, the diffusion coefficient is defined as $v_F=\frac{c_F\mu}{\rho}$, where c_F is a constant whose reciprocal is sometimes referred to as the turbulent Schmidt number, and F_{SOR} is the density source (corresponding to R_{SOR} in Eq. (2.1)). For a compressible two-fluid simulation, F represents the volume fraction of fluid, and the density is calculated from the compressible fluid equation-of-state.

2.2.5. Numerical schemes

Second-order schemes were used for the approximation of the model equations. First-order schemes were used only to check the model's integrity and stability for the initial stages of the research. Final simulations were conducted by using only second-order, monotonicity-preserving upwind-difference method-based schemes. These schemes require greater computational resources but are far more precise in comparison to the first-order schemes because an additional derivative is being solved. The monotonicity-preserving method was applied to the approximate momentum, density, energy, and fluid fraction advection. The used discretization scheme is derived by using second-order polynomial approximations to the advected quantity in each of the coordinate directions [82]. In Eq. (2.10), one can see how variable Q advected in the x-direction, the value fluxed through the cell-face Q^* is computed.

$$Q^*=Q_i+\frac{1}{2}A\left(1-C\right)\delta x_i, \tag{2.10}$$

Where: Q_i – cell-centered value, C – Courant number, x_i – cell size, A – second-order approximation to the first derivative of Q at the location which Eq. (2.11) describes within the cell.

$$x_0=\frac{1}{6}\left(1-2C\right)\delta x_i. \tag{2.11}$$

Coefficient A can be calculated from two neighboring first derivatives by linear interpolation provided that these derivatives are second-order accurate. The latter can be achieved by computing the derivatives at the midpoint between the Q_i locations as described in Eq. (2.12) below.

$$\frac{dQ}{dx_{i+\frac{1}{2}}} = 2\frac{Q_{i+1} - Q_i}{\delta x_{i+1} + \delta x_i}, \tag{2.12}$$

This equation is a second-order accurate first derivative for Q at the point between Q_i and Q_{i+1}. In order to ensure monotonicity, it is necessary to restrict the value of derivative A [83]. The value of A is not allowed to exceed twice the minimum magnitude of the centered Q derivatives used in its computation by Eq. (2.13).

$$A \le 2\left(\frac{dQ}{dx_i}, \frac{dQ}{dx_{i+1}}\right). \tag{2.13}$$

For momentum advection, second-order approximation allows achieving stable convergence even for an unstable, swirling flow. The introduction of the same second-order schemes to density and heat transfer equations allows avoiding first-order schemes problems, such as numerical diffusion.

2.2.6. Combustion modeling

Combustion simulations are the most computationally expensive problems in CFD. Since combustion is such a rapid process, chemical reactions occur on the scale of nanoseconds [84]. This means that, for the transient simulation, the time step size has to be small enough, which in total can add up to millions of time steps for the relatively short physical time of the simulating process.

The simulation was executed without the coupling of the direct chemical kinetics modeling. All of the required values for the material properties and coefficients were obtained from a separate investigation. The combustion rate and energy production equations are given by Eqs. (2.14, 2.15), respectively [85].

$$Q_M = \rho_{solid}\left(aP^b\right) \tag{2.14}$$

Here, Q_M is the combustion gas mass flow rate in kg/s at the gas/propellant boundary, ρ_{solid} is the density of the propellant in kg/m^3, P is the pressure of the gas at the solid/gas interface, a is the burning coefficient (an empirical parameter), and b is the burning exponent (an empirical parameter).

$$Q_E = Q_M C_P T_{burn} \tag{2.15}$$

Here, Q_E is the energy produced by the reaction in Joules, Q_M is the combustion flow rate in m/s, C_P is the specific heat of the gas at constant pressure, and T_{burn} is the propellant burning temperature obtained from the chemical kinetics calculations.

When using this model, some limitations must be introduced:

1. No additional source terms are introduced into the momentum equations because combustion is assumed to be of the stagnation type.
2. Combustion gas density is calculated from the ideal gas equation.
3. Direct turbulence effects on the burn rate are ignored.
4. Stress and deformation calculations for the propellant grain are ignored.

The model combustion component is described by a stationary component but changes shape and volume according to the evolution of time. These changes are constrained by the initial conditions of the combustion component properties and the initial shape of the propellant grain. The combustion component area and volume fractions are computed at the single-cell level for every time step during the simulations until the combustion component has been depleted in the computational domain. The primary variable that represents the geometry component is the relative (fractional) volume of the solid in a cell, which is the ratio of the solid volume in the cell to the total cell volume. This relationship is described by Eq. (2.16) [86].

$$V_{f,combust} = \frac{V_{combust}}{V_{cell}}, 0 \le V_{f,combust} \le 1 . \tag{2.16}$$

The open volume fraction in a cell, or the volume fraction, can then be described in the form of Eq. (2.17).

$$V_f = 1 - V_{f,combust} . \tag{2.17}$$

The equation for the change in the solid propellant content in the computational cell can be written in the form of Eq. (2.18), where the open area of the burning surface of the solid propellant of the cell is dA.

$$\frac{dV_{f,combust}}{dt} = \frac{Q_M \, dA}{\rho_{solid} V_{cell}} . \tag{2.18}$$

Fig. 2.2.1 illustrates the interface region used in computation for the combustible element, where the control volume is the computational domain mesh element (cell), fractional parts of the solid propellant (V_{solid}) and fluid domain fraction (gas).

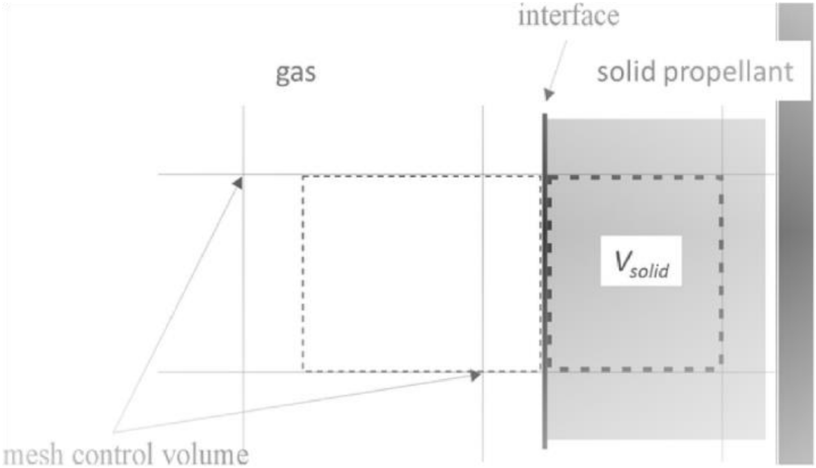

Fig. 2.2.1. Schematics of the interface region in the numerical model [92]

This model provides the amount of propellant burned in each time step, and is described by Eq. (2.19).

$$\frac{dM}{dt} = Q_M \frac{dA}{dt} . \tag{2.19}$$

The energy produced by the combustion process is distributed over the gas volume at the burning surface interface. After introducing the processes described above, the diffusion and convection processes are calculated, and the mass transport equation is solved for the gas produced by the reaction. This equation can be described by the mass source relation for the combustion chamber pressure:

$$\frac{dm}{dt} = aP^b. \tag{2.20}$$

2.3. Construction of an internal ballistics model of a rocket motor

The main objectives of the model were the ability to successfully implement calculation of the pressure, temperature, and velocity field values of the fluid flow with regard to the hexahedral mesh which was used in the simulation for the RM-12K rocket motor which is employed in the RT-400 aerial target system.

The model for the study has to abide by the following constraints and assumptions:

1. The material properties for the initial fluid (air) have to be implemented.
2. The material properties for the propellant have to be implemented.
3. The material properties for the propellant combustion products have to be implemented.
4. All the required numerical models for the fluid flow calculations have to be implemented.
5. The numerical models for interface tracking and dynamic mesh calculations have to be implemented.
6. The mesh in the cylindrical reference frame capable of efficiently capturing geometry features of the rocket motor have to be generated.
7. The mass flow objects with specific boundary conditions for the ignition implementation of the grain have to be created.
8. The boundary conditions for the computational domain have to be constrained so that the flow would be physical.
9. Physical initial conditions for the simulation have to be applied.
10. The required numerical schemes for gradients, divergence, discretization, and other factors have to be applied according to the required stability and diffusion parameters of the used models.
11. The adaptive time-stepping allowing to save computational time with regard to varying simulation phases have to be implemented
12. The sensor (probing) points and sampling surfaces in the areas of interest have to be created to track the specific parameters during the combustion process.
13. A strategy for the recording of the results has to be applied.
14. The simulation criteria with regard to the residual threshold values have to be constrained.
15. The simulation with regard to the physical time duration has to be constrained.

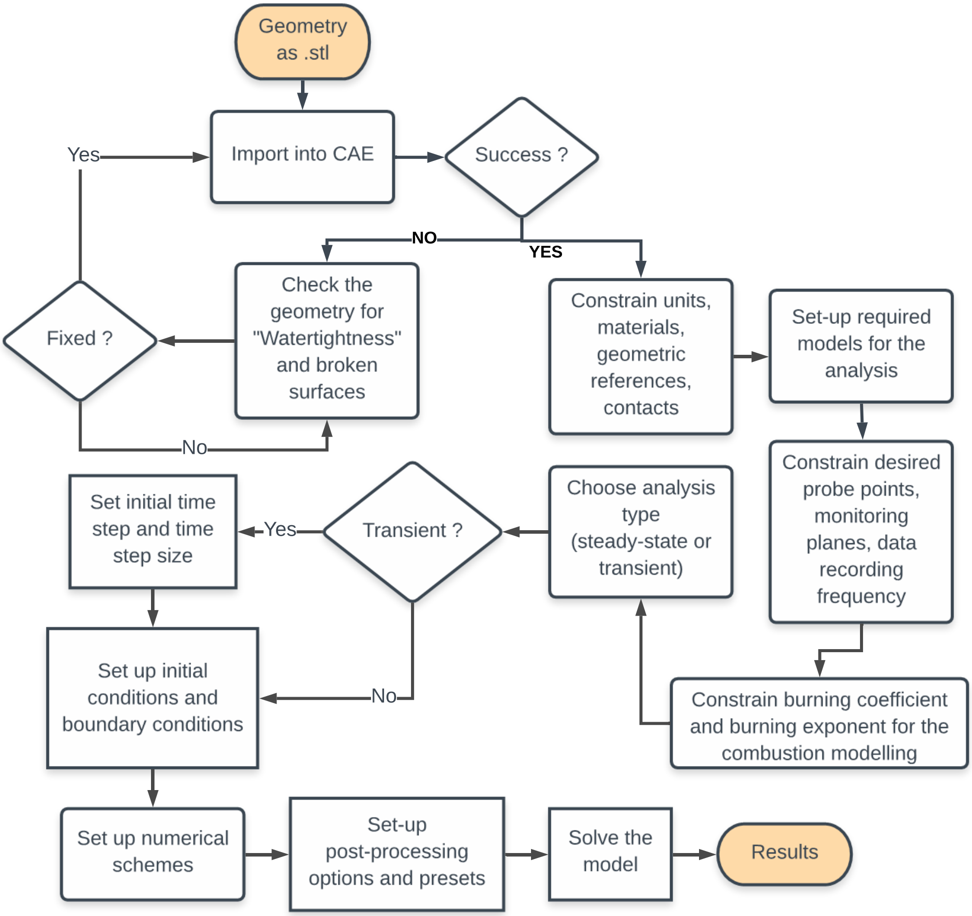

Fig. 2.3.1. Visual representation of the numerical algorithm

In order to set up a specific simulation with a dynamically changing mesh, some trade-offs had to be made, mainly because of the fact that the mesh has to be with interface tracking (**Fig. 2.3.2**) coupled with propellant grain combustion rate calculations, and, on top of that, it has to be sufficient enough with regard to the numerical stability and computational time. The first part of the modeling is dedicated to the propellant grain setup. The properties and composition of the motor had to be tailored and fine-tuned in order to achieve the desired motor characteristics.

A commercial code *Flow 3D* was used in order to create the aforementioned model. The model calculations were primarily based on the Volume of the fluid (VoF) numerical method, and the mesh calculations were based on Fractional Area Volume Obstacle Representation (F.A.V.O.R.) which was instrumental in calculating the solid state propellant and other combustion products' interactions with each other within the mesh. In the diagram above, we can observe a visual representation of the algorithm which is used within the commercial code to perform the calculations (**Fig. 2.3.1**).

Fig. 2.3.2. Evolution of the propellant grain due to interface tracking [87]

The RM-12K rocket motor uses a solid rocket propellant with a specific grain geometry which controls its combustion properties. One of the most prominent challenges while constraining a mesh for the propellant grain is to effectively capture the geometrical features of certain, more sophisticated parts of the said grain as the flow in those areas is more intense and requires extra attention. Having said that, it is relatively straightforward to solve this problem by increasing the mesh cell count, but such a strategy directly positively influences the time required for the computation to such an extent that, in some cases, it can take years for the simulation to complete. The best detail-to-simulation duration ratio was achieved by using the trial-and-error method. The resulting mesh was sophisticated enough to be able to represent a star grain neutral type thrust profile without introducing an unacceptable amount of errors.

The motor grain geometry was selected to be the neutral star type with an ammonium nitrate composite-based propellant (ANCP) forming the grain. This helps to sustain relatively the same level of thrust (the neutral thrust profile) during the steady-state of the combustion process. Moreover, the propellant was designed specifically for this motor by using the six main components. These components were divided into 3 groups: 1 – oxidizer, 2 – fuel, 3 – binder. For the oxidizer group, Ammonium Nitrate (AN) was used in the composition of the propellant which is a chemically stable component. It would not self-ignite and is safe to store in small or big batches. One element was used for the fuel group; it was aluminum. Aluminum itself was used in the form of a powder which was ball-milled to particles of 80 micrometers on average. Furthermore, four elements were used for the binder. The main portion of the binder consisted of silicone. It is worth mentioning that silicone can be divided into its composition, but, for the simulation, we can use the chemical composition provided from the datasheet of the manufacturer. In addition to silicone, three other components at small fractions were added into the mixture. The main purpose of these components is to act as stabilizers or enchanters of the specific properties of the propellant. Carbon acts as a temperature enhancer during the combustion. It helps to sustain the desired combustion temperature and enable a smooth combustion process while minimizing the oscillations of the combustion reaction. Iron oxide acts as a stabilizer as well, but also as a catalyst with regard to the burn rate and chemical reactions. Ammonium perchlorate acts similarly to ammonium nitrate, but its energetic properties are higher than AN. The main feature of this component in the mixture is to sustain and/or boost small fractions of the propellant where the mixture is slightly off the homogenous composition. The chemical composition and other physical properties of the propellant are shown in Table 2.1.

Table 2.1. Molecular composition and physical properties of the propellant components

Material	Weight, g	Density, g/cm^3	Composition
Ammonium Nitrate	55	0.06230	4H-2N-3O
Potassium Perchlorate	8	0.09100	1K-1Cl-O4
Aluminum	14	0.9760	1Al
Carbon	2	0.06370	1C
Silicone	20	0.03610	6H-2C-1O-Si
Iron Oxide	1	0.184	3O-2Fe

By combining all of the ingredients required for the ANCP propellant, it was found that the density of the propellant was 1623.4 kg/m^3. In order to obtain the chemical kinetic properties for the propellant, a separate analytical study was performed by using 100 g of the propellant. To obtain the required results, we need to dismantle the ingredients described above to the atom level. The composite propellant consists of a number of gram atoms of each element presented in the ingredients (in the ascending order): 1 – 0.012523 Fe, 2 – 0.057738 Cl, 3 – 0.057738 K, 4 – 0.269687 Si, 5 – 0.518903 Al, 6 – 0.705888 C, 7 – 1.374175 N, 8 – 2.580678 O, 9 – 4.366474 H.

Having said that, the chemical kinetics study revealed the results for the 2 areas of interest. The crucial one is based on the combustion chamber, whereas the second one is based on the nozzle level. One of the main parameters needed for the simulation to be implemented was the combustion temperature which, in this case, was 2322 K, and the γ value was 1.19. We must note that the gamma value in the numerical code was described as specific heat capacity when the volume is constant and as specific heat capacity when the pressure is constant. The chemical kinetics properties are shown in Table 2.2.

Table 2.2. Chamber results and exhaust results of the chemical kinetic model

	T, K	P, bar	Enthalpy, J	Entropy, J/K	C_p/C_v (γ)	RT, J/(kg·K)
Chamber results	2322	62.03	-103.52	224	1.16	3.66
Exhaust results	1526	0.962	-167.02	224	1.19	3.63

Here, T is the temperature in Kelvins, P is the pressure in bars (1 bar = 100000 Pa), C_P/C_V is the specific heat ratio (γ), and RT is the specific gas constant. From the simulation, the molecular weight of the mixture was 23.896 mol/g, and the gas specific heat was 2102 J/kg/K. The performance calculations showed that the specific impulse of the designed ANCP propellant was 235 s.

The Propellant Evaluation Program (PEP) software was used to obtain the chemical kinetics data. The software itself was developed for designing and analyzing the composition and performance of propellants [88]. To avoid numerical complexities, the igniter and ignition period was excluded here. The ignition process was simulated with constant conditions for the temperature and density of the jet gas escaping from five jets, which mimicked the igniter jet holes. The design process of the RM-12K involved custom tailoring of the properties and composition of the propellant grain and its shape. The motor model was designed by using CAD software and exported as stereographic (STL) format models for future pre-processing.

2.3.1. Justification of modeling parameter values and determination of computer resource requirements

The following assumptions and constraints are used for the numerical method-based computer simulation. The simulation was executed by using an 8-core workstation-grade machine with an *Intel i7-6700K* class processor with an 8 MB cache and a 4.2GHz clock speed, 48 GB of RAM memory, and 2 TB of the storage space. All other workstation components, such as I/O ports or GPU properties, were irrelevant for this type of study and shall not be discussed further in this thesis. The simulation type was set to transient, and the physical end time was set to 5 seconds. This was performed with an additional adaptive time step term. This approach allowed the capturing of the entire combustion process until the propellant had been completely depleted. Moreover, a coarsened time step was chosen to expedite the simulation because of the time required to calculate the changing computational domain interface which limits the simulation progress. On top of that, the initial time step was set to 245 ns. This value was chosen from the results of the previous simulations, which was the most time-saving time step in order to provide stable convergence and the time savings of the initial phase of the simulation. Furthermore, the minimum and maximum time step sizes were set to 1 ns and 0.1 s, respectively. The maximum time step was chosen to capture the final moments of the simulation when the combustion process was already over. The time adaptation was tracked with regard of time continuity. The total computation time for one simulation, comprising 170 million iterations, was approximately 2571000 s.

In conclusion, the assumptions and constraints of the simulation were designed to optimize the time taken to complete the simulation while maintaining an acceptable result accuracy. As a result, the simulation required 715 h of computing time on average when using an 8-core machine. Even though, from the first glance, it seems that finishing the simulation takes an enormous amount of time, it is still a relevant option because we can save a decent amount of labor and time in terms of obtaining the same results when applying the experimental approach which can take 3 months or more during the standard schedule while maintaining all the safety procedures for the RM-12K solid-propellant rocket motor test agenda.

2.3.2. Geometry and mesh of the model

The imported geometry and computational mesh setup had the following properties. The model was cylindrical and axisymmetric; it was meshed with structured hexahedral cells in a cylindrical reference frame. Moreover, the computational domain height and diameter were 1.12 m and 0.2 m, respectively, with a computational cell count of 162000. As described in the previous section, such a cell count of the mesh was obtained when applying the trial-and-error approach in an effort to obtain the minimum possible number of computational cells without losing the main geometrical features of the propellant grain. For post-processing purposes, two cutting planes were used to represent the simulation results. The first cut was made across the center axis of the motor thus providing representation and visualization of the combustion process inside the rocket motor. A second cut was made perpendicularly to the first cut in order to extract the cross-sectional view of the rocket motor. Both cutting plane locations are illustrated in **Fig. 2.3.14**. Furthermore, two probes were created and strategically positioned to allow the simulation to capture and record the specific data values. One probe point was constrained to the same position as the pressure probe in the real-life experiment that had been completed prior to the simulation. This probe was labeled Probe 1 and placed near the head section of the rocket motor. A second probe was placed at the very end of the exit of the nozzle and was labeled Probe 2. The setup was designed to effectively capture and monitor the simulation data for the purpose of comparison with the results obtained by previously performed static tests. One must note that, during static testing, the measurement hardware used in these tests was unable to perform the data acquisition at the nozzle section because combustion products leaving the nozzle would have incinerated the probe almost instantly.

2.3.3. Boundary and initial conditions

The initial conditions for the simulation were constrained to the fluid domain with 300 K initial air temperature inside the combustion chamber and 1.01 bar (101325 Pa) uniform atmospheric pressure. Such a configuration was chosen to mimic the initial conditions as they were during the static testing of the experimental rocket motor. We must note that static testing was conducted in the summertime, in July, on a sunny and hot day, when the ambient air temperature was around 298 K – 300 K. Moreover, the mass momentum source element was created to represent the propellant igniter. This artificial source had to mimic the real ignition process, and, therefore, the same combustion gas properties were used as those of the actual propellant. One must note that the chemical composition of the igniter for the real rocket motor was different from the chemical composition of the propellant grain. As a result, the gas composition of the combustion products was different, but, in order to minimize the computational duration, the same material was used for simulation purposes. What is more, the change of material was made due to the relatively insignificant role of the igniter with regard to the entire combustion process; therefore, such a simplification is unlikely to distort the results of the simulation. Furthermore, the temperature, the flow rate, and the gas density were 1200 K, 0.02 kg/s, and 10 kg/m^3, respectively. The igniter/mass source surface diameter was 0.01 m. There were five surfaces in total. One of the mass sources was placed perpendicularly to the domain axis, whereas the other four were positioned in a cylindrical pattern around the domain axis, being equally spaced at 45° angles. Finally, the igniter was placed near Probe 1 location with 0.4 s ignition time. The initial conditions were chosen to accurately represent the experimental environment. In the image below (**Fig. 2.3.3**), we can see the igniter's components before the assembly.

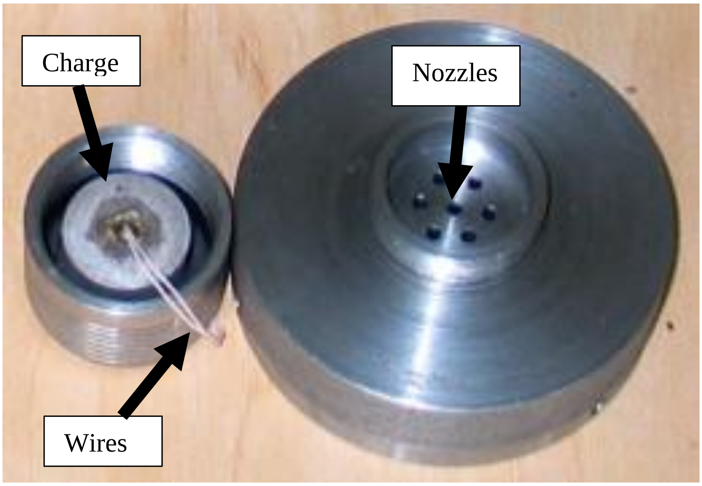

Fig. 2.3.3. Image of the igniter

The boundary conditions are extremely significant with regard to obtaining the desired simulation results. The boundary conditions for the cylindrical domain were constrained with the same symmetry for all the boundaries except for the periodic boundaries in contact with each other, which is necessary for cylindrical meshes when the full domain is simulated. Furthermore, in order to achieve stable convergence, the boundary at the end of the nozzle was constrained as a pressure outlet. We must note that the interface region for the fluid and solid acts as the dynamic boundary condition. To conclude, this relatively simple set of boundary conditions is all that is required to obtain the physical results.

2.3.4. Assumptions with regard to a specific numerical code

Some key assumptions had to be considered for the specific numerical code. The discussion below describes these assumptions and the reasoning behind them.

Two computational domains, solid and fluid, were constrained with different additional properties for different geometric parts which were as follows:

Table 2.3. Properties of the parts used in the simulation

Part	Type	Properties	Description
Head	Solid	Steel 304, Rigid, bonded with casing	1
Casing	Solid	Aluminum 7075-T6, rigid, bonded with head, tail, nozzle	2
Tail	Solid	Steel 304, rigid. Bonded with nozzle and casing	3
Nozzle	Solid	Graphite, tanso, bonded with tail and casing	4
Propellant	Combustible	ANCP, in contact with the head, casing, nozzle	5

Contacts between parts were constrained as bonded to simplify the simulation because the study was based on an internal ballistics research, and the contact study can be done after this study by implementing the acquired pressure values to the combustion chamber. As described in Table 2.3 above, the description column is numbered according to the list as follows:

1. The head part was imported as simplified geometry; it was used for the production of the real part. It was done to simplify the model and minimize the geometry features which could increase the cell count dramatically. The igniter geometric feature was excluded as well because this feature was implemented from the numerical code properties as a virtual component. In the picture below, we can see the head part prepared for numerical analysis after simplification and the head part as it should be made for the production of the real rocket motor for static testing (**Figs. 2.3.4** and **2.3.5**).

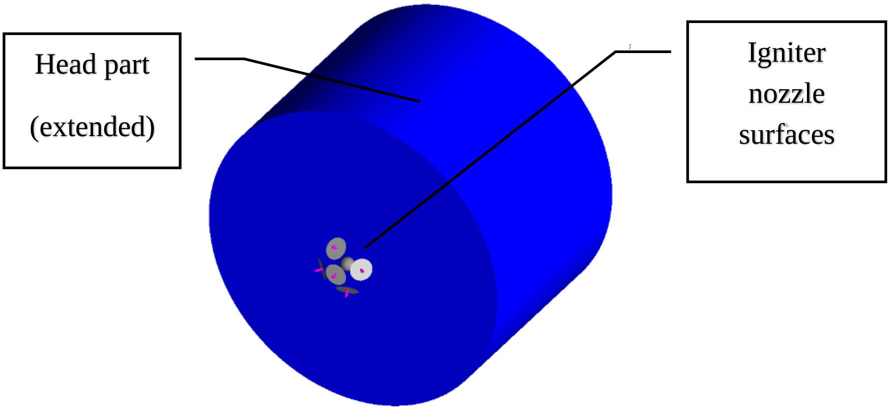

Fig. 2.3.4. Simplified head part for analysis. Refer to Fig. 2.3.14 item 1

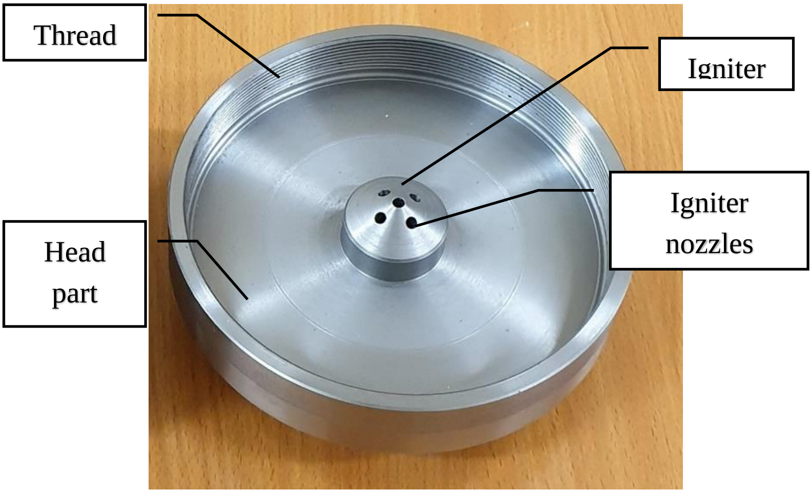

Fig. 2.3.5. Production sample of the head part. Refer to Fig. 3.2 item 7

2. The casing part was modified for the simulation in order to minimize the cell count in the domain. The thickness of the casing was expanded in order to allow the use of bigger mesh cells. This was done because the casing had to

create the boundary for the propellant only, and in all other phases of the simulation it was excluded and acted only as a placeholder for the propellant grain. In the pictures below, one can see the production part of the casing and its simplified version for the simulation (**Figs. 2.3.6** and **2.3.7**).

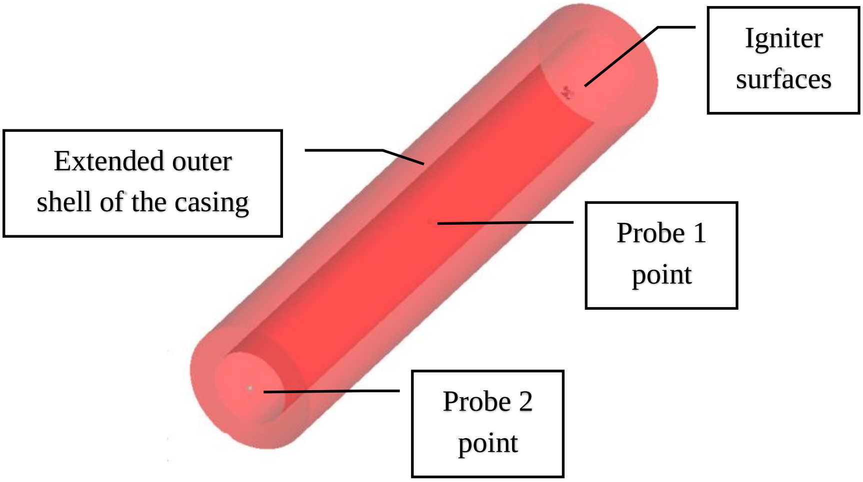

Fig. 2.3.6. Simplified casing part for analysis. Refer to Fig. 2.3.14 item 2

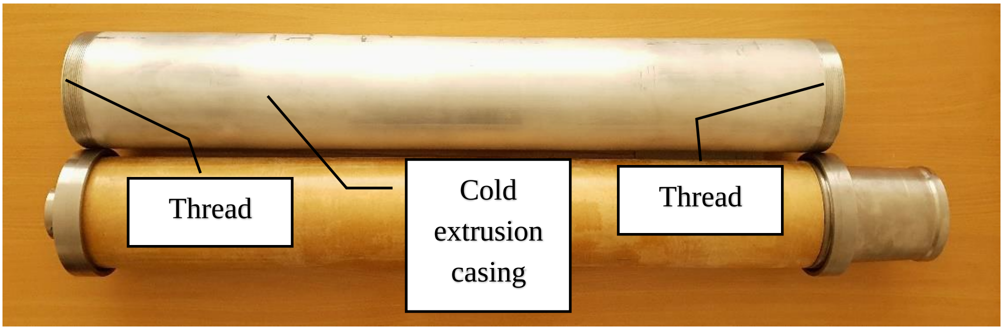

Fig. 2.3.7. Casing part for production. Refer to Fig. 3.2 item 6

3. The tail part (sometimes referred to as the *skirt*) was originally designed to couple the casing of the rocket motor and to hold the nozzle together. The simplified version of the tail was made where the interfering faces between the casing and the skirt were bonded to form rigid assembly for the simulation. In the pictures below, we can see the tail part model prepared for production as well as the simplified version which was used in the simulation (**Figs. 2.3.8** and **2.3.9**).

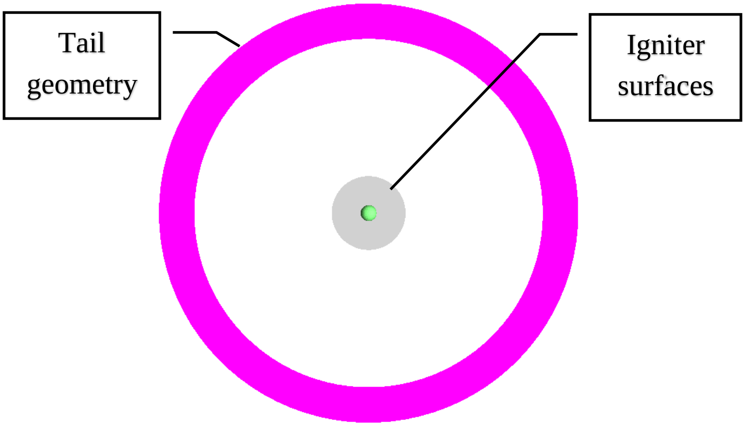

Fig. 2.3.8. Simplified tail part used in simulation. Refer to Fig. 2.3.14 item 3

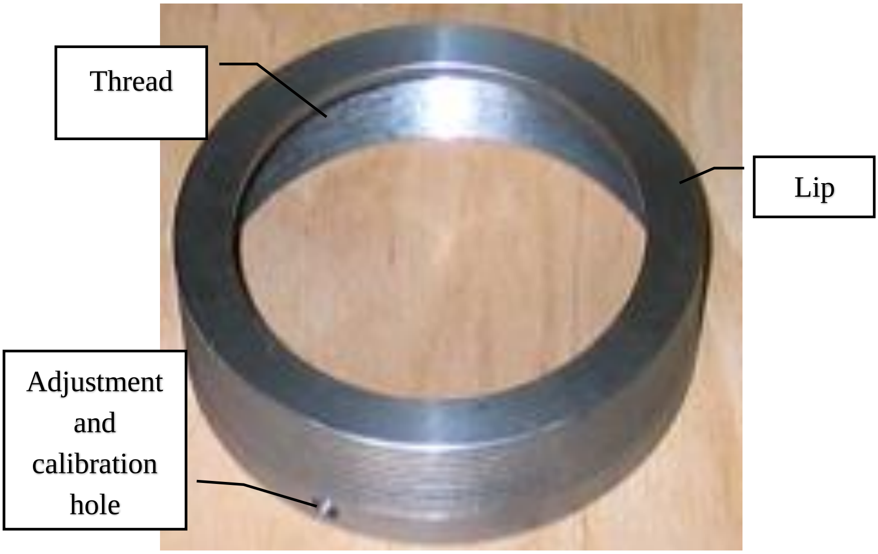

Fig. 2.3.9. Tail part geometry made for production. Refer to Fig. 3.2 item 6

4. The nozzle, one of the main objects in the simulation with regard to obtaining the desired simulation results, was the same as it was in the production blueprints. This was done in order to eliminate every possible deviation from the real rocket motor due to possible future problems when the comparison and evaluation of the model will be needed. In the picture below, we can see the original part of the nozzle which was manufactured for the production as well as the part which was used in the simulation (**Figs. 2.3.10** and **2.3.11**).

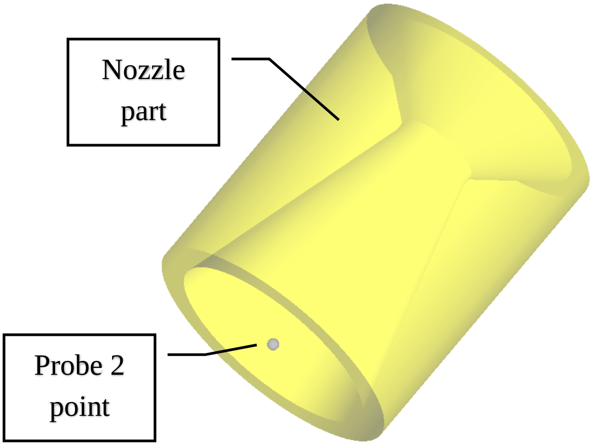

Fig. 2.3.10. Nozzle part which was used in simulation. Refer to Fig. 3.2.14 item 3

Fig. 2.3.11. Nozzle part which was made for production. Refer to Fig. 3.2 item 3

5. The ANCP propellant part as the star type grain geometry was imported as identical geometry as it was used in the real rocket motor. With regard to simulation, there was almost no simplification in order to ensure the same thrust curve profile as it was acquired from the static testing. In the pictures below, we can see the produced propellant grain which was used in the rocket motor as well as the geometry used in the simulation (**Figs. 2.3.12** and **2.3.13**).

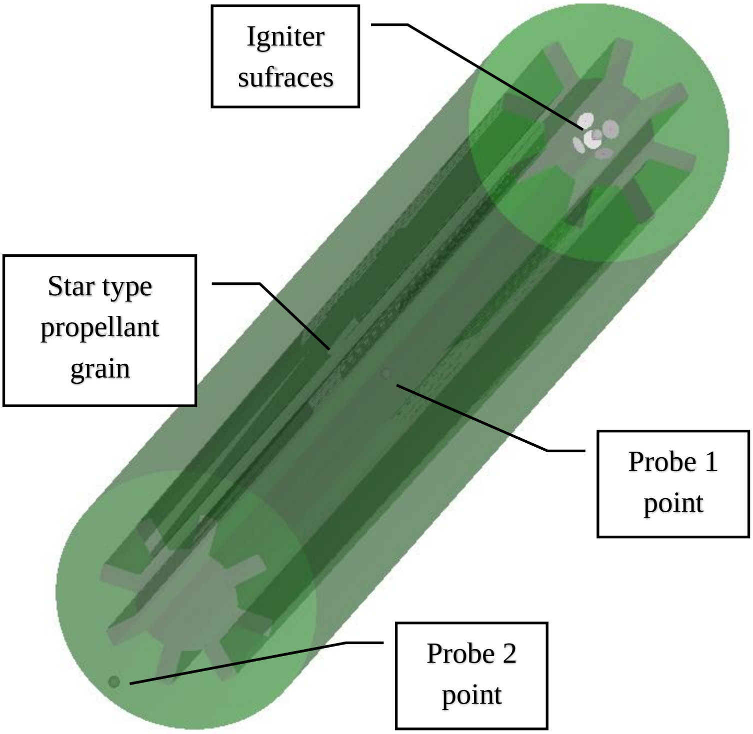

Fig. 2.3.12. Geometry representation of the propellant grain which was used in the study. Refer to Fig. 3.2.14 item 4

Fig. 2.3.13. Produced propellant grain. Refer to Fig. 3.2 item 4

After describing all the solid bodies which will be used in the simulation, the fluid itself has to be constrained. From the numerical code perspective, most of the setup was described in the previous sections. On top of that, it is worth noting that, when the propellant grain is constrained as a special type component in the numerical code, one additional setup has to be completed in order to allow the combustible object to work. In the previous section which was dedicated to the combustion process for the numeric solution, two specific constants were introduced. They are named ‘a’ and ‘b’ and are the combustion coefficient and the combustion rate exponent, respectively. These two constants constitute everything that is needed to describe the combustion process and grain evolution from the numerical code setup perspective.

After some trial and error tinkering and comparison with the small portions of the process from the static test data, we can finally conclude the final values of these parameters. All of the properties for the fluid and solid domains required for the simulation are described in Table 2.4.

Table 2.4. The main properties of the fluid and solid domains, as well as those of the introduced combustion gas as a mass source for the simulation

Fluid	Density ρ, kg/m^3	Individual gas const. Rt, J/kg/K	Specific heat C_v, J/kg/K	Thermal conductivity k, W/m/K
Combustion gas	1.446	347.943	2102	0.1
Solid	Density ρ, kg/m^3	Combustion temperature T_c, K	Combustion threshold temperature T_t, K	Empirical coefficients a, b
Propellant	1623	2322	1000	0.039, 0.27

Gravity was also introduced in the model. A graphic representation of the model in the Flow-3D graphical user interface is shown in **Fig. 2.3.14**. The gravity vector was parallel to the Cut plane #1 and was facing towards the bottom (from the **Fig. 2.3.14** perspective). This indicates that static firing testing was executed when having the motor in the same position as described below.

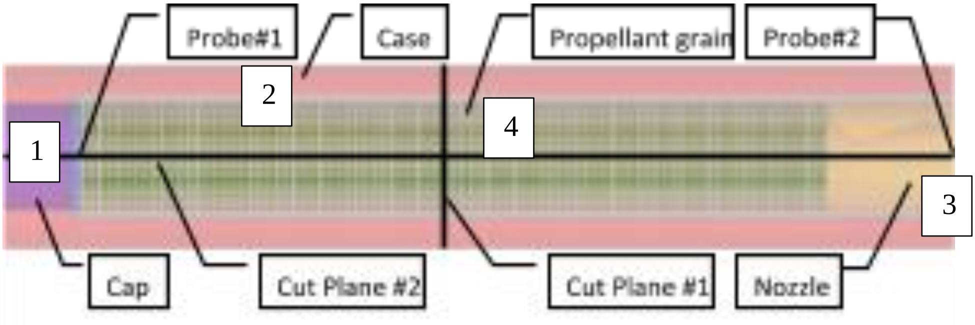

Fig. 2.3.14. Schematic model

In conclusion, it is noteworthy that different assumptions may be required if the results are replicated when using a different numerical code.

2.4 Summary

To conclude this chapter, we can summarize the following main points:

1. The model was described with regard to this mathematical term
2. The model itself was described and constructed in the specific numerical code
3. The geometry and mesh data were replicated the same as in a real rocket motor for the most crucial elements of the system.

3. METHODOLOGY AND RESULTS OF EXPERIMENTAL APPROACH OF SOLID PROPELLANT ROCKET MOTOR INTERNAL BALLISTIC CHARACTERISTICS

3.1. RM-12K rocket motor design

The RT-400 rocket uses a solid propellant RM-12K motor with the star-shaped grain that provides the motor with the neutral thrust profile, which means that, during the combustion, the average thrust produced by the motor is relatively stable throughout the Steady-state phase. The motor was designed and developed specifically for the RT-400 rocket. The table below contains the core motor characteristics.

Table 3.1. RM-12K solid-propellant rocket motor characteristics

Designed thrust, N	12000
Maximum thrust, N	13000
Average thrust, N	10000
Burn time, s	3.5
Propellant mass, kg	18
Motor mass, kg	33.5
Impulse, N·s	33000
Specific impulse, s	187 (230)

Motor development is divided into 3 phases. The first phase consists of creating the mixture for the propellant, whereas the second phase involves forming the actual grain out of the propellant, and, finally, during the third phase, the propellant grain is bonded with the rest of the motor. The motor itself is comprised of the external casing, the thermal-isolation material, the specialized sealing elements, the electronic components, the igniter and other, smaller components.

The materials used in the propellant are chemically stable and not toxic. The combustion of the propellant is based on the chemical reaction of two main components – the fuel and the oxidizer. In this case, the fuel is aluminum powder, and the oxidizer is ammonium nitrate. Both components are widely used in the industry for manufacturing and agriculture. For instance, aluminum powder is used in the paint industry, whereas ammonium nitrate is commonly used as a fertilizer in agriculture.

Furthermore, the powdery propellant mixture is combined with various polymers, and the resulting substance is then formed with specialized, purpose-built machinery (**Fig. 3.1**) which gets it pressed with 10 tons of force. The substantial pressure force is required to eliminate any and all imperfections in the powdery mixture as a failure to do that may cause the motor to explode during combustion due to the developed micro cavities. The risk of explosion arises due to an increase in the surface area as a direct result of the propellant grain imperfections which, in turn, can increase the chamber pressure to the point at which the containment shell may disintegrate under the forces acting from inside the motor. A couple of tests were conducted specifically to determine the relationship between the propellant grain integrity and the safety of the motor. The results showed that the compromised propellant integrity is directly correlated with the reduction in the motor's safety and an increase in the risk of explosion.

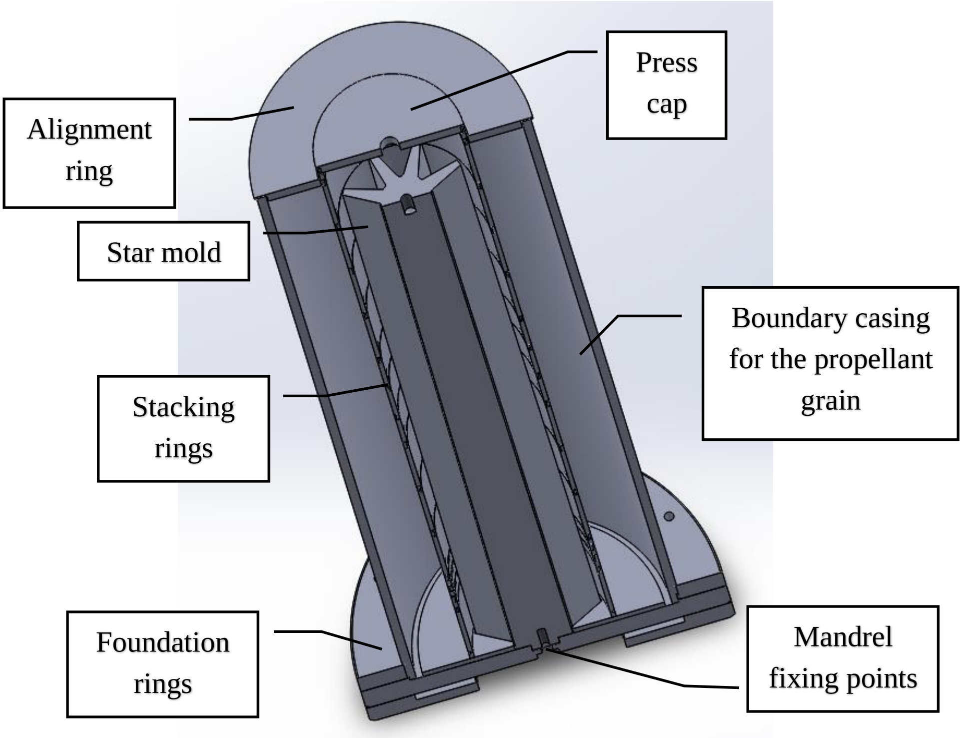

Fig. 3.1. Technological equipment for the production of the rocket motor propellant grain

The motor grain is formed by specialized machinery and powered by a hydraulic press which iteratively forms the propellant grain monolith. Additionally, the machinery does more than the aforementioned forming of the grain as it also sands the grain and controls the geometrical shape that is required per design parameters. The geometrical control, although important, would be impossible without the said machinery because the star-shaped grain geometry is not completely perpendicular to the plane that holds it; in fact, the shape has a specific gradient of 0.71°. The gradient is required to aid the ignition process when the falling igniter combustion products through the inside of the grain need to have as many contact points with the grain as possible.

The final product of the motor formation process is completely polymerized propellant grain which is then taken out from the mold to be dried, weighed, and measured. Finally, the walls of the propellant grain are inspected once again to make sure there are no mechanical imperfections.

The motor is assembled first by inserting the propellant grain into the motor case. Insulation materials, O-rings and gaskets are added below. We insert the nozzle and the screw cap [89]. The initiation charge is also installed. Everything is sealed and prepared for the installation in a rocket. The illustration below shows the motor components (**Figure 3.2**) where 1 – igniter, 2 – pressure cap, 3 – nozzle, 4 – propellant grain, 5 – O-rings, 6 – mounting rings, 7 – motor head.

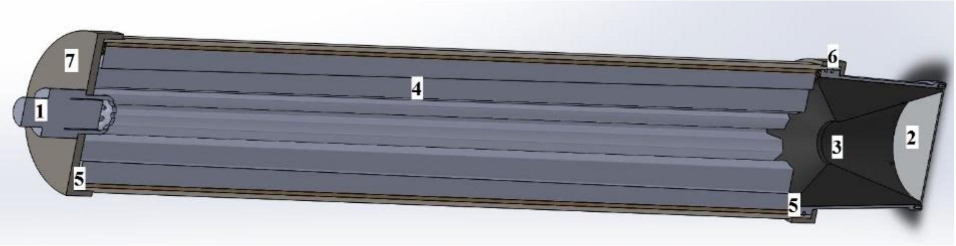

Fig. 3.2. 3D composition of the rocket motor

Another important milestone is with regard to motor testing. To produce a reliable and accurate system of the declared parameters, it is necessary to test the motor on the test stand.

In the aerospace industry as well as the automotive industry, the motor used and the knowledge about it allows to further design the desired system of parameters and to identify the possible engine deficiencies or inaccuracies at an early stage of the product development as well as to compare the theoretical design data with the experimental design.

3.2. The static test stand for the solid rocket motor

The most accurate and optimal testing method is the vertical test method when the motor is tested in the same position as the complete system. Unfortunately, the design of the stand is structurally complicated, and there is a problem in eliminating possible additional defects due to the structural deformation and, of course, the stand itself becomes less rigid and, as a rule, non-mobile (without the possibility of being transported to a safe storage location). Therefore, a horizontal type test stand was selected. This was done in order to achieve the best cost-effectiveness and precision properties. It should be noted that the simplest version of the test stand is the same vertical type in the opposite direction only, but this has been discarded due to the increased probability of clogging the nozzle throat due to solid particles build-up from the combustion products which may cause the motor to explode. The illustration below shows a test stand for rocket motors. Its design image is depicted as 1, the manufactured product is shown as 2, and the test-motor-mounted and fully equipped system is number 3 (**Fig. 3.3**).

Fig. 3.3. Structure of the rocket motor test stand

One of the key features of the aforementioned design was the ability to minimize the friction between the test stand and the rocket motor. This was critical due to the requirements for the precision of the thrust measurements because the rocket motor placement was horizontal. This was solved by introducing ball bearings at 4 points thus forming the cross formation. Having said that, another mandatory feature of the test stand was the ability to fine-tune the center alignment with the thrust sensor. This is highly critical as well because the direct measurement of the thrust can develop an error when slight misalignment is introduced. This was achieved by having 4 contact points between the rocket motor and the ball bearings. The aforementioned contact points had the ability to be fine-tuned by using a threaded rod which was individually adjustable. The final feature of the test stand was designed for the versatility of the stand. This was done to allow the ability to use the stand for various types of motors. The head section of the stand was able to extend and subtract in order to fit the required motor for testing. For the RM-12K motor test, the stand configuration was set to the smallest configuration. One of the advantages of such a configuration was the most stable and centered setup for testing. The testing scheme of the static testing procedure is presented in the figure below (**Fig. 3.4**).

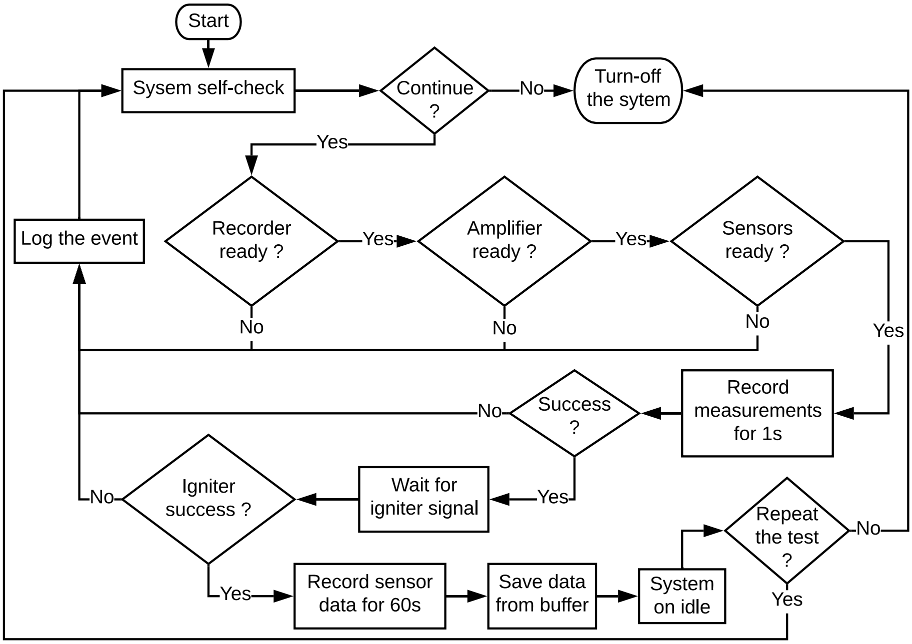

Fig. 3.4. Procedure of static testing

During the experiment, the data acquisition program starts recording as soon as a command for the initiation device has been sent. A triggered initiation device ejects the hot gas mass flow into the combustion chamber. The motor grain ignites and starts to generate thrust. The thrust is generated for about 3.5 seconds and starts to deplete after the wall of this burning propellant has almost aligned with the wall of the propellant grain thermal insulation. At this stage, the motor stops generating thrust rapidly. After burning the residual propellant in the combustion chamber for some time due to the pressure there, the gas contained therein escapes through the nozzle until, finally, the combustion chamber pressure equates to the atmospheric pressure. The illustration below shows the rocket motor that is attached to the test stand during experimental testing at the moment when the motor generates full thrust (between 0.5 and 3 seconds (**Fig. 3.5**)).

Fig. 3.5. General view of the steady-state of the motor during the experiment

The experiment and the data obtained after processing the raw data when using the MATLAB program resulted in a time-dependent thrust curve profile of the tested motor (**Fig. 3.6**) [90]. It was found that the maximum thrust that could be developed during the test was 13054 Newtons. The average thrust of the motor was found to be 4814 Newtons. This value was obtained by measuring the pressure in the combustion chamber from the ignition initiation until it equalized to the atmospheric pressure. The impulse generated by the motor was 32995 Newton Seconds. The specific impulse of the motor was 186.8 (230, 233) seconds. We must note that, from the different tests of the motor, different specific impulses were observed. The data presented in the figure below is from the test when ISP was 230 s. From the additional study, it was determined that the low specific impulse was caused by the quality of the propellant. The main reason for this lack of performance was the increased humidity levels during the casting process of the propellant grain. Thus it has to be noted that the humidity control during the casting process is crucial if the projected energetic properties of the propellant need to be achieved.

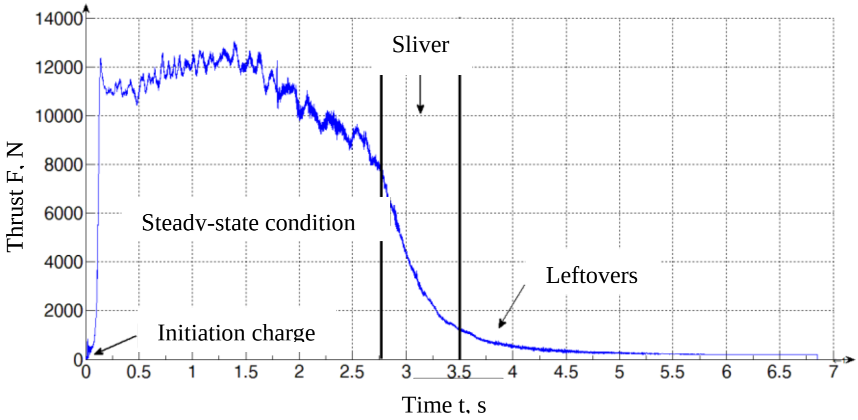

Fig. 3.6. Post-processed thrust data of the rocket motor

3.3. Test equipment of the RM-12K rocket motor

For a complete and ready-to-use motor, the thrust, pressure and some other characteristics, and, for reliability tests, a specific test stand is required. With the help of a test stand, the existing motor can be tested under static conditions, and one can check motor’s deformation both, when the motor is performing and when the propellant has been depleted. The case deformation can occur due to the temperature and pressure changes, causing the displacement of the materials thus deforming structural elements of the rocket. Also, a test stand can be used to determine the motor-generated thrust, the motor-generated pressure, and the temperature in the combustion chamber, to determine the burning rate of the propellant and to evaluate the various inaccuracies that were not anticipated during the motor design and production phases. The testing of rocket motors requires special work safety and careful preparation because the rapid and uncontrolled combustion process in the case of an accident would simply not allow the involved individuals any time to react to the changed situation due to their relatively slow reaction time [91]. Although it has been mentioned in the literature review that a solid propellant rocket motor is based on controlled combustion (its area), however, the propellant combustion itself is uncontrolled as the elements reacting in the chemical reaction of the combustion propellant decompose in such a way that the medium itself takes care not to shorten the oxygen combustion; thus it is virtually impossible to extinguish such a propellant. Although the test stand has been designed to measure various parameters, only the measured thrust and pressure will be evaluated in this work. For the thrust measurement, a special load cell was used based on the strain gauges with heat-resistant transition. Since the motion of the sensor in relation to the axis is in the order of tenths of a millimeter, in order to avoid possible measurement errors, it is necessary to ensure as far as possible the evaluation of the influence of foreign factors on the measurements as the motor heats up suddenly during its operation thus transferring heat to the measuring head (if it is metallic). Such an error can later lead to the development of major errors in the calculation of a possible rocket flight distance or other external ballistic characteristics [92]. To eliminate a potential problem, the test stand head was made from the massive metal plate with a high thermal mass. The illustration below depicts the measurement equipment used to determine the thrust of the rocket motor and the chamber pressure. **Fig. 3.7** Part 1 shows the measurement sensor and instrumental amplifier circuit with the measurement representation points. Part 2 shows the used high-power load module (capable of measuring, and a significantly larger thrust than the 12 kN thrust designed for this motor). Part 3 illustrates the pressure sensor used to assess the specificity of the combustion chamber. Part 4 shows the full-featured equipment. When knowing the theory of the nozzle which was outlined in the literature review, it can be understood that, due to the geometric dimensions of the nozzle and the set pressure in the combustion chamber, the nozzle can be redesigned to increase or decrease the motor power because the motor power is then generated. When there is high gas pressure in the combustion chamber, low velocity passes its pressure through the nozzle neck thereby increasing the velocity. In this way, when knowing the equation of the nozzle and having experimental data on the pressure of the combustion chamber, we can evaluate the errors of the designed system or the rates of wear of the thermal insulation (the nozzle spread).

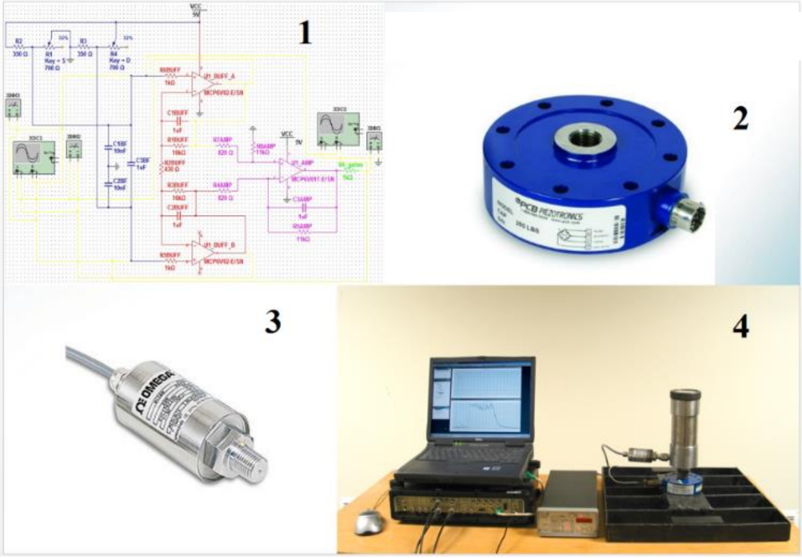

Fig. 3.7. Measuring equipment used in our research

Therefore, with the fully assembled electronic equipment, it is necessary to have a structure, to which all the sensors and the motor itself can be attached thus minimizing the existing friction and the influence of gravity. This is because the thrust vector is directly measured, but the laws of physics indicate that there is always the force of gravity whose influence can be minimized by various engineering solutions.

4. RESULTS OF THE SIMULATION AND EXPERIMENTAL APPROACH OF SOLID PROPELLANT ROCKET MOTOR INTERNAL BALLISTIC CHARACTERISTICS

4.1. Methodology for determining and presenting results

The methodology for capturing and presenting the simulation results was determined as follows. First, for the graphical representation, the simulation results were captured for six different time marks: 1 – the initial state at t = 0 s, 2 – 1/5 of the finished combustion process at time t = 1 s, 3 – 2/5 of the initial combustion process at time t = 2 s, 4 – 3/5 of the combustion process at time t = 3 s, 5 – 4/5 of the combustion process at time t = 4 s, and 6 – the finished combustion process at time t = 5 s. This was performed in order to clearly represent the changing evolution of the solid propellant grain throughout time. Secondly, the data used to plot the results was obtained from the probe points and mesh results. Moreover, the data for the burn distance and the open area of the combusting grain surface and volume was obtained from the results of the mesh dependent history. Meanwhile, the pressure and temperature values were extracted from the probes. Additional data was obtained representing the thrust and the total impulse of the motor. Finally, all of the data was captured from the very beginning of the simulation, only skipping the igniter execution time of 0.4 s. Most importantly, the pressure and temperature data was simultaneously collected at all datapoints during the simulation.

For presenting the data in the nozzle section, the probe line was created across the center axis of the model. The length of the probe line was 0.24 m, where 0.07 m was the probing across the combustion chamber, 0.034 m was the probing across the converging part of the nozzle, 0.006 m was probed across the throat section, and 0.17 m was probed across the diverging part of the section. The time step for nozzle readings was taken after the end of the initiation device had taken effect (which was 0.4 s) with the addition with some delay. The time marks of the readings for all the data with regard to the nozzle plots were taken at 0.5 s time marks.

The methodology for capturing the results from the experimental approach was done according to the DAQ (data acquisition) unit. The data acquisition time step was 0.004 s. The recording of the data was triggered after sending the fire command of the initiation charge. All the gathered pressure and thrust readings data from different sensors was parsed and plotted in the graphical form for future analysis and comparison.

4.2. Rocket motor internal ballistics simulation results

To develop better understanding of the combustion process and motor performance due to the specific grain, the post-processed data was categorized into 4 different parts. The first part was dedicated to pressure and density. The pressure readings were shown for the combustion chamber and the nozzle. On top of that, the pressure and density change was plotted through the axis of the nozzle to see the change in pressure and density caused by the choked flow. In the second part, the temperature results of the fluid were plotted for the combustion chamber and the nozzle. In addition, the average fluid temperature was plotted for the whole fluid domain. In the third part, the velocity plot was presented through the nozzle. Velocity measurements in the combustion chamber are not necessary to obtain because the area of interest for the velocity effect only evokes interest from the throat through the diverging section of the nozzle. In the fourth part of the discussion of the results, the open surface area (the combusting area), the volume, and the burning rate of the propellant grain are presented. This was done to evaluate the thrust profile neutrality behavior of the employed star-shaped propellant grain. The correlating pattern of the open surface versus the thrust profile was desirable to observe. On top of that, the propellant volume was plotted regarding the desired linear-like regression behavior, and the burn rate was plotted in order to observe the desirable semi-constant behavior. In the fifth part, the grain evolution was plotted due to the showcase change in the propellant grain with respect to the different time step. The development of the sliver was one of the desired features to observe. It was done because of deeper understanding of the possible optimization of the future grain design interactions. The final (sixth) part was dedicated to the thrust representation during the entire combustion process. This result was subsequently used for the comparison with the experimental results.

4.2.1. Pressure and density

After post-processing the simulation data, the results were obtained. The probe sample points for the pressure and temperature are provided in **Figs. 4.1, 4.2, 4.3,** and **4.4**.

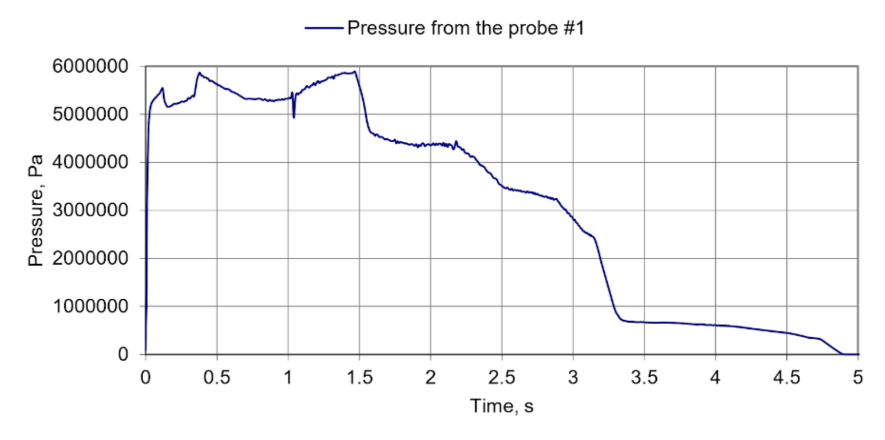

Fig. 4.1. Pressure versus time for Probe 1 point (head)

The pressure probing of the cap section was performed at the same location as for the experiment. The plotted results of Probe 1 exhibited the standard pressure curve behavior for the star-shaped propellant grain type. The pressure readings for different time marks were: 1 – the initial state at t = 0 s, 1.01 MPa (1.01 bar); 2 – 1/5 of the finished combustion process at time t = 1 s, 53.39 MPa (53.39 bar); 3 – 2/5 of the initial combustion process at time t = 2 s, 43.64 MPa (43.65 bar); 4 – 3/5 of the combustion process at time t = 3 s, 27.57 MPa (27.57 bar); 5 – 4/5 of the combustion process at time t = 4 s, 6.57 MPa (6.06 bar); and 6 – the finished combustion process at time t = 5 s, 446 Pa (0.0045 bar).

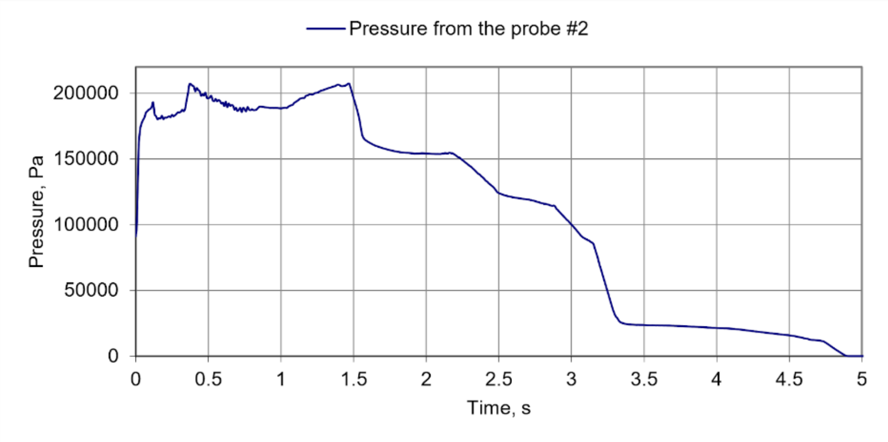

Fig. 4.2. Pressure versus time for Probe 2 point (nozzle)

For Probe 2 point, the pressure readings exhibited a similar pattern to that of the cap section, but with lower values, which was caused by the converging-diverging nozzle. In the experiment, the pressure readings at Probe 2 point were not possible because of the volatile nature of the combusting propellant, which limited the data measurement options during the static motor test. The pressure readings of Probe 2 point were: 1 – the initial state at t = 0 s, 91192 Pa (0.91 bar); 2 – 1/5 of the finished combustion process at time t = 1 s, 1.88 MPa (1.89 bar); 3 – 2/5 of the initial combustion process at time t = 2 s, 1.54 Pa (1.54 bar); 4 – 3/5 of the combustion process at time t = 3 s, 97795 Pa (0.98 bar); 5 – 4/5 of the combustion process at time t = 4 s, 21330 Pa (0.21 bar); and 6 – the finished combustion process at time t = 5 s, 14.31 Pa (0.00014 bar).

As mentioned in the section on methodology for determining and presenting the obtained results, the monitoring line through the center axis of the whole nozzle was probed, and data was plotted below to depict the pressure and density trends (**Fig. 4.3** and **Fig. 4.4**).

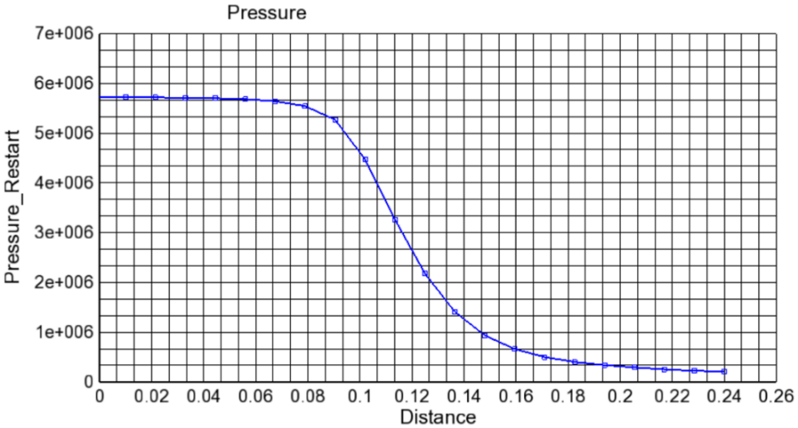

Fig. 4.3. Pressure versus distance for the nozzle

For the pressure plot, the x-axis is in respect for the distance, for which, meters are employed as the unit of measurement, and, the y-axis outlines the pressure which is measured in pascals. According to the plot depicted above, the pressure in the combustion chamber was 56.66 MPa (56.66 bar) on average when the sharp transition of the decrease of the pressure was observed at the throat where the value was 44.29 MPa (44 bar) and the diverged section of the nozzle where, at the end of the nozzle, the pressure value was 210618 Pa (2.1 bar). According to analytical calculations, the throat pressure was 57.3 MPa (57 bar), and the exit pressure equalled 1.01 MPa (1 bar). What regards these results, the error was 28.69% and 52.18%, respectively. In the table below, we can see the values according to the distance of the described plot.

Table 4.1. Pressure across nozzle section

Probe point No.	Distance, m	Pressure, bar	Comment
1	0	56.66	Combustion chamber
2	0.01	56.66	Combustion chamber
3	0.02	56.56	Combustion chamber
4	0.03	56.48	Combustion chamber
5	0.04	56.38	Combustion chamber
6	0.05	56.21	Combustion chamber
7	0.06	55.82	Combustion chamber
8	0.07	54.83	Combustion chamber
9	0.08	54.85	Converging section
10	0.09	52.16	Converging section
11	0.1	44.29	Throat
12	0.11	32.3	Throat
13	0.12	21.58	Diverging section
14	0.13	13.97	Diverging section
15	0.14	10.26	Diverging section
16	0.15	9.27	Diverging section
17	0.16	6.56	Diverging section
18	0.17	4.95	Diverging section
19	0.18	3.98	Diverging section
20	0.19	3.34	Diverging section

21	0.2	2.88	Diverging section
22	0.21	2.5	Diverging section
23	0.22	2.21	Diverging section
24	0.23	2.16	Diverging section
25	0.24	2.1	Diverging section

For the density plot, the same methodology of data capturing was used as outlined above. The x-axis was in respect of the distance in meters, and the y-axis was in respect of kg/m^3. The probed density at the combustion chamber was 6.28 kg/m^3 on average, when the sharp transition of the decrease of the pressure was observed at the throat where the value was 5.05 kg/m^3 and the diverged section of the nozzle where, at the end of the nozzle, the pressure value was 0.35 kg/m^3. The same pattern with regard to the pressure plot was observed when the fluid was traveling through the throat and the diverging section of the nozzle, the volume of the combustion products was expanding, which led to the rapid change in the density.

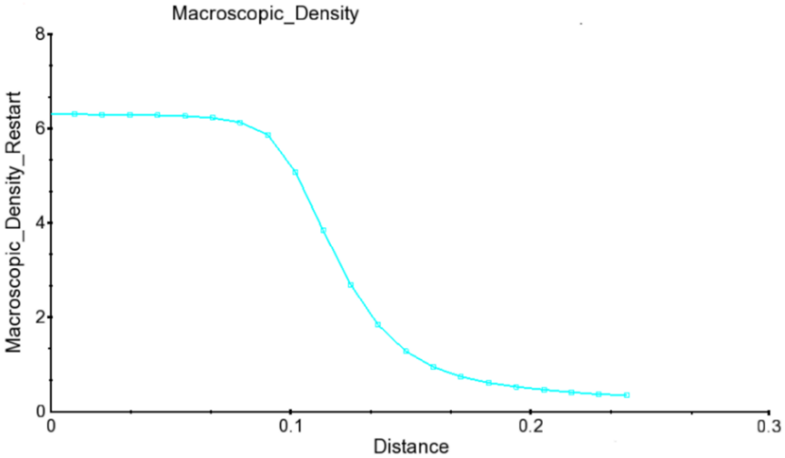

Fig. 4.4. Pressure changes across the nozzle

Table 4.2. Density across nozzle section

Probe point No.	Distance, m	Density, kg/m^3	Comment
1	0	6.28	Combustion chamber
2	0.01	6.27	Combustion chamber
3	0.02	6.27	Combustion chamber
4	0.03	6.26	Combustion chamber
5	0.04	6.25	Combustion chamber
6	0.05	6.23	Combustion chamber
7	0.06	6.22	Combustion chamber
8	0.07	6.19	Combustion chamber
9	0.08	6.1	Converging section
10	0.09	5.83	Converging section
11	0.1	5.05	Throat
12	0.11	3.82	Throat
13	0.12	2.68	Diverging section
14	0.13	1.82	Diverging section

15	0.14	1.57	Diverging section
16	0.15	1.27	Diverging section
17	0.16	0.94	Diverging section
18	0.17	0.73	Diverging section
19	0.18	0.6	Diverging section
20	0.19	0.52	Diverging section
21	0.2	0.46	Diverging section
22	0.21	0.4	Diverging section
23	0.22	0.38	Diverging section
24	0.23	0.36	Diverging section
25	0.24	0.35	Diverging section

4.2.2. Temperature

The temperature readings were only obtained from the simulations. The temperature probes used in the static test were unable to capture reliable data because the temperature was too high and the exposure time was too long for the hot combustion gas. At Probe 1 location, the temperature readings were: 1 – the initial state at t = 0 s, 300 K; 2 – 1/5 of the finished combustion process at time t = 1 s, 2359 K; 3 –2/5 of the initial combustion process at time t = 2 s, 2360 K; 4 – 3/5 of the combustion process at time t = 3 s, 2350 K; 5 – 4/5 of the combustion process at time t = 4 s, 2338 K, and 6 – the finished combustion process at time t = 5 s, 1895 K.

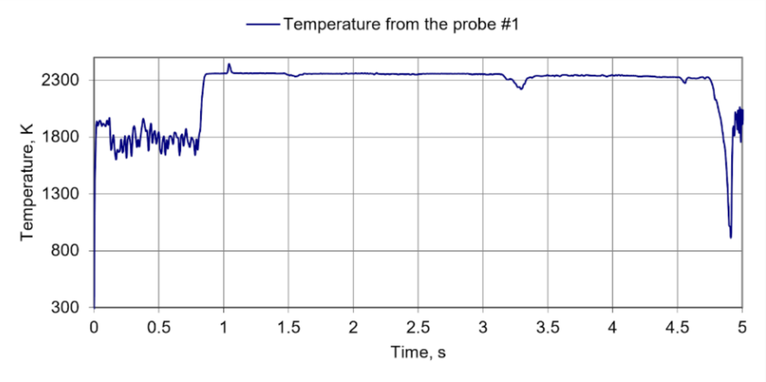

Fig. 4.5. Temperature versus time for Probe 1 point (head)

The temperature sampling data of Probe 2 was different from that of Probe 1. This was caused by the combustion gas escaping from the combustion chamber through the nozzle throat. As a result, the heat energy was released because of the converging-diverging nozzle. The temperature data readings of Probe 2 were: 1 – the initial state at t = 0 s, 300 K; 2 – 1/5 of the combustion process at time t = 1 s, 1382 K; 3 – 2/5 of the initial combustion process at time t = 2 s, 1382 K; 4 – 3/5 of the combustion process at time t = 3 s, 1380 K; 5 – 4/5 of the combustion process at time t = 4 s, 1381 K; and 6 – the finished combustion process at time t = 5 s, 1285 K. According to analytical calculations, the exit temperature was 1207 K. For these results, the error was 12.66%.

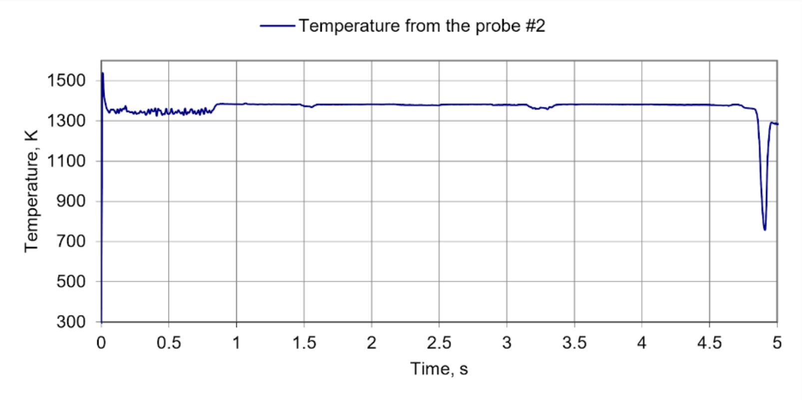

Fig. 4.6. Temperature versus time for Probe 2 point (nozzle)

Additional data was extracted for the mesh dependent results in order to better represent and enhance the understanding of the problem. The average fluid temperatures in the computational domain and the temperature across the nozzle are plotted in **Figs. 4.7** and **4.8**, respectively.

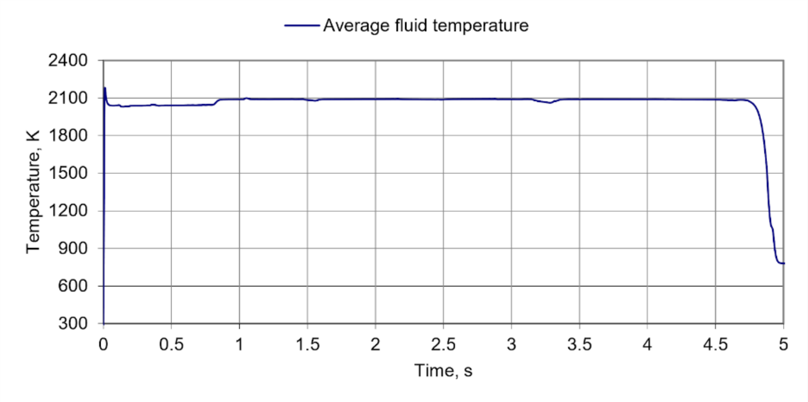

Fig. 4.7. Average fluid temperature

The sample data of the average fluid temperature was obtained from the entire computational domain. This was performed in order to determine the required thermal protection solutions. High temperatures inside the combustion chamber can lead to a failure of the mechanical components due to high thermal loads. From the sampled data, the average fluid temperature inside the combustion chamber was 2080 K, which demonstrates that adequate thermal protection is necessary to obtain nominal motor performance parameters and avoid catastrophic failures due to component rupturing.

The temperature plot for the nozzle is depicted in **Fig. 4.8** below. In the aforementioned plot, the x-axis is with respect to the distance whose units of measurement are meters, and, for the y-axis, the temperature is measured in Kelvins. According to the plot depicted above, the temperature in the combustion chamber was

2592 K on average, when the sharp transition of the decrease of the temperature was observed at the throat where the value was 2514 K and in the diverged section of the nozzle, at the end of the nozzle, the temperature value was 1724 K. In the table below, we can see the values according to the distance of the described plot. The tabular data of the aforementioned plot is presented in Table 4.3.

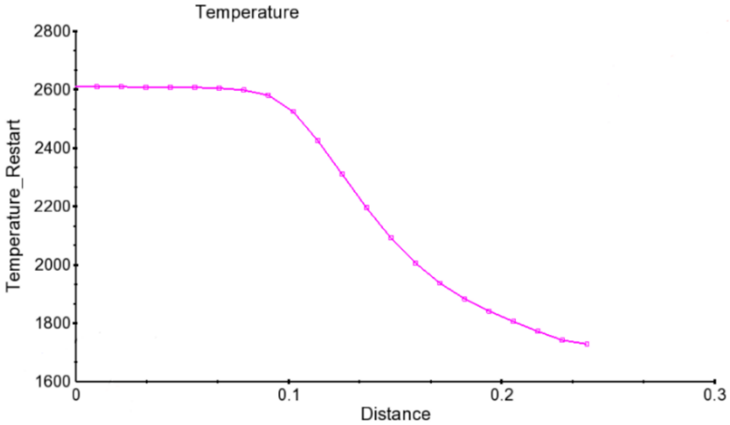

Fig. 4.8. Temperature changes across the nozzle

Table 4.3. Temperature across nozzle section

Probe point No.	Distance, m	Temperature, K	Comment
1	0	2592	Combustion chamber
2	0.01	2592	Combustion chamber
3	0.02	2592	Combustion chamber
4	0.03	2591	Combustion chamber
5	0.04	2591	Combustion chamber
6	0.05	2590	Combustion chamber
7	0.06	2589	Combustion chamber
8	0.07	2588	Combustion chamber
9	0.08	2582	Converging section
10	0.09	2567	Converging section
11	0.1	2514	Throat
12	0.11	2317	Throat
13	0.12	2302	Diverging section
14	0.13	2187	Diverging section
15	0.14	2122	Diverging section
16	0.15	2083	Diverging section
17	0.16	1998	Diverging section
18	0.17	1929	Diverging section
19	0.18	1876	Diverging section
20	0.19	1834	Diverging section
21	0.2	1798	Diverging section
22	0.21	1765	Diverging section
23	0.22	1755	Diverging section
24	0.23	1736	Diverging section
25	0.24	1724	Diverging section

4.2.3. Velocity

The area of interest for velocity in the solid rocket motor is at the nozzle section because, in the combustion chamber, thermal energy is stored and converted into kinetic energy when combustion products gets into the nozzle section. During this energy conversion process, the velocity of the combustion products gains momentum, and acceleration is achieved when entering the throat and then through the diverging section of the nozzle. The velocity plot for the nozzle is depicted in **Fig. 4.9** below. In the aforementioned plot, the x-axis is with respect to the distance which was measured in meters and to the y-axis depicting the velocity in meters per second. According to the plot depicted above, the velocity in the converging section of the nozzle was 257 m/s on average when sharp transition of the increase of the velocity was observed at the throat where the value was between 714 m/s to 1014 m/s, and the diverged section of the nozzle where, at the end of the nozzle, the velocity value was 2200 m/s. According to analytical calculations, the throat velocity was 937 m/s, and the exit velocity was 2204 m/s. What regards these results, the error was 8.44% and 0.18% respectively. In the table below, one can see the values according to the distance of the described plot. The tabular data of the aforementioned plot is presented in Table 4.4.

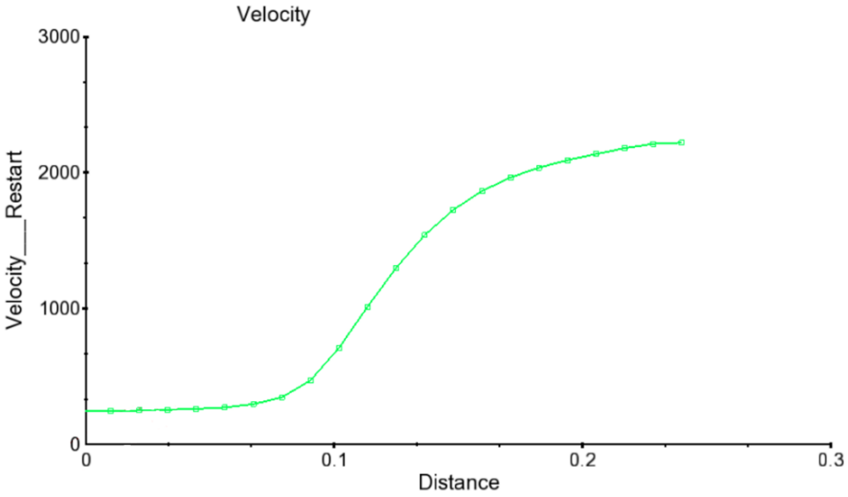

Fig. 4.9. Velocity changes across the nozzle

Table 4.4. Velocity across the nozzle section

Probe point No.	Distance, m	Velocity, m/s	Comment
1	0	257	Combustion chamber
2	0.01	259	Combustion chamber
3	0.02	263	Combustion chamber
4	0.03	267	Combustion chamber
5	0.04	273	Combustion chamber
6	0.05	284	Combustion chamber
7	0.06	293	Combustion chamber

8	0.07	306	Combustion chamber
9	0.08	355	Converging section
10	0.09	478	Converging section
11	0.1	714	Throat
12	0.11	1014	Throat
13	0.12	1300	Diverging section
14	0.13	1430	Diverging section
15	0.14	1538	Diverging section
16	0.15	1723	Diverging section
17	0.16	1860	Diverging section
18	0.17	1960	Diverging section
19	0.18	2033	Diverging section
20	0.19	2088	Diverging section
21	0.2	2133	Diverging section
22	0.21	2176	Diverging section
23	0.22	2188	Diverging section
24	0.23	2198	Diverging section
25	0.24	2200	Diverging section

4.2.4. Burn rate, surface, and volume

The performance of the motor is closely coupled with its combustion surface area. This is a key parameter when designing rocket motors for specific performance requirements. The open surface of the solid propellant rocket motor from the beginning of combustion until the propellant has depleted completely is shown in the plot below (**Fig. 4.10**). The values of the open surface of the propellant grain were: 1 – the initial state at t = 0 s, 0.4 m^2; 2 – 1/5 of the combustion process at time t = 1 s, 0.42 m^2; 3 – 2/5 of the initial combustion process at time t = 2 s, 0.348 m^2; 4 – 3/5 of the combustion process at time t = 3 s, 0.224 m^2; 5 – 4/5 of the combustion process at time t = 4 s, 0.054 m^2; and 6 – the finished combustion process at time t = 5 s, 0.005 m^2.

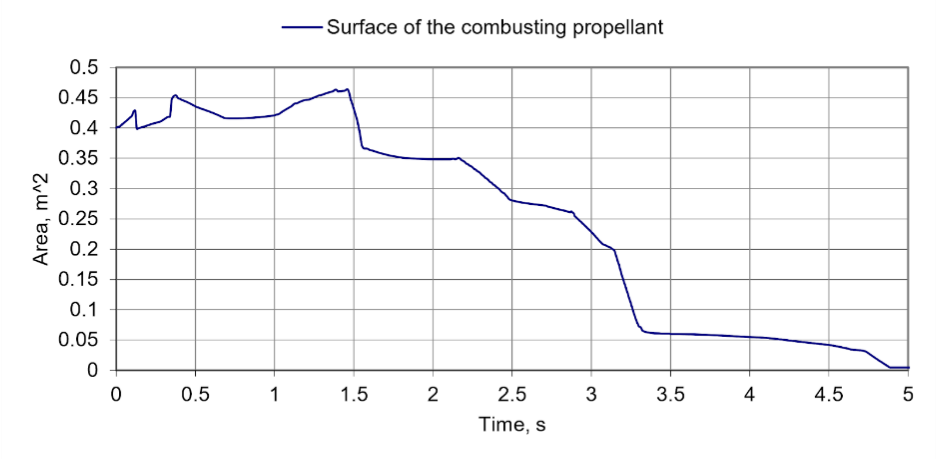

Fig. 4.10. Combustion surface area

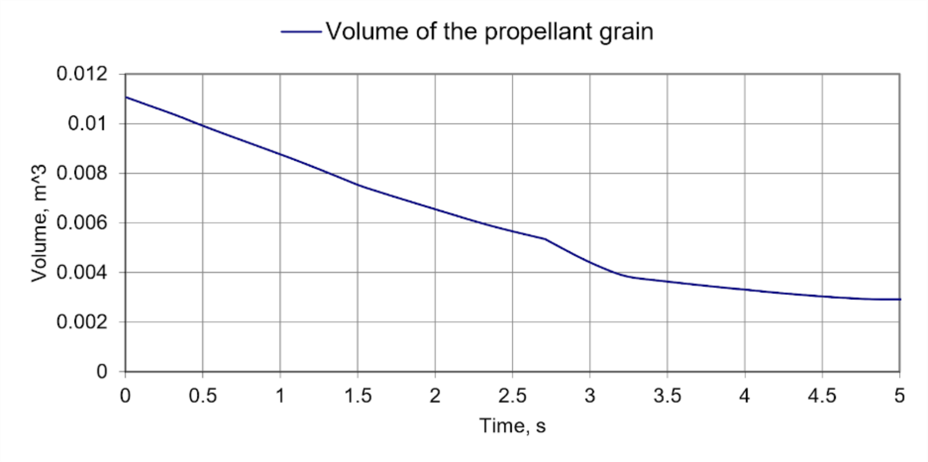

Fig. 4.11. Combustion surface volume

In order to obtain greater understanding of the research results, the change in the combustion propellant grain volume was plotted in **Fig. 4.11**. The combustion stability was determined which is based on stable regression of the propellant volume during combustion. According to these results, combustion was stable throughout the entire combustion process until the sliver phase had been reached, and then it continued steadily until the propellant had been depleted completely. The volume of the propellant steadily depleted from the initialization (0.011 m^3) to the sliver phase (0.0043 m^3).

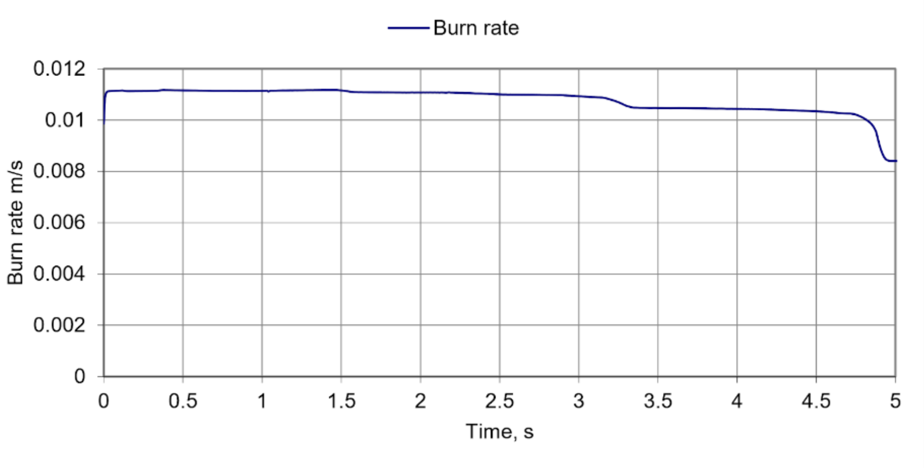

Fig. 4.12. Propellant grain burning rate

The burning rate of the propellant was extracted according to Eq. 2.19 as follows: 1 – the initial state at t = 0 s, 0.00986 m/s; 2 – 1/5 of the combustion process at time t = 1 s, 0.0111 m/s; 3 – 2/5 of the initial combustion process at time t = 2 s, 0.011 m/s; 4 – 3/5 of the combustion process at time t = 3 s, 0.011 m/s; 5 – 4/5 of the combustion process at time t = 4 s, 0.01 m/s; and 6 – the finished combustion process at time t = 5 s, 0.0084 m/s.

4.2.5. Grain evolution

Fig. 4.13 and **Fig. 4.14** depict the evolution of the propellant grain during combustion at different times. The key advantages of being able to monitor and measure the changes in the propellant surface area and its shape over time are that the inner workings of the motor can be understood, and the parameters can be fine-tuned for enhanced performance. Moreover, the data provided by the cross-section would not otherwise be available if only static testing could be performed. Furthermore, as shown in **Fig. 4.13**, the propellant grain transforms as it combusts. The vector field is included to represent the fluid motion. The data is also color-coded to represent the different components within the RM-12K motor.

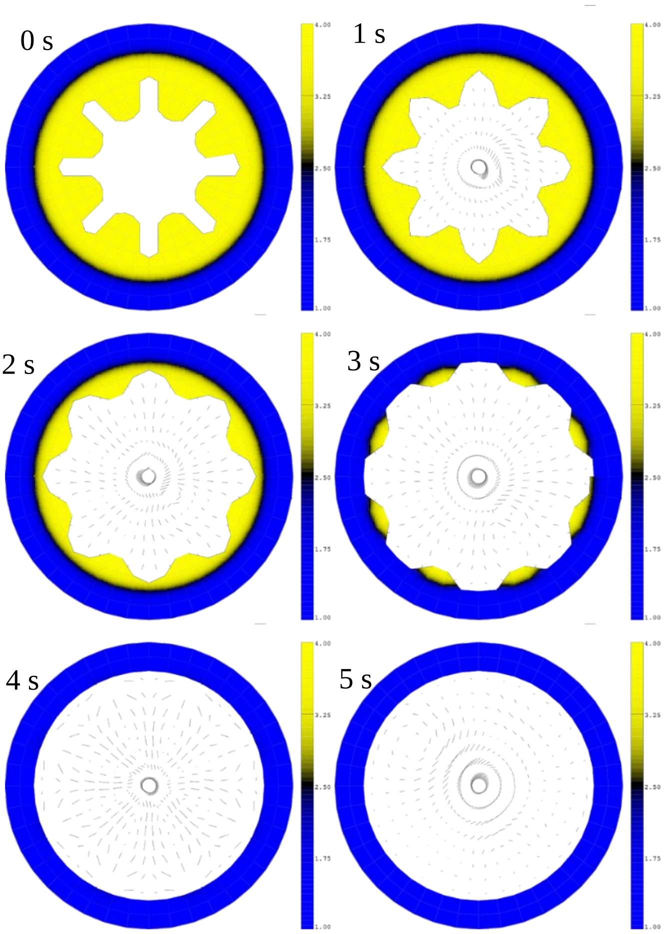

Fig. 4.13. Propellant combustion evolution at t = 0, 1, 2, 3, 4, and 5 seconds for the x-y axis

Fig. 4.14 depicts a different cross-section of the same combustion transformation process as for **Fig. 4.13**.

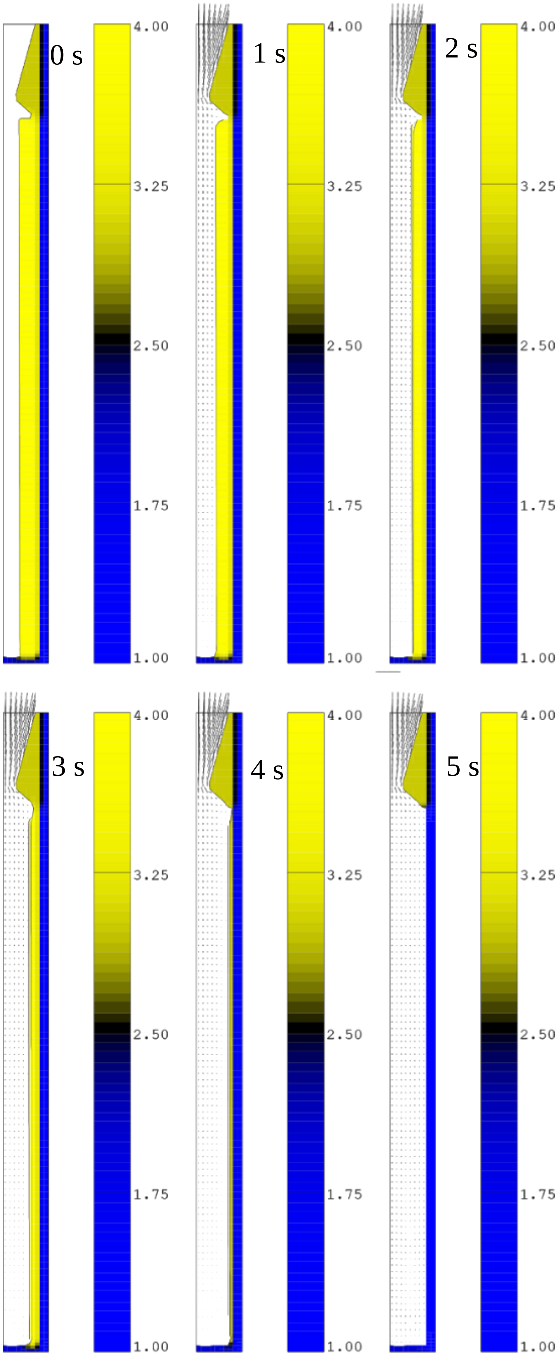

Fig. 4.14. Propellant combustion evolution at t = 0, 1, 2, 3, 4, and 5 seconds

4.2.6. Thrust

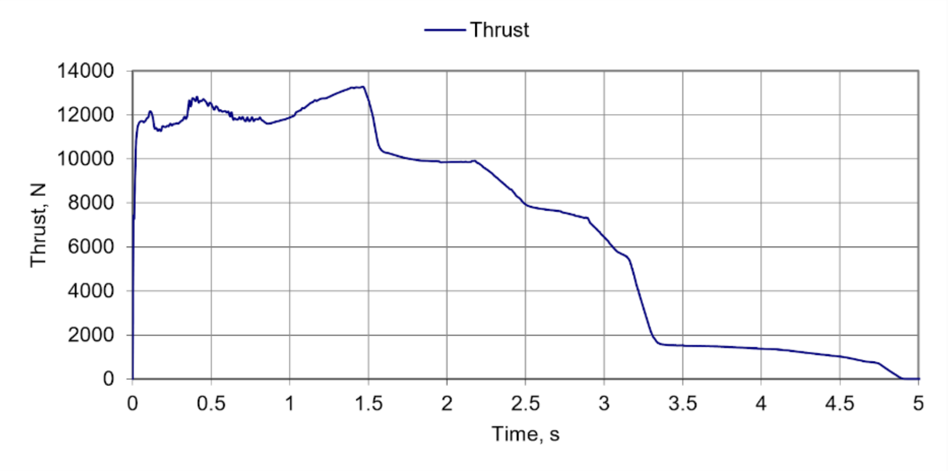

Fig. 4.15. Rocket motor thrust

The thrust produced by the motor is given in Eq. (4.1) and is explained below.

$$F = \dot{m}v_e\left(p_e - p_0\right)A_e\ . \tag{4.1}$$

Here, F is the thrust, ṁ is the mass flow rate from the nozzle exit, v_e is the exit velocity from the nozzle (custom monitoring plane), p_e is the pressure at the end of the nozzle (Probe 2), p_0 is the atmospheric pressure (initial pressure), and A_e is the exit area (custom monitoring plane). The thrust values were as follows: 1 – the initial state at t = 0 s, 0 N; 2 – 1/5 of the combustion process at time t = 1 s, 11879 N; 3 – 2/5 of the initial combustion process at time t = 2 s, 9859 N; 4 – 3/5 of the combustion process at time t = 3 s, 6359 N; 5 – 4/5 of the combustion process at time t = 4 s, 1364 N; and 6 – the finished combustion process at time t = 5 s, 1.02 N.

4.3. Model results verification with experimental results

The aforementioned results were verified by comparison of the pressure and thrust. This was done because there are only two possible data sets from the experimental approach to be compared with the simulation. In the tables below, we can see experimental data made for comparison with the simulation data. We must note that, for the experimental data, the first and the last time step are bigger when compared with the model results. This is because of sensor readings. For the comparison in the error calculation section, we must anticipate that the atmospheric pressure is neglected, and this is why both values are more similar.

Table 4.5. Experimental results of the rocket motor

	Time, s					
	0	1	2	3	4	5
	Values					
Pressure from probe No. 1, bar	1.01	55.39	43.65	27.78	2.93	1.2
Pressure from probe No. 2, bar	n/a	n/a	n/a	n/a	n/a	n/a

Temperature from probe No. 1, K	n/a	n/a	n/a	n/a	n/a	n/a
Temperature from probe No. 2, K	n/a	n/a	n/a	n/a	n/a	n/a
Average fluid temperature, K	n/a					
Propellant area, m²	n/a	n/a	n/a	n/a	n/a	n/a
The burn rate of the propellant, mm/s	n/a	n/a	n/a	n/a	n/a	n/a
Thrust, N	0	11909	11126	5817	604	271

Table 4.6. Model results of the rocket motor

	Time, s					
	0	1	2	3	4	5
	Values					
Pressure from probe No. 1, bar	0.1	55.39	43.65	27.57	6.06	0.0045
Pressure from probe No. 2, bar	0.91	1.89	1.54	0.98	0.21	0.00014
Temperature from probe No. 1, K	300	2359	2360	2350	2338	1895
Temperature from probe No. 2, K	300	1382	1382	1380	1381	1285
Average fluid temperature, K	2080					
Propellant area, m²	0.4	0.42	0.348	0.224	0.054	0.005
The burn rate of the propellant, mm/s	9.86	11.1	11	11	10	8.4
Thrust, N	0	11879	9859	6359	1364	1.02

4.4. Comparison of the results

The model used for the simulation was valid and physically correct according to the observed parameters during the static testing and correlated within a reasonable degree of confidence to the parameters obtained during the simulation. The experimental results of the changes in pressure and thrust over time were evaluated. Moreover, the aforementioned data was compared with the results obtained from the simulation. This was performed to test the model compatibility and, from the observed results, it can be concluded that the model is capable of representing all of the key characteristics of the combustion process of the solid propellant rocket motor.

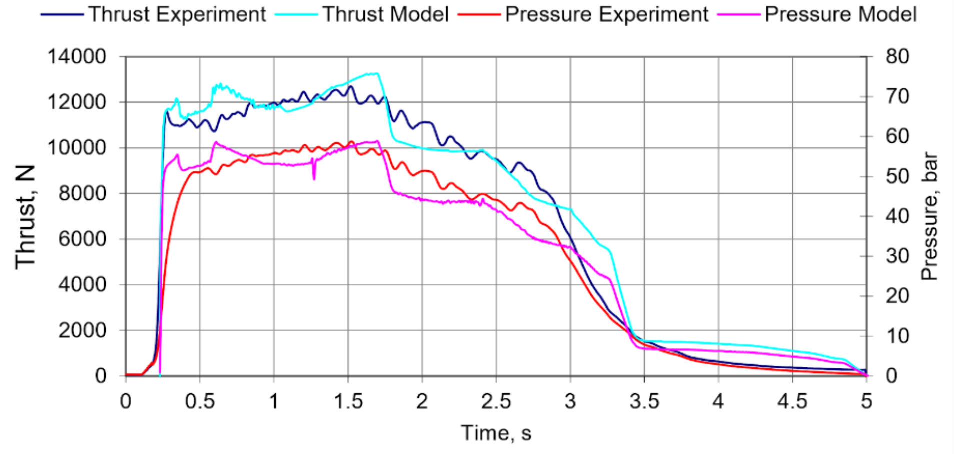

Fig. 4.16. Thrust and pressure comparison of the rocket motor by the experimental approach correlated with the data of the simulation

It must be noted that, at the end of the measurement time, some deviation was observed. This was caused because of the way the experiment was set up. The thrust sensor, after the sliver phase, read the mass of the rocket motor with additional friction effects. Such a behavior is negligible for the validation of the model because TWR after the sliver phase is not sufficient enough to produce the lift effect in real-world applications when the rocket motor is not attached to the test stand and flying at the steady-state when airborne. This insight only reinforces the statement that the simulation is able to provide the results closer to the real-world situation while fully overcoming the test stand limitations.

As in **Fig. 4.16** above, the graphical representation of the comparison is converted into the table form. From Table 4.7, we can see the errors of thrust and pressure at different time steps. The area of interest is the phase between the 1st and the 3rd seconds, otherwise known as the steady-state, which is the combustion period when the motor is generating thrust. It is important to note that the errors depicted in the table are taken as maximum values available at the respective time steps so that to showcase the worst-case scenario. However, it is likely that the error deviation is actually smaller in reality as pressure probes and thrust sensors are experiencing vibrations and other physical impediments during the experiment, which causes the readings to fluctuate more significantly. Moreover, as already noted in the previous paragraph, the error values during the sliver phase (the 4th second) are extremely high due to the specific way the experiment was set up and do not represent the actual deviation, although it could be mathematically calculated by subtracting the mass of the motor from the readings of sensors.

Table 4.7. Error in percentages of static testing and model results

	Time, s					
	0	1	2	3	4	5
	Error					
Pressure error, %	0.01	0.87	8.29	0.75	106.82	15.45
Thrust error, %	0	0.25	11.38	9.31	125.82	0.37
Description	Start-up	Steady-state	Steady-state	Steady-state	Sliver	Leftovers
	Not generating sufficient thrust	Generating thrust			Not generating sufficient thrust	

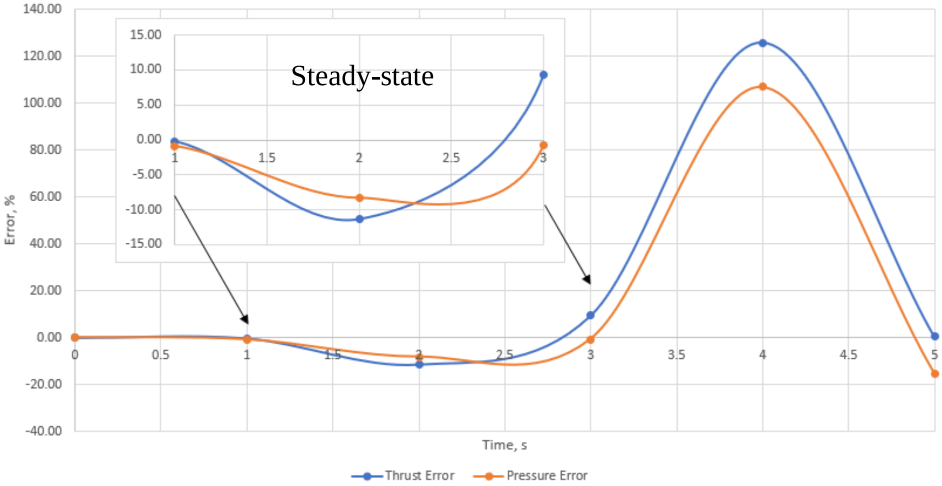

Fig. 4.17. Graphical representation of the error

All in all, after the comparison of the static test results against the simulated data, we can conclude that the simulation is accurate enough to be used as a virtual twin for improving and optimizing the motor. The experimental errors are acceptable and can be explained, whereas some of the analytical errors, such as the exit and throat pressure, diverge from the experimental and simulation results beyond the comfortable acceptance levels. This indicates that the analytical means of calculating rocket performance could be useful as high-level guidelines for motor design, but this strategy is too rough and inaccurate when it comes to calculating the exact motor performance and to identifying the potential issues with the design. What is more, the simulation produced data points that are otherwise virtually impossible to measure during an experiment because of extreme physical conditions in which sensors are rendered obsolete. The aforementioned additional data points uncovered areas of improvement that, if addressed, may potentially increase the motor's efficiency and performance.

4.5. Summary of the chapter

1. The methodology of the results was as follows: first, the physical simulation time was set to 5 seconds. This was done in order to ensure full coverage of the entire combustion process and at some time after the process for a more precise comparison. Secondly, the representation of the results was divided into the marks covering one second each. This was done in order to present data in the table form due to the clear explanation for the start-up, steady-state and sliver processes.
2. The results were extracted and presented in the form of figures. The main interest was dedicated to the pressure, temperature, and velocity in the combustion chamber and at the end of the nozzle. Some figures were extracted for the representation of the average values.

3. Another set of results was extracted only to cover the nozzle area. This was done in order to evaluate the physical processes which occur by the converging/diverging nozzle when the flow is compressible. The pressure, temperature, velocity and density changes were covered through the axis of the entire nozzle and presented as figures and tables.
4. Another set of data was extracted and derived from the data outlined in Figures 4.12 and 4.15. The burn rate and the thrust were obtained. The results showed minimal deviation from the analytical calculations and the experimental values.
5. Both experimental and simulation results were compared with regard to model validation. The results showed virtually no error in the initial state, which highlights that the initial conditions for the model were close enough to the values of experimental testing. What regards the steady-state phase, the minimal error versus the maximal error was in the range of 0.25% to 11%. This concludes that the model is valid enough to produce trustworthy results without the need for additional comparison by doing static testing.
6. In conclusion, it is possible to reproduce the static test data by using numerical methods based on computer modeling and simulations. This approach provides additional insights that are useful for more profound understanding of the processes involved in combustion-related problems and the internal ballistics of solid propellant rocket motors. This enables the optimization of the design parameters with minimal costs and maximum benefits.

CONCLUSIONS

Analysis of analytical, static and numerical approaches showed that, in conclusion, numerical methods-based simulations are a viable option for the design and development of solid propellant rocket motors, and, in some cases, it is even more advantageous than static testing. This conclusion can be expanded into:

1. A 3D model of a solid propellant rocket motor based on mass conservation, fluid motion, heat transfer laws and equations of the fluid interface in the computational domain at the cell level between the fluid and solid parts evaluating the energy properties of the propellant and its combustion in the chamber and peculiarities of the nozzle in the discharge area was developed.
2. Simulations of the initial and boundary conditions were established in order to evaluate the pressure and temperature in the combustion chamber, the physical properties of the fluid and solid-state regions, and CAD geometry and a computational grid were constructed to allow sufficiently accurate modeling and determination of solid propellant combustion and motor internal ballistics characteristics.
3. The simulation results obtained from the internal ballistics of solid rocket motors covered the time, pressure, thrust, temperature in the combustion chamber and the nozzle as a function of time and volume of the fuel grain and surface area and the evolution of the fuel grain during combustion.

4. Comparative analysis of the simulation results and the static/experimental ballistic pressure and the thrust characteristics of the RM-12K solid-propellant rocket motor showed that the model error compared to the experimentally obtained results does not exceed 15%, whereas the average error in the main combustion phase ranged from 0.25% to 11%. This indicates that the simulation based on numerical modeling is valid and represents reasonably accurately the physical internal ballistics processes occurring in the course of motor operation.
5. A methodology for the development of solid-propellant rocket motors has been developed which evaluates the energy properties of the propellant and its combustion chamber characteristics and reduces or alters the need for experimental testing thus enabling the design of solid-propellant rocket motors at a reduced cost and time.

REFERENCES

1. Siemienowicz, K. (1650). *Ars magna artilleriae*. Amsterodami: Janssonius.
2. Semerjyan, V. (2013, January 25). *Tsiolkovsky's Rocket equation*. Retrieved May 23, 2017, from https://smallsats.org/2013/01/24/tsiolkovskys-rocket-equation/.
3. Garner, R. (2015, February 11). *Dr. Robert H. Goddard, American Rocketry Pioneer*. Retrieved May 23, 2017, from https://www.nasa.gov/centers/goddard/about/history/dr_goddard.html.
4. Wade, M. (1997). *Von Braun, Wernher*. Retrieved May 23, 2017, from http://www.astronautix.com/v/vonbraun.html.
5. Washington, D.C., NASA Headquarters, NASA Historical Reference Collection, NASA History Division. (1955). NSC 5520 "*Draft Statement of Policy on U.S. Scientific Satellite Program*," (p. 1). Washington, WA: NASA. Retrieved May 23, 2017, from https://history.nasa.gov/sputnik/17.html.
6. Schmidt, W. G. (27 January 1970). *U.S. Patent No. US3492176* A. Washington, DC: U.S. Patent and Trademark Office.
7. Wilson, J. (n.d.). *NASA - Solid Rocket Boosters*. Retrieved May 23, 2017, from https://web.archive.org/web/20130406193019/http://www.nasa.gov/returntoflight/system/system_SRB.html.
8. Mehta, U.B., "*Guide to Credible Computer Simulations of Fluid Flows*," AIAA Journal of Propulsion and Power, Vol. 12, No. 5, September-October 1996, pp. 940-948. (Also, AIAA Paper 95-2225).
9. B. N. Kondrikov, V. E. Annikov, V. Yu. Egorshev, L. DeLuca, and C. Bronzi. "*Combustion of Ammonium Nitrate-Based Compositions, Metal-Containing and Water-Impregnated Compounds*", Journal of Propulsion and Power, Vol. 15, No. 6 (1999), pp. 763-771. http://dx.doi.org/10.2514/2.5526.
10. Favini B., Di Giacinto M., Serraglia F., "*Modeling of Flowfield Features During Ignition of Solid Rocket Motors*", AIAA Paper N° 2002-3753, 38th Joint Propulsion Conference, Indianapolis, Indiana, July 2002.
11. Beckstead, M.W. *Combust Explosive Shock Waves* (2006) 42: 623. doi:10.1007/s10573-006-0096-5.
12. Harrland, A., & Johnston, I. A. (2012). *Review of Solid Propellant Ignition Models Relative to the Interior Ballistic Modelling of Gun Systems* (1st ed., Vol. 1, UNCLASSIFIED, pp. 1-41, Tech. No. DSTO-TR-2735). Edinburgh, South Australia: Australian Government, Department of Defence, Defence Science and Technology Organization. Retrieved May 23, 2017, from https://www.dst.defence.gov.au/sites/default/files/publications/documents/DSTO-TR-2735.pdf.
13. Pandit, A. V., Kumar, A., Srinivasa Rao, G., Kedarnath, C., Srihari, R., & Ranade, V. V. (2012). *Decomposition of Solid Propellants in a Combustion Chamber*. Advanced Chemical Engineering Research (ACER), 1(1), 8-17. Retrieved May 23, 2017, from https://ia801002.us.archive.org/11/items/ACER003_201311/ACER003.pdf.

14. Kritzinger, W., Karner, M., Traar, G., Henjes, J., & Sihn, W. (2018). *Digital Twin in manufacturing: A categorical literature review and classification*. IFAC-PapersOnLine, 51(11), 1016-1022.
15. Orlebar, C. (1997). *The concorde story* (p. 39). Osprey publishing.
16. Byers, A. (2002). *The crash of the concorde*. The Rosen Publishing Group, Inc.
17. Baals, D. D., Robins, A. W., & Harris Jr, R. V. (1970). *Aerodynamic design integration of supersonic aircraft*. Journal of Aircraft, 7(5), 385-395.
18. Nangia, R., Palmer, M., & Iwanski, K. (2004). *Towards design of long-range supersonic military aircraft*. In 22nd Applied Aerodynamics Conference and Exhibit (p. 5071).
19. Fry, R. S. (2004). *A century of ramjet propulsion technology evolution*. Journal of propulsion and power, 20(1), 27-58.
20. Hank, J., Murphy, J., & Mutzman, R. (2008, April*). The X-51A scramjet engine flight demonstration program*. In 15th AIAA International Space Planes and Hypersonic Systems and Technologies Conference (p. 2540).
21. Giorgi, B. R. (2013). *Experimental and computational analysis of a miniature ramjet at Mach 4.0*. NAVAL POSTGRADUATE SCHOOL MONTEREY CA.
22. Tsuru, K., & Naitoh, K. (2016). *Computational experiments for improving the performance of Fugine based on supermulti-jets colliding working for a wide range of speeds from startup to hypersonic condition*. In 52nd AIAA/SAE/ASEE Joint Propulsion Conference (p. 4709).
23. Dunbar, B. (2015, August 13). *NASA Dryden Fact Sheets - X-15 Hypersonic Research Program*. Retrieved May 23, 2017, from https://www.nasa.gov/centers/armstrong/news/FactSheets/FS-052-DFRC.html.
24. The US Military Planned on Using This Crazy Modified C-130 to Rescue Hostages in Iran. (2016, June 28). Retrieved May 23, 2017, from https://tacairnet.com/2016/06/28/the-us-military-planned-on-using-this-crazy-modified-c-130-to-rescue-hostages-in-iran/.
25. Neri, A., Bianchi, S., Pascal, P., & Cutroni, M. (2003, July). *An Overview of Vega Solid Rocket Motors Development and Qualification Program*. In 39th AIAA/ASME/SAE/ASEE Joint Propulsion Conference and Exhibit (p. 5284).
26. Rocket Lab Raises $75 Million in Funding for Production of Electron Rocket. (n.d.). Retrieved May 23, 2017, from https://www.rocketlabusa.com/latest/series-d-financing/.
27. Lee, T. W., & Lee, T. W. (2014). *Basics of Rocket Propulsion. In Aerospace Propulsion* (Vol. 1, pp. 176-178). John Wiley & Sons.
28. Shanks, R., & Hudson, M. K. (2000). *A labscale hybrid rocket motor for instrumentation studies*. Journal of Pyrotechnics, 11(2).
29. Undefined, U. U. (2017). *1.2. ROCKET PROPULSION*. In G. P. Sutton & O. Biblarz (Authors), Rocket propulsion elements (pp. 5-9). Hoboken (N.Y.): Wiley.
30. Fedaravičius, A., Račkauskas, S., Survila, A., & Šamelis, A. (2016 09 22). *External ballistics modelling of the "RT-400" rocket aerial target*. XIth INTERNATIONAL ARMAMENT CONFERENCE ON SCIENTIFIC ASPECTS OF ARMAMENT AND SAFETY TECHNOLOGY, 11(1), 227-235.

31. Sutton, G. P., & Biblarz, O. (2017). *Solid propellant rocket fundamentals. 11.2. Basic performance relations*. In Rocket propulsion elements (7th ed., pp. 440-442). Hoboken, NJ: John Wiley & Sons Inc.
32. Davenas, A. (Ed.). (2012). *Solid rocket propulsion technology*. Newnes.
33. NATIONAL ASSOCIATION OF ROCKETRY. (n.d.). *Standard Motor Codes*. Retrieved May 29, 2017, from http://www.nar.org/standards-and-testing-committee/standard-motor-codes/.
34. Alemasov, V. E., Dregalin, A. F., & Tishin, A. F. (1970). *Theory of rocket engines* (No. FTD-MT-24-116-70). AIR FORCE SYSTEMS COMMAND WRIGHT-PATTERSON AFB OH FOREIGN TECHNOLOGY DIVISION.
35. Undefined, U. U. (2017). 8. *THRUST CHAMBERS*. In G. P. Sutton & O. Biblarz (Authors), Rocket propulsion elements (pp. 287-296). Hoboken (N.Y.): Wiley.
36. Bianchi, S., & IPT, V. I. P. T. (2008). *VEGA, the European small launcher: Development status, future perspectives, and applications*. Acta Astronautica, 63(1-4), 416-427.
37. Wright, D. (2015). Research note to hypersonic boost-glide weapons by James M. Acton: *analysis of the boost phase of the HTV-2 hypersonic glider tests*. Science & Global Security, 23(3), 220-229.
38. Kongsberg Gruppen ASA (KONGSBERG). (2015*). NASAMS Air Defence System* [Brochure]. Author.
39. Parsch, A. (2004, September 29). *Raytheon (General Dynamics) AGM / BGM / RGM / UGM-109 Tomahawk*. Retrieved May 28, 2017, from http://www.designation-systems.net/dusrm/m-109.html.
40. Montoya, J. (2003). *Advantages of Hybrid Systems*. Retrieved May 28, 2017, from http://www.angelfire.com/falcon/jmontoya/hybrid.html.
41. Wade, M. (1997). Encyclopedia Astronautica *Scout G-1*. Retrieved May 28, 2017, from http://www.astronautix.com/s/scoutg-1.html.
42. Kyle, E. (2016, July 6). Space Launch Report: *Pegasus Data Sheet*. Retrieved May 28, 2017, from http://www.spacelaunchreport.com/pegasus.html.
43. Kyle, E. (2017, April 12). Space Launch Report: *Chang Zheng Data Sheet*. Retrieved May 28, 2017, from http://www.spacelaunchreport.com/cz.html.
44. Wallace, J. S. (2018). 10. *Propellants*. In Chemical analysis of firearms, ammunition, and gunshot residue (pp. 57-62). Boca Raton, FL: CRC Press.
45. Wallace, J. S. (2018). 10. *Propellants*. In Chemical analysis of firearms, ammunition, and gunshot residue (pp. 62-67). Boca Raton, FL: CRC Press.
46. Oommen, C., & Jain, S. R. (1999). *Ammonium nitrate: a promising rocket propellant oxidizer*. Journal of hazardous materials, 67(3), 253-281.
47. Lempert, D. B., Nechiporenko, G. N., & Manelis, G. B. (2006). *Energetic characteristics of solid composite propellants and ways for energy increasing*. Central European Journal of Energetic Materials, 3(4), 73-87.
48. Chaturvedi, S., & Dave, P. N. (2013). *A review on the use of nanometals as catalysts for the thermal decomposition of ammonium perchlorate*. Journal of Saudi Chemical Society, 17(2), 135-149.

49. Manelis, G. B., & Lempert, D. B. (2009). *Ammonium nitrate as an oxidizer in solid composite propellants*. Progress in Propulsion Physics, I, 81-96. doi:10.1051/eucass/200901081.
50. Silant'yev, A. I. (1967). *Hybrid propellants*. In Solid Rocket Propellants (pp. 25-28). Ohio: FOREIGN TECHNOLOGY DIVISION. Retrieved June 4, 2017, from http://www.dtic.mil/dtic/tr/fulltext/u2/656567.pdf.
51. The Editors of Encyclopædia Britannica. (2016, December 26). *Air*. Retrieved June 04, 2017, from https://www.britannica.com/science/air.
52. Nakka, R. (2016, June 16). *Experiments with Ammonium Nitrate / Aluminum based Propellant Formulations*. Retrieved June 04, 2017, from https://www.nakka-rocketry.net/anexp.html.
53. Sutton, G. P. (2001). *RESULTS OF THERMOCHEMICAL CALCULATIONS*. In Rocket propulsion elements (9th ed., pp. 189-190). New York: Wiley.
54. Crouch, W. W. (1962*). U.S. Patent No. 3,023,570*. Washington, DC: U.S. Patent and Trademark Office.
55. Sutton, G. P., & Biblarz, O. (2017). *Solid propellant rocket fundamentals. 3.4. Nozzle configurations.* In Rocket propulsion elements (9th ed., pp. 73-81). Hoboken, NJ: John Wiley & Sons Inc.
56. Sutton, G. P., & Biblarz, O. (2017). 11.3. *PROPELLANT GRAIN AND GRAIN CONFIGURATION*. In Rocket propulsion elements (pp. 444-453). Hoboken (N.Y.): Wiley.
57. Sutton, G. P., & Biblarz, O. (2017). *Nozzle theory and thermodynamic relations. 11.3. Propellant grain and grain configuration*. In Rocket propulsion elements (7th ed., pp. 446-447). Hoboken, NJ: John Wiley & Sons Inc.
58. T. Harmon, "*X-33 Linear Aerospike on the Fast Track in System Engineering*" AIAA Paper 99-2181, Joint Propulsion Conference, June 1999.
59. Martelli, E., Nasuti, F., & Onofri, M. (2007). *Numerical parametric analysis of dual-bell nozzle flows*. AIAA journal, 45(3), 640-650.
60. Sutton, G. P., & Biblarz, O. (2017). 3.4. *NOZZLE CONFIGURATIONS*. In Rocket propulsion elements (pp. 75-85). Hoboken (N.Y.): Wiley.
61. Tsien, H. S. (1952). The transfer functions of rocket nozzles. Journal of the American Rocket Society, 22(3), 139-143.
62. Willcox, M. A., Brewster, M. Q., Tang, K. C., Stewart, D. S., & Kuznetsov, I. (2007). *Solid rocket motor internal ballistics simulation using three-dimensional grain burnback*. Journal of Propulsion and Power, 23(3), 575-584.
63. Davenas, A. (1993). 1.2.*5 The ignition system*. In Solid rocket propulsion technology (p. 9). Oxford: Pergamon.
64. Vivek, S., Sharan, S., Arvind, R., Praveen, D. V., Vigneshwar, J., Ajith, S., & Kumar, V. S. (2015). *Studies on Pre-Ignition Chamber Dynamics of Solid Rockets with Different Port Geometries*. World Academy of Science, Engineering and Technology, International Journal of Mathematical, Computational, Physical, Electrical and Computer Engineering, 9(8), 482-488.

65. A. Fedaravicius, A. Survila, S. Rackauskas, S. Kilikevicius, E. Slizys, L. Patasiene, *Air target for a rocket with an infrared targeting system* (March 2017).
66. Kuperman, A. J. (1999). *The Stinger missile and US intervention in Afghanistan*. Political Science Quarterly, 114(2), 219-263.
67. Motyl, K., Makowski, M., Zygmunt, B., Puzewicz, Z., & Noga, J. (2017). *A Concept for Striking Range Improvement of the GROM/PIORUN Man-Portable Air-Defence System*. Problemy Mechatroniki: uzbrojenie, lotnictwo, inżynieria bezpieczeństwa, 8.
68. Granlund, Rego, Erik Berglund, and Henrik Eriksson. "*Designing web-based simulation for learning*." Future Generation Computer Systems 17.2 (2000): 171-185.
69. Tian, H., Li, Y., Li, C., & Sun, X. (2017). *Regression rate characteristics of hybrid rocket motor with helical grain*. Aerospace Science and Technology, 68, 90-103. https://doi.org/10.1016/j.ast.2017.05.006.
70. Pralits J.; Natali D.; Guerrero J.; Bottaro A. 2018. *Wolf dynamics - multiphysics simulations, optimization, and data analytics*. [accessed 9 Feb. 2019]. Available from Internet: http://www.wolfdynamics.com/our-services/hpc-cloud-computing.html.
71. Guthrie, J. J. (2015). *CFD simulations on a Raspberry Pi cluster*. Frankfurt am Main. https://doi.org/10.13140/RG.2.1.1079.2486
72. Lichtl, A., & Jones, S. (2015). *GPUs to Mars: Full scale simulation of SpaceX's Mars rocket engine*. GTC2015. [accessed 3 Mar. 2019]. Available from Internet: http://on-demand.gputechconf.com/gtc/2015/presentation/S5398-Stephen-Jones-Adam-Lichtl.pdf.
73. Cengel, Y. A., & Cimbala, J. M. (2004). *Fluid Mechanics Fundamentals and Applications*.
74. Norton, T., & Sun, D. W. (2006). *Computational fluid dynamics (CFD)–an effective and efficient design and analysis tool for the food industry*: a review. Trends in Food Science & Technology, 17(11), 600-620.
75. Chorin, A. J., Marsden, J. E., & Marsden, J. E. (1990). *A mathematical introduction to fluid mechanics (Vol. 3*). New York: Springer.
76. Sreenivasan, K. R. (1995). *On the universality of the Kolmogorov constant*. Physics of Fluids, 7(11), 2778-2784.
77. Catalano, P., & Amato, M. (2003). *An evaluation of RANS turbulence modelling for aerodynamic applications*. Aerospace science and Technology, 7(7), 493-509.
78. Li, Y. H., & Kong, S. C. (2008). *Diesel combustion modelling using LES turbulence model with detailed chemistry*. Combustion theory and modelling, 12(2), 205-219.
79. Beckstead, M. W., Derr, R. L., & Price, C. F. (1970). *A model of composite solid-propellant combustion based on multiple flames*. AiAA Journal, 8(12), 2200-2207. https://doi.org/10.2514/3.6087.
80. Cummings, R. M., Mason, W. H., Morton, S. A., & McDaniel, D. R. (2015*). Applied computational aerodynamics:* A modern engineering approach (Vol. 53). Cambridge University Press.
81. Hirt, C. W., & Nichols, B. D. (1981). *Volume of fluid (VOF) method for the dynamics of free boundaries*. Journal of computational physics, 39(1), 201-225. https://doi.org/10.1016/0021-9991(81)90145-5.

82. Cummings, R. M., Mason, W. H., Morton, S. A., & McDaniel, D. R. (2015*). Applied computational aerodynamics:* A modern engineering approach (Vol. 53). Cambridge University Press.
83. Hirt, C. W., & Nichols, B. D. (1981). Volume of fluid (VOF) method for the dynamics of free boundaries. Journal of computational physics, 39(1), 201-225. https://doi.org/10.1016/0021-9991(81)90145-5.
84. Canu, P., & Vecchi, S. (2002). *CFD simulation of reactive flows: Catalytic combustion in a monolith*. AIChE Journal, 48(12), 2921-2935.
85. *Solid propellant combustion modeling* Flow-3d blog [Web log post]. 2017. Retrieved September 10, 2018, from https://www.flow3d.com/solid-propellant-combustion-modeling/
86. Hirt, C. W. (1989). *Flow in a Solid-Propellant Rocket Chamber*, Flow Science Technical Note #17.
87. Hartfield, R.; Jenkins, R.; Burkhalter, J.; Foster, W. 2003. *A review of analytical methods for solid rocket motor grain analysis*, 39th AIAA /ASME/SAE/ASEE Joint Propulsion Conference and Exhibit 39: 4506.
88. Lekstutis, *A. GUIPEP-Graphical User Interface to PEP*.
89. Canepa, M. (2005). *The Rocketry Toolbox*. In: Canepa, Mark B Modern High-Power Rocketry 2. 2nd ed. Victoria, BC, CANADA: National Library of canada Cataloguing in Publication. p335-340.
90. Taylor, T.S. (2009). *Thrust*. In: Travis, S. Taylor Introduction to Rocket Science and Engineering. Boca Raton, Filadelphia, FL, USA: CRC Press Taylor & Francis Group. p89-92.
91. Taylor, T.S. (2009). *Measuring Thrust*. In: Travis, S. TaylorIntroduction to Rocket Science and Engineering. Boca Raton, Filadelphia, FL, USA: CRC Press Taylor & Francis Group. p219-229.
92. Sutton, G.P. Biblarz, O. (2010). *Instrumentation and data management*. In: John Willey Rocket Propulsion Elements. 8th ed. Hoboken, New Jersey, USA: John Willey & Sons, Inc. p742.

PUBLICATIONS LIST ON THE SUBJECT OF THE DISSERTATION

Publications with IF:

1. Fedaravičius, A., Kilikevičius, S., Survila, A., & Račkauskas, S. (2019). *Short range rocket-target: research, development and implementation*. Aircraft engineering and aerospace technology, 00, 1-6. doi:10.1108/AEAT-07-2018-0177.

2. Fedaravičius, A., Račkauskas, S., Sližys, E., & Survila, A. (2014). *Investigation of solid rocket motor strength characteristics by employing composite materials*. Mechanika, 20(3), 247-253. doi: 10.5755/j01.mech.20.3.7158

3. Račkauskas, S., Fedaravičius, A., & Survila, A. (2019). *Numerical Study on Internal Ballistics Characteristics of a Solid Propellant Rocket Motor*. Mechanika, 25(3), 187-196. doi: 10.5755/j01.mech.25.3.23742.

Presentations at international conferences:

1. Fedaravicius, A., Kommanaboina, N., Manimaran, H., Papanaboina, M., Rackauskas, S., Survila, A., & Vikas, S. (2018). Research and design of middle range rocket target. In: Transport means 2018: proceedings of the 22nd international scientific conference, October 03-05, 2018, Trakai, Lithuania (pt. 3, pp. 1398-1403). Kaunas: Kaunas University of Technology

2. Fedaravičius, A., Kilikevičius, S., Survila, A., & Račkauskas, S. (2018). Research and development of a rocket with predefined parameters. In Transport means 2018: proceedings of the 22nd international scientific conference, October 03-05, 2018, Trakai, Lithuania (pt. 3, pp. 1432-1434). Kaunas: Kaunas University of Technology

3. Fedaravičius, A., Račkauskas, S., Survila, A., & Šamelis, A. (2016). External ballistics modelling of the "RT-400" rocket aerial target. In XI Międzynarodowa konferencja uzbrojeniowa nt. naukowe aspekty techniki uzbrojenia i bezpieczenstwa = 11th International armament conference on scientific aspects of armament & safety technology, Ryn, 19-22.09.2016 (pp. 227-235).

4. Fedaravičius, A., Račkauskas, S., Survila, A., Ragulskis, K., & Patašienė, L. (2014). Piezoelectric actuators and their application in precise-positioning systems and space structures. In Vibroengineering procedia: International conference Vibroengineering 2014, Katowice, Poland, 13-15 October 2014 (vol. 3, pp. 238-242). Kaunas: JVE International

Patent:

Fedaravičius, A. (inventor), Survila, A. (inventor), Račkauskas, S. (inventor), Kilikevičius, S. (inventor), Sližys, E. (inventor) and Patašienė, L. (inventor) (2017, March 10). Air target for a rocket with infrared targeting system. Patent No. LT 6371 B. *Patent Bureau of the Republic of Lithuania*.

SCIENTIFIC ACTIVITY

Publications in peer-reviewed scientific publications:

1. Fedaravičius, A., Račkauskas, S., Survila, A., & Šamelis, A. (2018). External ballistics simplified model of the "RT–400" rocket aerial target. Problemy mechatroniki: uzbrojenie, lotnictwo, inżynieria bezpieczeństwa = Problems of mechatronics: armament, aviation, safety engineering, 9(1), 9-22. doi:10.5604/01.3001.0011.7175.

2. Fedaravičius, A., Račkauskas, S., Survila, A., & Patašienė, L. (2015). Design of the testing system for solid propellant rocket motor thrust measurements using mathematical modelling techniques. Journal of measurements in engineering, 3(4), 123-131.

Other scientific research activities:

1. State project No. VPI-3.1-ŠMM-10-V-05 Development, research, implementation and commercialization of rocket technology for training. 2013-2015. Amount of project funding 2,467 Mill. LTL.

2. Contract No. 8754. Development, research and implementation of laser rifle simulator; 2015. UAB „Konsolė"; funding: 88,000 LTL.

3. Contract No. SV9-135. Development, research and implementation of laser rifle simulator; 2015. Lithuanian Riflemen's union; funding: 43,443.00 EUR.

4. Contract No. SV9-164. Launch services of the rocket – ballistic air target (NATO exercise "Amber Arrow – 2015"); 2015. LM Air defence battalion; funding 15,000 EUR.

5. Contract No. SV9- 0551. Development, research and implementation of a new type of laser rifle simulator; 2016. Lithuanian Riflemen's union; funding 55,000 EUR.

6. Contract No. SV9-1209. Launch services of the rocket – ballistic air target; (NATO exercise "Amber Arrow – 2017"); 2017. LM Air defence battalion; funding: 15,000 EUR.

7. Contract No. SV9-1607. Launch services of the rocket – ballistic air target; (international air defence exercise "Baltic Zenith 2018"); 2018. LM Air defence battalion; funding: 40,000 EUR.

8. Contract No. S-MIP-17-94/SV3-0464. Experimental rocket: Development and research; 2017-2020. Research council of Lithuania; funding 100,000 EUR.

9. Contract No. SV9-2229. Launch services of the rocket – ballistic air target; (international air defence exercise “Baltic Zenith 2019”); 2019. LM Air defence battalion; funding 15,000 EUR.

7 NATO NSNs created and installed in Lithuanian and foreign defence structures and included in NATO Logistics Catalogue:

- LT-5M Laser Rifle Simulator; 6920-47-000-7909;
- Laser Machine Gun Simulator LT-1 FN MAG; 6920-0000-7910;
- Laser Grenade Launcher LT-1 CARL GUSTAF; 6920-47-000-7911;
- LT-5M GLOCK-17 Laser Gun; 6920-47-000-9046;
- Automatic Laser Rifle LT-5M-M4A1; 6920-47-000-9047;
- Laser Gun LT-5M - P226; 6920-47-000-9048.
- Aerial rocket target complex RT-400; 6920-47-000-8331.

Awards:

1. 2016 Gold medal. Product of the year. MACHINERY AND EQUIPMENT INDUSTRY GROUP: Rifle Training Center Using Laser Training Weapons – LT-5M-M4A1, LT-5M-SIG SAUER P226, LT-5M-GLOCK 17 – Kaunas University of Technology Public enterprise VšĮ *Institute of defence technologies*.

2. 2014 Gold medal. Product of the year. MACHINERY AND EQUIPMENT INDUSTRY GROUP: The RT-400 Training Rocket Complex for STINGER air defence applications. – KTU Institute of Defence Technologies.

3. 2013 Gold medal. Product of the year. MACHINERY AND EQUIPMENT INDUSTRY GROUP: Laser equipment educational complex of small arms training – KTU Institute of Defence Technologies.

Fellowship:

Scientific Fellow. September – November, 2016. Military University of Technology. Warsaw, Poland.

SL344. 2020-04-07, 12,75 leidyb. apsk. l. Tiražas 12 egz.
Išleido Kauno technologijos universitetas, K. Donelaičio g. 73, 44249 Kaunas
Spausdino leidyklos „Technologija“ spaustuvė, Studentų g. 54, 51424 Kaunas